

GMI Calibration Algorithm and Analysis Theoretical Basis Document

Version G

Issued: April 19, 2012

Thomas Meissner

Frank Wentz

David Draper

Prepared by:

Remote Sensing Systems
444 10th Street, Suite 200, Santa Rosa, CA 95401

Prepared for:

Ball Aerospace & Technologies Corp.
P.O. Box 1062, Boulder, CO 80306

Table of Contents

1	INTRODUCTION AND OVERVIEW	9
1.1	PURPOSE OF THE GMI CALIBRATION ALGORITHM	9
1.2	PURPOSE AND CONTENTS OF ATBD	9
1.3	APPLICABLE AND SUPPLEMENTAL DOCUMENTS.....	10
2	GMI INSTRUMENT AND CALIBRATION SYSTEM.....	11
2.1	INSTRUMENT.....	11
2.1.1	<i>Receiver Subsystem</i>	12
2.1.2	<i>Antenna Subsystem</i>	12
2.2	IN-FLIGHT CALIBRATION SYSTEM.....	13
2.2.1	<i>Hot Load View</i>	13
2.2.2	<i>Cold Sky View</i>	14
2.2.3	<i>Noise Diodes</i>	15
2.3	REFERENCE VALUES.....	16
3	KEY REQUIREMENTS	17
3.1	FUNCTIONAL REQUIREMENTS.....	17
3.2	PERFORMANCE REQUIREMENTS.....	18
3.3	DERIVED REQUIREMENTS	19
3.4	INPUT REQUIREMENTS FOR THE CALIBRATION ALGORITHM.....	19
3.5	INPUT REQUIREMENTS FOR THE PRE-LAUNCH VERIFICATION ANALYSIS	19
4	ALGORITHM STRUCTURE AND SUBMODULES	20
4.1	BASIC FLOW	20
4.2	COLD CALIBRATION	21
4.3	HOT CALIBRATION	22
4.4	DETERMINATION OF CALIBRATION PARAMETERS.....	24
4.5	TRANSFORMATION FROM RADIOMETER EARTH MEASUREMENTS INTO ANTENNA TEMPERATURES	24
4.6	ANTENNA PATTERN CORRECTION: TRANSFORMATION FROM ANTENNA TEMPERATURES INTO TOA BRIGHTNESS TEMPERATURES.....	25
5	KEY INTERFACES	26
5.1	ALGORITHM INPUT	26
5.1.1	<i>General Requirements for Input Data</i>	26
5.1.2	<i>Geolocation Input</i>	27
5.1.3	<i>On-Orbit Instrument Data</i>	27
5.1.4	<i>External Input Data</i>	28
5.2	ALGORITHM OUTPUT.....	29
5.3	USER INTERFACE DESIGN AND CODE STRUCTURE.....	30
5.4	FORMAT AND RANGE FOR SUBMODULE I/O.....	31
5.5	MISSING OBSERVATIONS AND EXCEPTION FLAG.....	34
5.6	OTHER ERRORS AND EXCEPTIONS	37
6	RADIOMETRIC CALIBRATION	39
6.1	BASELINE RADIOMETRIC CALIBRATION	39
6.1.1	<i>Radiometric Transfer Function</i>	39
6.1.2	<i>Gain and Offset at Reference Tie Point Temperature 3K and 300K</i>	42
6.1.3	<i>Determination of Ground Non-Linearity</i>	42
6.2	ON-ORBIT RETRIEVAL OF CALIBRATION PARAMETERS AND TRENDING.....	42
6.2.1	<i>Determination and Trending of Non-Linearity</i>	42
6.2.2	<i>Determination and Trending of Noise-Diode Coupled Temperature</i>	43
6.2.3	<i>Calibration Point Consistency Check</i>	43
6.2.4	<i>Trending of Gain and Offset</i>	44
6.3	HOT-LOAD BACKUP RADIOMETRIC CALIBRATION	44
6.4	PRECIPITATION RADAR BLANKING CORRECTION	44

6.5 ON-ORBIT NEDT VERIFICATION	47
7 ANTENNA PATTERN THEORY.....	48
7.1 VECTOR EFFECTIVE HEIGHT	48
7.2 INCIDENT AND RECEIVED FIELDS	48
7.3 INCIDENT AND RECEIVED POWER – STOKES VECTOR.....	49
7.4 POLARIZATION BASIS ROTATION.....	51
7.5 BATC ANTENNA PATTERNS.....	53
7.5.1 BATC Patterns in the MRCS.....	53
7.5.2 Port Symmetry.....	54
7.5.3 Consistency Checks.....	54
7.5.4 Scanning.....	55
7.5.5 Transformation of the Antenna Patterns into the MBS	55
7.6 POLARIZATION BASIS ALIGNMENT	56
7.6.1 Earth V-H Basis	56
7.6.2 S/C V-H Basis	56
7.6.3 Aligning the S/C V-H Basis with the Polarization Basis of the Antenna Pattern.....	56
7.6.4 Principal Plane Cuts of the Antenna Patterns in the V-H Basis	58
7.7 TRANSFORMATION BETWEEN EARTH BRIGHTNESS TEMPERATURES AND ANTENNA TEMPERATURES	59
7.7.1 Faraday Rotation.....	59
7.7.2 Polarization Basis at Boresight	59
7.7.3 Polarization Rotation due to Deviation of the S/C Attitude from the Nominal Attitude.....	60
7.7.4 Full Transformation form Brightness Temperatures into Antenna Temperatures	60
8 ORBIT SIMULATOR	61
8.1 PURPOSE AND OVERVIEW	61
8.2 S/C ORBIT SIMULATION	62
8.3 SWATH SIMULATION.....	63
8.4 TOA BRIGHTNESS TEMPERATURE SIMULATION	64
8.5 RADIATIVE TRANSFER MODEL	65
8.6 ANTENNA TEMPERATURE SIMULATION	68
8.7 RADIOMETER COUNT SIMULATION.....	68
9 ANTENNA PATTERN CORRECTION	69
9.1 PURPOSE AND GENERAL METHOD	69
9.2 ANTENNA PATTERN CORRECTION FOR EMISSIVE MAIN REFLECTOR	70
9.3 DETERMINATION OF THE APC COEFFICIENTS	71
9.3.1 Conventional Method: Antenna Pattern Integration.....	71
9.3.2 Determination of the APC Coefficients from Orbit Simulator	72
9.4 ANTENNA PATTERN CORRECTION FOR SINGLE POLARIZATION FREQUENCIES.....	72
10 PRE-LAUNCH VERIFICATION AND TESTING.....	74
10.1 CALIBRATION UNCERTAINTY ERRORS AND ERROR BUDGETING	74
10.2 ERROR SOURCES AND VERIFICATION OF THE COLD CALIBRATION	74
10.3 ERROR SOURCES AND VERIFICATION OF THE HOT CALIBRATION	76
10.4 ERROR SOURCES AND VERIFICATION OF THE APC	78
10.4.1 Error of the APC.....	78
10.4.2 Contribution from Sidelobes, Backlobes and Cross Polarization.....	79
10.4.3 Knowledge Error in the Antenna Patterns.....	79
10.4.4 Knowledge Error in the Main Reflector (MR) Emissivity and Temperature.....	80
10.4.5 Contamination from Instrument, S/C and Strut	80
10.5 ERROR SOURCES AND VERIFICATION OF THE NON-LINEARITY CORRECTION	80
10.6 VERIFICATION OF THE CALIBRATION UNCERTAINTY	81
10.7 TESTING OF FUNCTIONAL REQUIREMENTS	81
11 SENSOR AND CALIBRATION ANOMALIES.....	82
11.1 MOON INTRUSION INTO THE COLD SKY VIEW	82
11.2 RFI INTRUSION INTO THE COLD SKY VIEW	85
11.3 RFI AND SUN GLINT FLAGGING.....	86

11.3.1 RFI Glint Flagging.....	86
11.3.2 Sun Glint Flagging.....	89
11.4 EARTH INTRUSION INTO THE COLD SKY VIEW.....	89
11.5 SUN INTRUSION INTO THE HOT LOAD.....	90
12 POST-LAUNCH CALIBRATION AND VALIDATION.....	94
12.1 BASIC TOOL FOR POST-LAUNCH CALIBRATION MEASURED VERSUS COMPUTED BRIGHTNESS TEMPERATURES.....	94
12.2 ANALYSIS AND CORRECTION OF SENSOR POINTING ERRORS.....	95
12.3 ANALYSIS AND CORRECTION OF ALONG-SCAN BIASES AND ORBITAL-POSITION DEPENDENT BIASES IN THE EARTH VIEW SECTOR.....	97
12.4 CORRECTION OF CALIBRATION SYSTEM ANOMALIES.....	98
12.5 ANALYSIS AND CORRECTION OF ALONG-SCAN BIASES IN THE CALIBRATION COUNTS.....	98
12.6 ABSOLUTE CALIBRATION.....	99
APPENDIX A COORDINATE SYSTEMS AND TRANSFORMATIONS.....	101
A.1 EARTH CENTERED INERTIAL SYSTEM (<i>ECI</i>).....	101
A.2 GEODETIC SYSTEM.....	101
A.3 GAUSS SYSTEM.....	102
A.4 TRANSFORMATION BETWEEN GAUSS AND <i>ECI</i> SYSTEMS.....	102
A.5 IN-FLIGHT S/C SYSTEM (<i>F</i>) AND GMI SYSTEM.....	104
A.6 MAIN REFLECTOR COORDINATE SYSTEM (<i>MRCS</i>).....	105
A.7 MAIN BEAM SYSTEM (<i>MBS</i>).....	106
APPENDIX B GEOLOCATION.....	108
APPENDIX C OPTIMUM INTERPOLATION AND NEAR-SIDELOBE CORRECTIONS.....	110
C.1 OPTIMUM INTERPOLATION.....	110
C.2 RESAMPLING AND COMPOSITE FIELD OF VIEW.....	114
C.3 NEAR-SIDELOBE CORRECTIONS.....	116
APPENDIX D PLANCK FUNCTION, RAYLEIGH-JEANS APPROXIMATION AND EFFECTIVE COLD SPACE TEMPERATURES.....	117

List of Figures

Figure 1: GMI instrument stowed configuration	11
Figure 2: GMI instrument deployed configuration.....	12
Figure 3: Calibration assembly configuration. Taken from PDR Day 4-5: Calibration Assembly (Randy Keller).	13
Figure 4: GMI hot load. Taken from PDR Day 4-5: Calibration Assembly (Randy Keller).	14
Figure 5: Cold sky reflector all space pattern for 10.65GHz cold ample (stare) number 1 out of 4. Taken from PDR Day 2-8: Cold Sky Reflector Design & Performance (Leo Diaz).....	15
Figure 6: Top level flow diagram for the GMI calibration algorithm.	20
Figure 7: Flowchart for the cold calibration algorithm.....	21
Figure 8: Flowchart for the hot calibration algorithm.	22
Figure 9: Flowchart for the calibration parameter module.	24
Figure 10: Flowchart for the Earth count to TA module.	25
Figure 11: Flowchart for the antenna pattern correction (APC) module.	25
Figure 12: User interfacing diagram: Calling and linking for the cold calibration module as example.....	30
Figure 13: Principal plane cuts of the 10.65 GHz patterns in the <i>MBS</i> v/h basis. The full lines are co-pol (vv and hh), the dashed lines are cross pol (vh and hv). The blue lines are the cuts in the plane $\phi = 0^\circ$ (positive θ) / $\phi = 180^\circ$ (negative θ). The green lines are the cuts in the plane $\phi = +90^\circ$ (positive θ) / $\phi = -90^\circ$ (negative θ). The plots are displaying the values $\frac{1}{2}4\pi f_{vv} ^2$ and $\frac{1}{2}4\pi f_{vh} ^2$, respectively.	58
Figure 14: Schematic overview of the orbit simulator.....	61
Figure 15: GMI swath (green) over S/C ground track. The longitude of the ascending equatorial crossing is 40° E.....	63
Figure 16: TOA TB simulation for the 10.65 GHz h-pol channel using the swath of Figure 15.	64
Figure 17: TOA TB simulation for the 36.5 GHz h-pol channel using the swath of Figure 15.....	65
Figure 18: Pre-launch verification scheme of the APC based on the orbit simulator.....	78
Figure 19: Cold count map for SSMIS 37V before correction of moon intrusion. The x-axis is time (orbit # or day since the starting orbit). The y-axis is the intra-orbit position (fractional rev #).	83
Figure 20: Cold count map for SSMIS 37V after correction of moon intrusion.	83
Figure 21: WindSat 10.7 GHz cold swath of orbit # 10200 showing moon and RFI intrusion.	84

Figure 22: WindSat 10.7 GHz cold swath of orbit # 10200 after applying the statistical filter.....	84
Figure 23: Absolute value of the RFI glint angle between the WindSat boresight and the geostationary TV satellite PAS-3R at 43.0° longitude.....	88
Figure 24: Brightness temperature difference between the WindSat 10 H-pol and 6 H-pol for the ascending forward looking swath. The maps show the averages of all orbits between rev# 2900 and rev# 7000. The left panel shows the result without applying the RFI glint flag. The right panel shows the result after events that were flagged for RFI were excluded from the data set.....	88
Figure 25: Earth map of cold counts for the 6H channel: Upper panel before, lower panel after doing the correction.	90
Figure 26: WindSat 18.7 GHz $2T_{A,v} - T_{A,h}$ measured – computed as a function of orbit number (rev #) and orbital angle.....	91
Figure 27: Gain as function of orbital angle for orbit # 1601. The black curve is the gain using the average thermistor temperatures (no hot load anomaly correction). The red curve is the gain after applying $\Delta T_{eff}(\beta)$. The green curve is the final gain after smoothing by fitting it to the cold counts + 2 nd order harmonics in z . The blue curve is $\Delta T_{eff}(\beta)$ shifted by 288K.	93
Figure 28: Descending minus ascending maps of SSMIS channel 18H for 500 (about 1 months) orbits with no nadir angle adjustment.	96
Figure 29: Descending minus ascending maps of SSMIS channel 18H for 500 (about 1 months) orbits after adjusting the nadir angle by -0.12°.....	96
Figure 30: WindSat Level 2 brightness temperatures for the 37V channel at 4 different resolutions. The figure shows a rain band in the ITCZ just north of the equator in the central Pacific in December. The missing part on the swath of the 56 km is due to the fact that there are no 6.8 GHz observations and for producing the figures all channels at a given resolution were required.....	115
Figure 31: Deviation $\delta = \Theta - T$ of the Planck Brightness Temperature Θ (231) from the physical temperature T (RJ approximation) for the GMI frequencies.	118

List of Tables

Table 1: Reference for important instrument and orbital parameters	16
Table 2: Key functional requirements that drive the design of the algorithm. The section and ID numbers are from BATC 2281975.	17
Table 3: Key performance requirements that drive the design of the algorithm. The section and ID numbers are from BATC 2281975.	18
Table 4: List of derived requirements for the GMI calibration algorithm.	19
Table 5: Required instrument characteristics input for the pre-launch verification and testing that is to be supplied by BATC.	19
Table 6: Dimensional parameters.	26
Table 7: Geolocation input for the calibration algorithm.	27
Table 8: On-orbit instrument input data for the calibration algorithm.	27
Table 9: On-orbit instrument data for trending of noise-diode and non-linearity.	28
Table 10: External input data to the calibration algorithm.	28
Table 11: Output of the calibration algorithm.	29
Table 12: I/O Format and valid range of variables for subroutine <i>cold_calibration</i> (cold calibration module).	31
Table 13: I/O Format and valid range of variables for subroutine <i>hot_calibration</i> (hot calibration module).	31
Table 14: I/O Format and valid range of variables for subroutine <i>calibration_par_4pt</i> (calibration parameter module).	32
Table 15: I/O Format and valid range of variables for subroutine <i>calibration_par_2pt</i> (calibration parameter module).	32
Table 16: I/O Format and valid range of variables for subroutine <i>calibration_cons</i> (calibration parameter module).	33
Table 17: Format and valid range of variables for subroutine <i>count_to_ta_1</i> Earth TA module in normal mode, option 1: using cold and hot counts w/o noise diode as input.	33
Table 18: Format and valid range of variables for subroutine <i>count_to_ta_2</i> Earth TA module in normal mode, option 2: using gain and offset at reference temperatures (3K and 300 K) as input.	33
Table 19: Format and valid range of variables for subroutine <i>count_to_ta_bkp</i> Earth TA module in hot-load backup mode: use cold counts with and w/o noise diode as input.	34
Table 20: Format and valid range of variables for subroutine <i>ta_to_tb</i> (APC module).	34
Table 21: Placeholders for missing input and output in the master subroutines.	35
Table 22: Exception handling and Q/C flag.	35
Table 23: Geostationary TV satellites causing RFI intrusion for the WindSat 10.7 GHz channels.	87

Table 24: Values for spillover and cross polarization contamination for WindSat from the NRL pre-launch antenna pattern measurements and the RSS post-launch absolute calibration.	100
Table 25: Off-nadir angles θ_N and off-track angles φ_0 for the GMI channels. Taken from PDR Day2-8: Main Reflector Design & Performance (Leo Diaz).	107
Table 26: Values for the effective temperature of cold space accounting for the deviation of the RJ approximation from the Planck law for the GMI frequencies.	119

1 Introduction and Overview

1.1 Purpose of the GMI Calibration Algorithm

The goal of the calibration algorithm for the Global Precipitation Measurement (GPM) Microwave Imager (GMI) is the conversion of Level 1A radiometer Earth and calibration counts from the science and housekeeping telemetry data packets into Level 1B calibrated top of atmosphere (TOA) brightness temperatures.

The GMI calibration algorithm follows closely the algorithms that have been developed by Remote Sensing Systems (RSS) for other radiometers, e.g.: the special sensor microwave imager SSM/I, the tropical rainfall mission (TRMM) microwave imager TMI, the advanced microwave scanning radiometer AMSR, the WindSat microwave radiometer and the special sensor microwave imager and sounder SSMIS. There are some deviations from the RSS algorithms to account for unique products from GMI, such as 4-point calibration, non-linearity retrieval, noise diode coupled temperature determination, and hot load backup functionality.

1.2 Purpose and Contents of ATBD

The purpose of this ATBD is to:

1. Describe the functionality of the GMI calibration system.
2. Give an overview of the physical background that underlies the GMI calibration method.
3. Describe the structure and the functionality of all the submodules of the GMI calibration algorithm.
4. Derive all the necessary equations and mathematical relations that will be used in the software.
5. Explain in detail how the user is interfacing with those submodules and how the submodules are interfacing with each other.
6. Describe how the algorithm is verified against its requirements and how the error budgets are derived.
7. Outline the main steps of the post-launch calibration and validation.

This ATBD is organized as follows:

Chapter 2 contains a short description of the GMI instrument and its subsystems including the in-flight calibration system. Chapter 3 lists the key functional and performance requirements that drive the design of the GMI calibration algorithm and also list all other requirements that the algorithm will need. In chapter 4 we show the flow diagram for the algorithm, demonstrate how the algorithm is structured into various submodules and give a short description of the functionality of each of these submodules. We also show how these submodules are linked together. Chapter 5 describes the interface between the submodules and the submodules and the user. It lists the content and the format of all the input that algorithm needs and the output that it produces. Chapter 6 gives a general account of the radiometric calibration method and derives the necessary relations. Chapter 7 contains a short overview of the basic theory of antenna patterns. In chapter 8 we explain the steps and features of the end to end in-flight orbit simulator, which simulates radiometer measurements from realistic environmental scenes based on the theory of radiative transfer. A central part of the GMI calibration algorithm is the transformation of measured antenna temperatures into TOA brightness temperatures, which is known as antenna pattern correction (APC). This

method is described in chapter 9. Chapter 10 explains how the performance requirements of the algorithm are verified and the error budgets are derived. In chapter 11 we give a short description of anomalies that have been observed at heritage radiometer instruments and show methods how those anomalies can be corrected. Chapter 12 contains and describes the steps of the post-launch calibration and validation plan.

1.3 Applicable and Supplemental Documents

- BATC 2281975: GMI Calibration Algorithm Requirements and Interfaces Specifications (Revision F, September 26, 2008)
- Global Precipitation Measurement Microwave Imager (GMI) PDR, November 13 – 17, 2006 (PowerPoint slides).
- BATC 2249401: NEDT Performance and Error Budget.
- BATC 2249262: GMI On-orbit Calibration Uncertainty Performance and Error Budget.
- BATC 2245942: Calibration Management Plan and Models for GMI.
- BATC 2298950: GMI Ground Calibration Error Budget.
- BATC 2345335: GMI Hot Load Calibration Error Assessment
- RSS Memo from 22 April 2009: Distribution of V – H Pol at TB at 23.8, 165.5 and 183.3 GHz.
- RSS Memo from 23 September 2010: Antenna Pattern Correction (Version 1).
- RSS Memo from 12 November 2009: Monte Carlo Simulation of GMI Radiometric Calibration: Calibration Count Averaging - Retrieval of Radiometer Gain and Offset.

2 GMI Instrument and Calibration System

In this section a brief description is given for the Global Precipitation Measurement Microwave Imager being built by BATC under contract to GSFC. GMI is the microwave imager that will fly on the GPM Core satellite with the Japanese supplied Ku- and Ka-band radars to provide collocated precipitation retrieval to improve precipitation retrieval of space borne radiometers. GMI will also fly on the GPM Constellation satellite to improve latency of precipitation retrieval.

2.1 Instrument

The purpose of the GMI is to collect global microwave radiometry. The GMI Instrument will operate continuously after being placed on orbit. The instrument consists of all hardware and software to collect radiometric data, perform instrument calibration, and send GMI Science Data Records (GSDRs) and GMI Housekeeping Data Records (GHDRs) to the spacecraft for transmission to the GMI ground station. The data will be processed to produce microwave imagery and other specialized meteorological data using algorithms developed by the government. The GMI Instrument is shown in Figure 1 in its stowed and in Figure 2 deployed configuration.

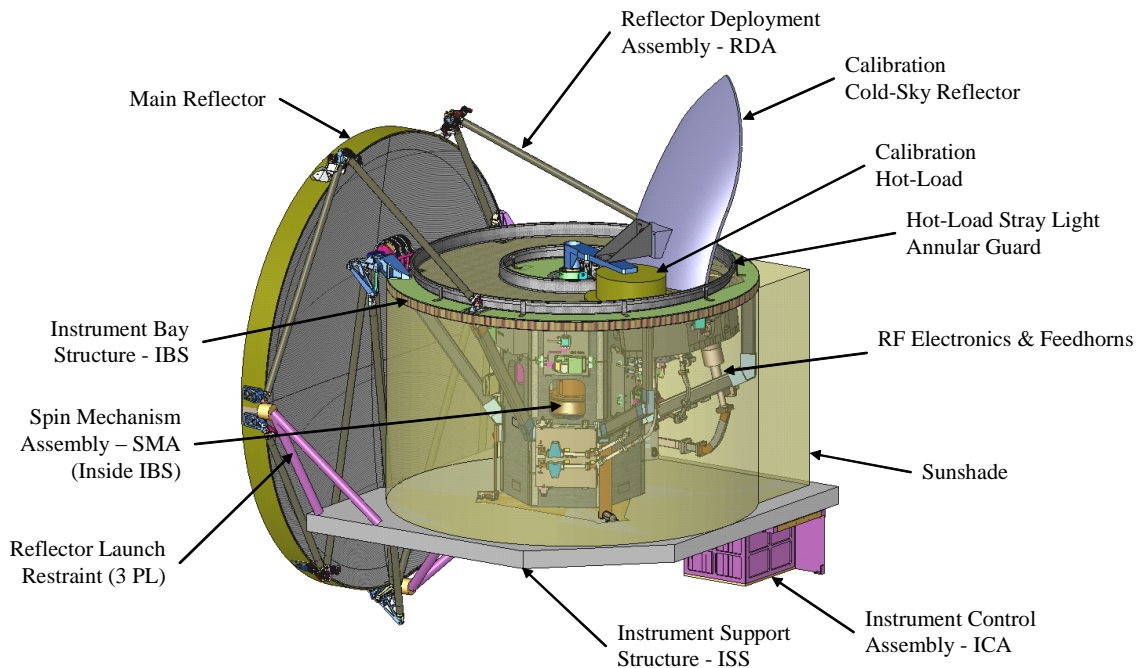


Figure 1: GMI instrument stowed configuration

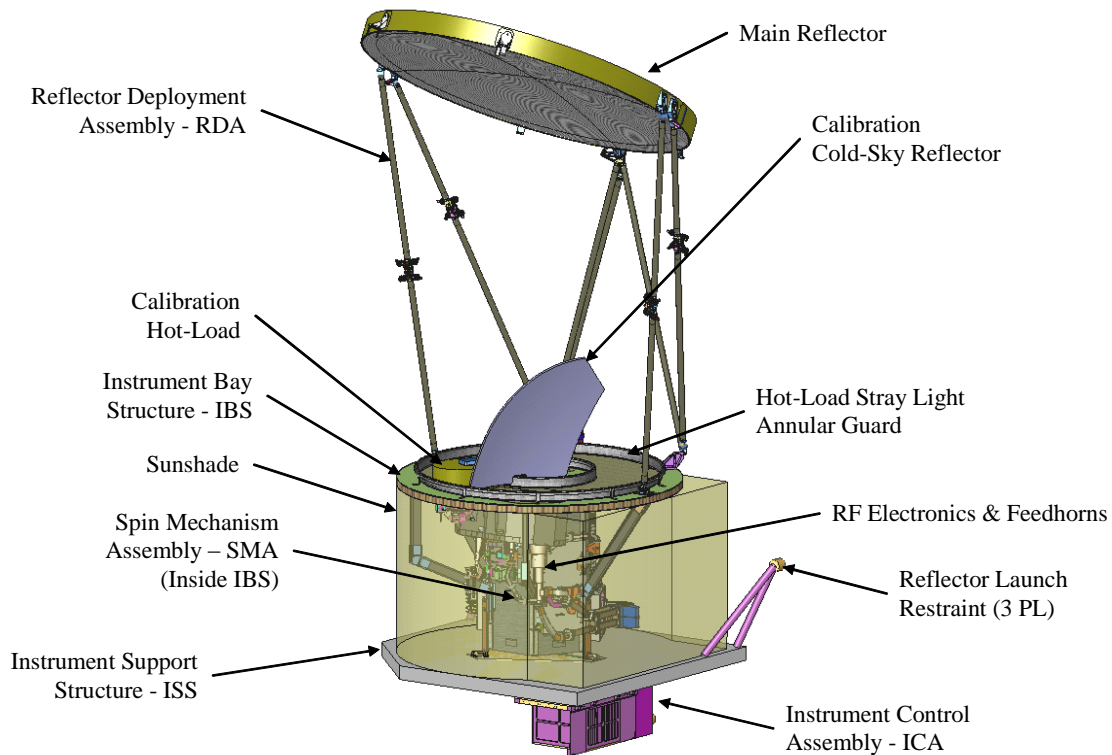


Figure 2: GMI instrument deployed configuration

2.1.1 Receiver Subsystem

The Receiver Subsystem receives microwave energy from the Antenna Subsystem as input, processes the frequency bands of interest and delivers digital data as output to the Instrument Controller Assembly (ICA) for transmission to the ground stations. The Receiver Subsystem consists of the microwave receivers, RF Digital Interface and Control, power supplies and electronic power conditioning (EPC), RF analog telemetry, including analog to digital converters, buffers, multiplexers, and Data Bus interface and input and output devices required to convert microwave energy delivered by the Antenna Subsystem into digital data and telemetry data delivered to the Command and Data Subsystem.

The Receiver Subsystem design is a single string, modular, total power radiometer. It employs GaAs based high electron mobility transistor / pseudomorphic high electron mobility transistor (HEMT/PHEMT) devices from 10 to 37 GHz and a mixer/ intermediate frequency (IF) preamplifier at 89, 166, and 183 GHz. Direct detect is used from 10 GHz to 23 GHz, 37 GHz uses a superhet with low noise amplifier (LNA) / mixer design, and 89, 166, and 183 GHz uses a superhet with mixer / IF preamp in dual sideband (DSB) mode. It has a total of thirteen (13) receivers for 10 vertical (V), 10 horizontal (H), 18V, 18H, 23V, 36V, 36H, 89 GHz V, 89 GHz H, 166 GHz V, 166 GHz H, 183.31+3 GHz V, 183.31+7 GHz V.

2.1.2 Antenna Subsystem

The Antenna Subsystem consists of the main antenna (reflector (MR) plus feed mechanical assembly), cold sky reflector (CSR), hot load, interconnecting waveguide, and noise diodes. The main reflector is a 1.22 m diameter thin membrane design with a vapor deposited aluminum (VDA) coating for high reflectivity (low emissivity), a SiO_x coating to prevent atomic oxygen erosion of the VDA, and a surface finish to limit solar concentration to less than 2.0 suns, multilayer insulation (MLI) for thermal control, and thermistors to measure

physical temperature. The cold sky reflector is a composite design with a VDA coating and a SiOx coating. The feed mechanical assembly includes the feeds (5), feed tray, alignment brackets, spacers and shims.

2.2 In-Flight Calibration System

GMI has similarity to other radiometers in that it measures radiation from two calibration loads, a cold sky view and a black body (hot load). GMI is distinct in that it also provides two additional measurements, a cold sky view with noise diode and hot load view with noise diode. Operational GMI has a calibration cycle that repeats every other scan rotation. On the first rotation, the cold sky view and the hot load are sampled and on the second rotation the cold sky view plus noise diode and hot load plus noise diode is sampled. This provides 4 calibration points, enough information to allow the excess noise temperature of the noise diodes and the nonlinearity of the receivers to be determined in addition to the gain and offset of the receivers.

Figure 3 shows the calibration assembly configuration. Cold sky reflector and hot load are stationary. That means they do not rotate with the instrument. The hot load tray mounts to the deck and rotates with the instrument. Its purpose is to provide thermal stability to the hot load and shield it from possible sun intrusion.

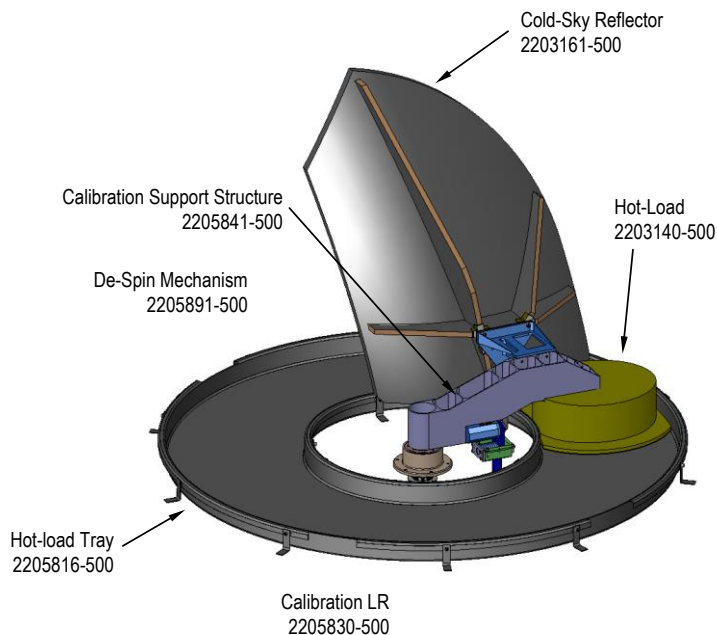


Figure 3: Calibration assembly configuration. Taken from PDR Day 4-5: Calibration Assembly (Randy Keller).

2.2.1 Hot Load View

The hot load consists of a non-rotating calibration target that intercepts the line-of-sight between the feedhorns and the main reflector as the feedhorns pass beneath the hot calibration load during each scan. The temperature of the hot load is passively controlled and will be between 240 K and 330 K over all on-orbit conditions. The hot load is an elliptical shape. It is made up of pyramidal shaped metal structures coated with an absorbing material called eccosorb. Figure 4 shows the GMI hot load calibration target. The pyramids are about 0.5” square by about 2.7” tall. The thickness of the base limits the temperature gradients across the load and the pyramid design in concert with the eccosorb allows the emissivity to be ~

1.0. The load was sized to allow a minimum of 4 measurements per view for all channels. The hot load is sampled multiple times per rotation of the main reflector and the samples are averaged over multiple rotations to minimize the effect of thermal noise.

The emissivity of the hot load is required to be greater than 0.9992 for 10-89 GHz and greater than 0.9999 for 165.5 and 183.3 GHz to provide limit the reflections from the load that will cause the observed brightness temperature to vary from the radiated brightness temperature. This is especially true of 165.5 and 183.3 GHz, where the local oscillator (LO) leakage is higher. The target is not thermally controlled as this would introduce undesirable gradients. However, the hot load is highly isolated to limit temporal changes in the brightness temperature. At least eleven (11) thermistors (PRTs) are embedded in the hot load and will be available during on-orbit operations. All of these PRTs are located in the tips of the hot load pyramids to lower the temperature uncertainty between the PRTs and the surface of the eccosorb coating, which will provide lower temperature uncertainty for the hot load view. Most of the PRTs are located along the arcs traversed by the feed horns to limit the impact of horizontal gradients. In order to possibly correct for vertical temperature gradients there is an additional PRT placed at the hot load tray and one of the pyramids has a two PRTs: one in its base and one in its tip.

A common problem with hot calibration targets has occurred and been observed at several instruments (AMSR, WindSat, SSMIS) in more or less stronger form: At certain points in the orbit or at certain times sun light hits the hot load and can cause additional gradients which cause its effective temperature to deviate from what the PRTs read. The GMI hot load design is such that this effect is minimized using a rim around the hot load to block possible solar intrusion. However it will still need to be analyzed during the post-launch calibration and validation and, if necessary, we will need to derive a correction similar to how we have done it for the other instruments.

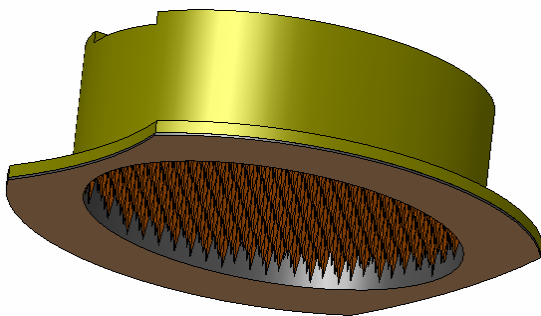


Figure 4: GMI hot load. Taken from PDR Day 4-5: Calibration Assembly (Randy Keller).

2.2.2 Cold Sky View

The cold calibration point is provided by the cold sky reflector (CSR) which allows the feed horns view approximately 2.7 K and obtain a cold calibration point. The cold sky view is also sampled multiple times per rotation of the main reflector and the samples are averaged over multiple rotations of the main reflector. The cold sky view is a more complex combination of sources than the hot load. Contributions other than from cold space come from reflections and emission from the instrument. There is also Earth view intrusion into the cold sky view primarily through the back lobe of the CSR. The back lobe looks at the main reflector, which sees the earth. The CSR is tilted up at a sufficient angle that little contamination comes from the earth directly. The cold sky reflector is sized to mitigate contamination

through the backlobe. Figure 5 shows the antenna pattern of the CSR over 4π steradians. As can be seen, there are contributions from several sources that may need to be determined to arrive at the true cold sky view temperature.

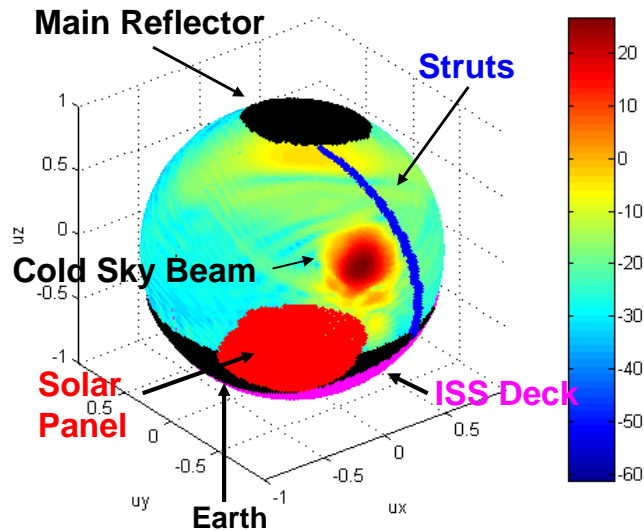


Figure 5: Cold sky reflector all space pattern for 10.65 GHz cold ample (stare) number 1 out of 4. Taken from PDR Day 2-8: Cold Sky Reflector Design & Performance (Leo Diaz).

In addition the orbital and cold sky view geometry makes it inevitable that the moon intrudes into the cold sky view. This lunar intrusion has been clearly observed at many other satellite microwave radiometers that employ cold sky calibration (SSM/I, SSMIS, TMI, AMSR, WindSat).

It is one goal of the calibration algorithm is to remove the most important of these contaminations of the cold sky view.

2.2.3 Noise Diodes

The noise diodes provide an additional source of calibration. The noise diodes are incorporated into channels 1-7 and will raise the receiver noise temperature by $220 K \pm 75 K$ over all conditions. The noise diodes will be switched on and off at every other scan rotation. The noise diodes operate in concert with the hot load and cold sky view to provide two additional calibration points, cold sky view with noise diode and hot load with noise diode. These two additional points allow for determination of two additional quantities. In addition to the gain and offset, nonlinearity and noise diode coupled temperature are also determined. That the noise diode coupled temperature is determined as a byproduct of the calibration process means that they do not need to be ultra stable. The nonlinearity and noise diode coupled temperature can be trended over temperature and life. If statistically significant changes to nonlinearity occur relative to the pre-launch characterization, the input nonlinearity can be updated versus instrument temperature.

2.3 Reference Values

For reference, Table 1 lists the nominal values of important orbital and instrument parameters that will be used in the calibration algorithm. The values for the half power beam widths are at the requirement level.

Table 1: Reference for important instrument and orbital parameters

channel #	center frequency [GHz]	pol	nadir angle (nom) [deg]	Earth incidence angle (nom) [deg]	beam width [deg]	footprint [km x km]	cold samples per scan (approx)	hot samples per scan (approx)	Earth samples per scan (nom)	band width [MHz]
1,2	10.65	v/h	48.5	52.821	1.72	32.1 x 19.4	14	4	211	100
3,4	18.7	v/h	48.5	52.821	0.98	18.1 x 10.9	26	9	211	200
5	23.8	v	48.5	52.821	0.85	16.0 x 9.7	26	9	211	400
6,7	36.64	v/h	48.5	52.821	0.81	15.6 x 9.4	42	15	211	1000
8,9	89	v/h	48.5	52.821	0.38	7.2 x 4.4	42	20	211	6000
10,11	166.0	v/h	45.36	49.195	0.37	6.3 x 4.1	42	25	211	3400
12,13	183.31 +/-3	v	45.36	49.195	0.37	5.8 x 3.8	42	25	211	2000
	183.31 +/-7									2000
Nominal altitude: 407 km Orbital inclination: 65 deg Spin Rate: 32 rpm Scan Time: 1.875 sec Swath width: 885 km Earth viewing sector: 146.2 deg Earth samples: 211 Integration time: 3.6 msec = (146.2/360) x 1.875 sec / 211 Dish Size: 1.22 m										

3 Key Requirements

3.1 Functional Requirements

The design of the algorithm is driven by the following key functional requirements listed in Table 2.

Table 2: Key functional requirements that drive the design of the algorithm. The section and ID numbers are from BATC 2281975.

Section	ID	Functional Requirement	
3.2.1	122	The GMI Calibration Algorithm shall compute the top of atmosphere brightness temperature for the antenna main beam of each channel for each effective field of view (EFOV) measured by the instrument.	General
3.2.3	124	The GMI calibration algorithm shall convert from measured receiver counts to main-antenna brightness temperature using the radiometer science measurements, hot-load observations, cold-sky observations, and nonlinearity data.	Radiometric Calibration
3.2.4	126	The GMI calibration algorithm shall be capable of performing radiometric calibration without the real-time hot load measurements for channels 1-7. This capability is termed the "Hot Load Backup."	Hot Load Backup Functionality
3.2.4	127	The Hot Load Backup functionality shall use the trended noise-diode coupled temperature and the "cold sky + noise diode" measurements as a substitute for the hot-load measurement.	
3.2.5	169	The GMI calibration algorithm shall compute the brightness temperature observed by the feeds during the hot load observation using the hot load physical temperature measurements.	Hot Load Brightness Temperature Determination
3.2.5	170	The GMI calibration algorithm shall correct the hot load observation for constant and scan-dependent biases. The corrections may be performed on either or both the computed brightness temperature or on the measured counts as deemed necessary.	
3.2.5	171	The GMI calibration algorithm shall compute quality checks on the computed hot load brightness temperature and discard data that do not meet a pre-determined set of criteria. RSS shall document the criteria in the ATBD.	
3.2.5	172	The GMI calibration algorithm shall compute quality checks on the hot load radiometer measurements and discard data that do not meet a pre-determined set of criteria. RSS shall document the criteria in the ATBD.	
3.2.5	328	The GMI calibration algorithm shall combine multiple hot load samples taken during a single scan.	
3.2.5	173	The GMI calibration algorithm shall combine the hot load observations from multiple scans.	
3.2.5	175	The GMI calibration algorithm shall determine the brightness temperature observed by the instrument during the cold sky observation.	
3.2.6	176	If necessary in order to meet performance requirements, the GMI calibration algorithm shall use the measured cold sky antenna patterns to correct for Earth contamination through the cold sky sidelobes.	Cold Sky Brightness Temperature Determination
3.2.6	177	If necessary in order to meet performance requirements, the GMI calibration algorithm shall correct for Earth and spacecraft contamination coming from the main antenna through the cold sky backlobe.	
3.2.6	179	The GMI calibration algorithm shall compute quality checks on the cold sky observations, and discard data that do not meet a pre-determined set of criteria. RSS shall document the criteria in the ATBD.	
3.2.6	180	The GMI calibration algorithm shall flag lunar contamination in the cold sky observation.	
3.2.6	331	The GMI calibration algorithm shall remove lunar contamination from the cold sky observation.	
3.2.6	181	The GMI calibration algorithm shall combine multiple cold sky samples taken during a single scan.	
3.2.6	182	The GMI calibration algorithm shall combine the cold sky observations from mul-	

		multiple scans.	
3.2.7	184	The GMI calibration algorithm shall correct for the nonlinearity of the receivers.	Noise Diodes and Non-linearity Correction
3.2.7	185	The GMI calibration algorithm shall be capable of using any of the following sources for nonlinearity correction: 1.Externally supplied ground-measured nonlinearity 2.Noise Diode-trended nonlinearity	
3.2.7	186	The GMI calibration algorithm shall compute the noise diode coupled temperature and the nonlinearity for each channel that uses noise diodes.	
3.2.7	187	A calibration cycle corresponds to the number of scans for which hot load and cold sky measurements are combined. The coupled temperature and nonlinearity shall be computed at least once per calibration cycle while the noise diodes are operating.	
3.2.7	188	The GMI calibration algorithm shall compute quality checks on the “hot load plus noise diode” and “cold sky plus noise diode” observations, and discard data that do not meet a pre-determined set of criteria. The criteria shall be documented in the ATBD.	
3.2.7	189	The nonlinearity shall be trended on-orbit at a minimum over the following set of parameters: 1.Receiver Physical Temperature 2.Receiver Gain Setting	
3.2.7	332	The noise diode coupled temperature shall be trended on-orbit at a minimum over the following parameters: 1.Noise Diode Physical Temperature	
3.2.8	191	The GMI calibration algorithm shall correct each measurement for main antenna pattern contributions coming from outside of the co-polarization main beam.	Antenna Pattern Correction
3.2.8	333	RSS shall determine which antenna pattern corrections are necessary in order to meet performance requirements.	
3.2.8	365	The GMI calibration algorithm shall correct each earth-scene measurement for cross-polarization contamination, contributions from cold space, and non-zero emissivity of the main reflector.	
3.2.8	366	The GMI calibration algorithm shall correct each Earth-scene measurement for the incidence angle dependence of the scene in the antenna sidelobes.	
3.2.8	367	The antenna pattern correction algorithm shall allow for correction of scan-dependent biases and orbital position-dependent that may be observed on-orbit. Such biases could originate from the spacecraft and instrument viewed by the sidelobes of the antenna.	
3.2.9	364	The GMI calibration algorithm shall correct each science measurement of channel 6 and 7 for variability in integration time due to asynchronous blanking of precipitation radar.	Precipitation Radar Blanking Correction

3.2 Performance Requirements

There are 5 top level performance requirements for the GMI calibration algorithm. They are listed in Table 3.

Table 3: Key performance requirements that drive the design of the algorithm. The section and ID numbers are from BATC 2281975.

Section	ID	Performance Requirement	
3.3.2	219	The calibration uncertainty for the GMI instrument shall be less than 1.35 K 3-sigma for channels 1-9 and 1.50 K 3-sigma for channels 10-13 over the earth scene dynamic range. Calibration uncertainty includes all error terms relating to calibrating a radiometer measurements on-orbit exclusive of the radiometric sensitivity (NEDT) from the scene sample. For definition of calibration uncertainty, measurement sample refers to the antenna main beam brightness temperature over homogeneous earth scenes.	Calibration Uncertainty
3.3.3	197	The hot load calibration shall contribute no more than 0.5 K 3-sigma error to the hot	Hot Load Brightness Tempera-

		load brightness temperature given the hot load characteristics in Table 3.3.3-1.	ture
3.3.4	203	The cold sky calibration shall contribute no more than 1.2 K 3-sigma error to the cold sky brightness temperature given the cold sky reflector characteristics in Table 3.3.4-1.	Cold Sky Brightness Temperature
3.3.5	209	The antenna pattern correction shall introduce an error of no more than 1.15 K 3-sigma given the main reflector and instrument characteristics given in Table 3.3.5-1.	Antenna Pattern Correction Error
3.3.6	247	The algorithm shall meet the calibration uncertainty with a non-linearity error of 0.2 K.	Nonlinearity Correction Error

3.3 Derived Requirements

The top level performance requirements of section 3.2 can be used to derive requirements for error sources that are a priori not sufficiently known.

Table 4 lists the requirements that we currently plan to derive from the performance requirements.

Table 4: List of derived requirements for the GMI calibration algorithm.

Derived Requirement	Driver	
Antenna Pattern Knowledge Error	Requirement on APC error (ID 209, Table 3)	If BATC does not supply errors in the antenna patterns.

3.4 Input Requirements for the Calibration Algorithm

The requirements of the calibration algorithm on input data are described in section 5.1.

3.5 Input Requirements for the Pre-Launch Verification Analysis

For development of the algorithm and the pre-launch verification analysis we expect to obtain the following instrument characteristics from BATC (Table 5):

Table 5: Required instrument characteristics input for the pre-launch verification and testing that is to be supplied by BATC.

A nominal curve $C=C(T)$ of radiometer counts as function of scene temperature or equivalently, nominal values for gain, offset and non-linearity, and how those parameters vary over the course of several representative orbits.
An nominal value for the noise diode coupled temperature T_n and how it varies over the course of several representative orbits.
Variation of cold sky reflector temperature together with the PRT readings over several representative orbits.
Cold sky reflector emissivity and its error.
Beam fractions for cold sky, Earth, instrument, S/C, strut for the cold sky view.
Variation of the hot load effective temperature together with the hot load PRT readings over several representative orbits.
Variation of hot load reflected brightness temperature, shroud physical temperature, shroud reflected brightness temperature and temperature of other warm hot load contamination sources over several representative orbits.
Beam fractions for hot load, shroud, gap, other warm contamination sources for the hot load view.
Emissivity of hot load and shroud.
Local oscillator (LO) leakage reflected from the hot load and cold sky reflector.
Variation of main reflector temperature together with the PRT readings over several representative orbits.
Main reflector emissivity and its error.
Brightness temperature of the instrument, S/C, strut over several representative orbits.
Antenna patterns (co pol and cross pol amplitude and phases for each port).
Knowledge error in the antenna patterns.
Blockage matrices of the parts of the antenna patterns that are blocked from instrument, S/C, strut.

4 Algorithm Structure and Submodules

4.1 Basic Flow

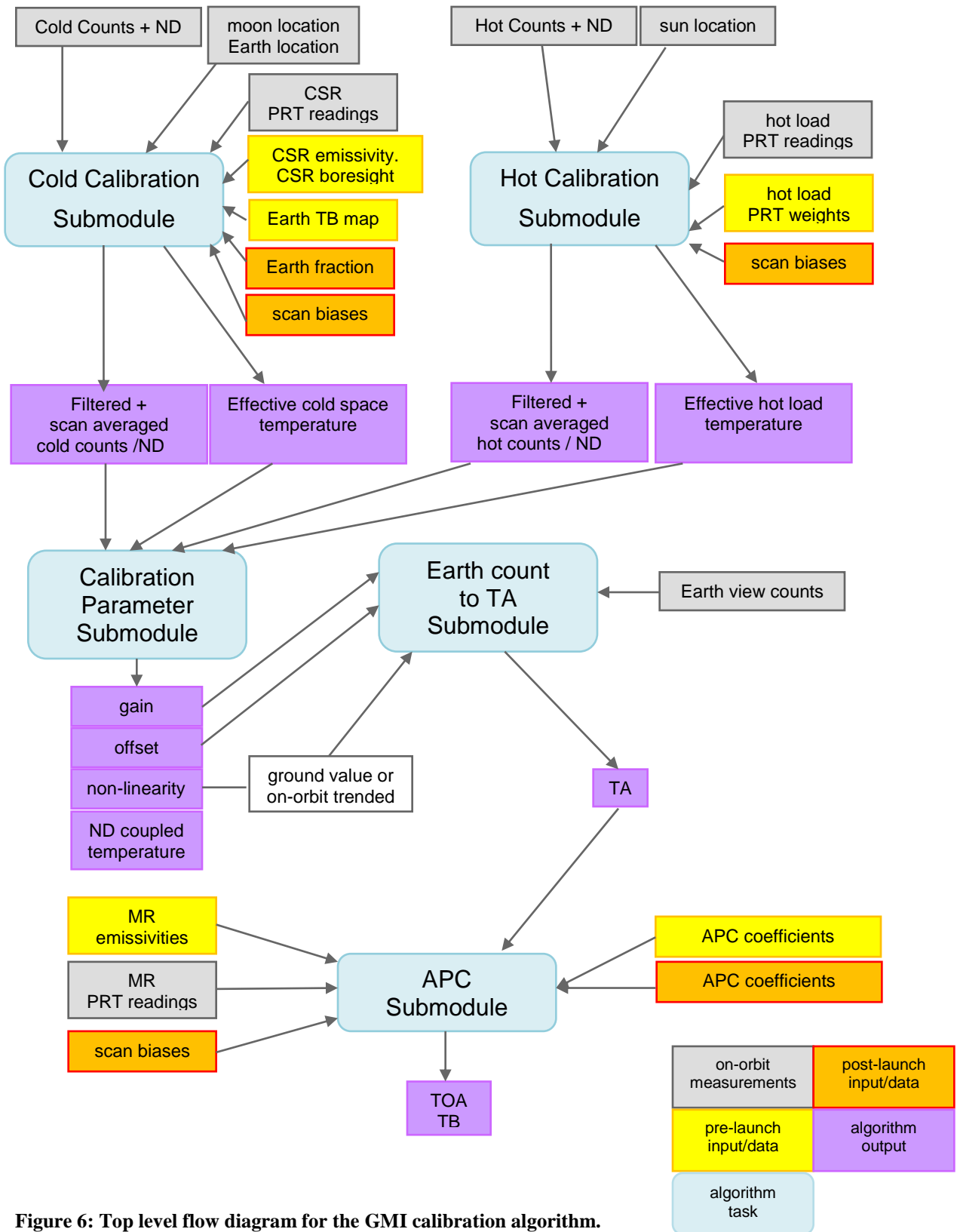


Figure 6: Top level flow diagram for the GMI calibration algorithm.

Figure 6 shows the top level flow diagram of the GMI calibration algorithm and its various components and submodules. They are explained in detail in the following sections.

4.2 Cold Calibration

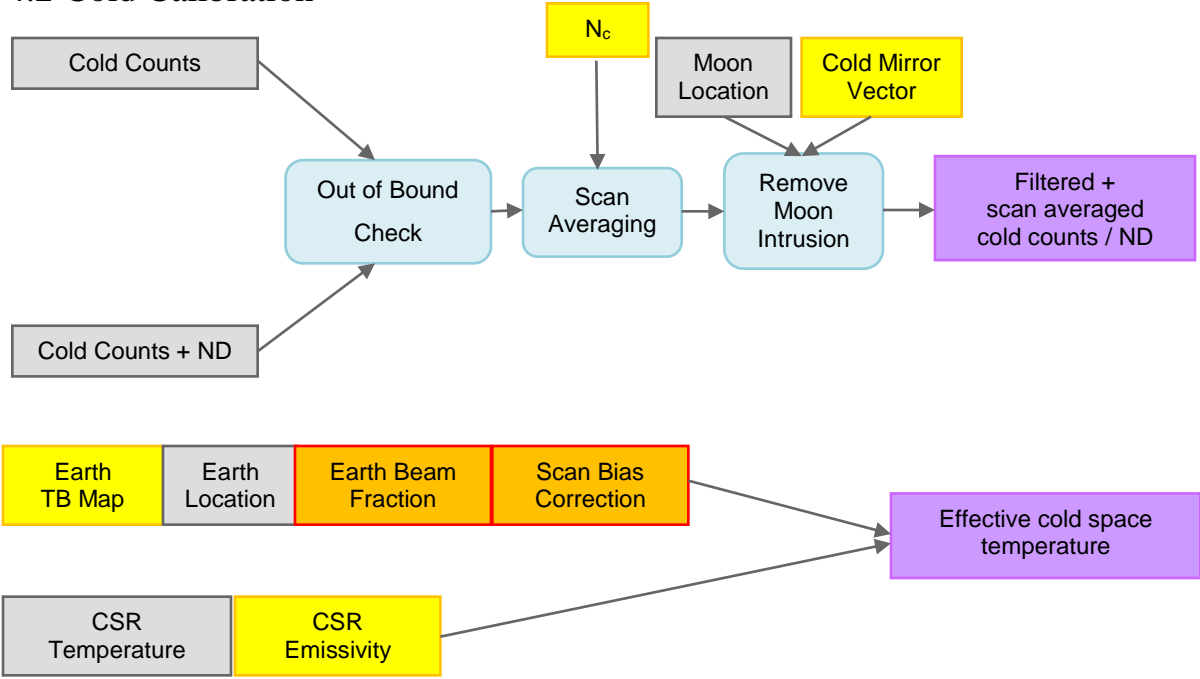


Figure 7: Flowchart for the cold calibration algorithm.

Figure 7 shows the flowchart for the cold calibration algorithm. The inputs are the counts of the cold sky view without and with noise diode injected temperature for each GMI channel. The counts are filtered for out of bound (OOB) values, such as negative or zero counts or unphysically large values. For each scan all valid counts are averaged over $\pm N_c$ scans before and after and the n_{cold} samples in each scan:

$$\bar{C}_c(i_{scan}) = \frac{\sum_{j_{scan}=i_{scan}-N_c}^{i_{scan}+N_c} \sum_{i_{cold}=1}^{n_{cold}} \Theta(j_{scan}, i_{cold}) \cdot C_c(j_{scan}, i_{cold})}{\sum_{j_{scan}=i_{scan}-N_c}^{i_{scan}+N_c} \sum_{i_{cold}=1}^{n_{cold}} \Theta(j_{scan}, i_{cold})} \quad (1)$$

$$\Theta \equiv \begin{cases} 1, & \text{if the observation is valid} \\ 0, & \text{if the observation is not valid} \end{cases}$$

The number N_c is determined from the requirements for the noise equivalent temperature (NEDT) of the cold calibration. The $\pm N_c$ window is effectively a time window. That means that the events in the cold count array need to be time ordered and if there are scans with missing observations, they need to be filled with placeholders for missing values as explained in section 5.5).

Each scan is flagged for moon intrusion into the cold mirror if the angle between the vector pointing from the S/C to the moon and the cold mirror vector is smaller than a threshold (section 11.1). In order to compute the average counts for the flagged scans, the algorithm linearly interpolates using unflagged scans before and after.

The cold calibration module computes an effective cold sky temperature for each GMI channel that accounts for intrusion of the cold sky view by radiation from the Earth and a finite emissivity of the cold sky reflector:

$$T_c^{eff} \approx (1 - E_{crefl}) \cdot T_c + E_{crefl} \cdot T_{crefl} + f_E \cdot T_{B,E} \quad (2)$$

where

E_{crefl} is the emissivity of the cold sky reflector, T_c is the temperature of cold space including deviations from the Rayleigh-Jeans (RJ) approximation (Appendix D), T_{crefl} is the temperature of the cold sky reflector, f_E is the beam fraction that falls on the Earth and $T_{B,E}$ is the brightness temperature of the radiation coming from the Earth.

The standard value for the cold space temperature T_c is 2.7 K. At higher frequencies it is necessary to include effectively the difference between the Rayleigh-Jeans approximation and the exact Planck law. The details are given in Appendix D .

The cold calibration module can also apply constant or scan position corrections to the cold sky temperature, which can arise from intrusion of the S/C, instrument or struts into the cold sky view. Those corrections will have to be derived post-launch (c.f. section 12.5).

4.3 Hot Calibration

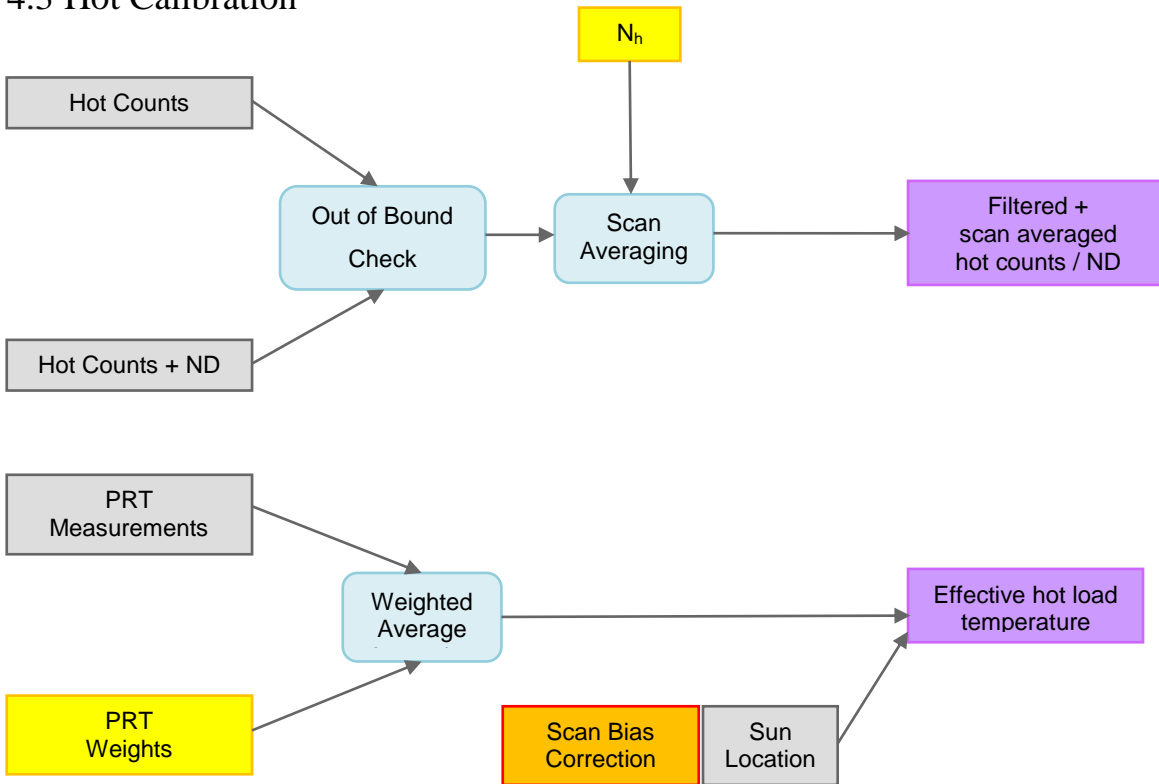


Figure 8: Flowchart for the hot calibration algorithm.

Figure 8 shows the flowchart for the hot calibration algorithm. The inputs are the counts of the hot load view without and with noise diode injected temperature of each GMI channel and the readings of the n_{PRT} hot load thermistors (PRT). The counts are filtered for out of bound (OOB) values, such as negative or zero counts or unphysically large values. For each scan all valid counts are averaged over $\pm N_h$ scans before and after and the n_{hot} samples in each scan.

$$\bar{C}_h(i_{scan}) = \frac{\sum_{j_{scan}=i_{scan}-N_h}^{i_{scan}+N_h} \sum_{i_{hot}=1}^{n_{hot}} \Theta(j_{scan}, i_{hot}) \cdot C_h(j_{scan}, i_{hot})}{\sum_{j_{scan}=i_{scan}-N_h}^{i_{scan}+N_h} \sum_{i_{hot}=1}^{n_{hot}} \Theta(j_{scan}, i_{hot})} \quad (3)$$

$$\Theta \equiv \begin{cases} 1, & \text{if the observation is valid} \\ 0, & \text{if the observation is not valid} \end{cases}$$

The number N_h is determined from the requirements for the NEDT of the hot calibration. The $\pm N_h$ window is effectively a time window. That means that the events in the hot count array need to be time ordered and if there are scans with missing observations, they need to be filled with placeholders for missing values as explained in section 5.5).

The effective hot load temperature T_h^{eff} is computed from the average of the $i = 1, \dots, n_{PRT}$ hot load PRT measurements T_i^{PRT} :

$$T_h^{eff} = w_0 + w_1 \cdot T_{PRT,ave} \quad (4)$$

where

$$T_{PRT,ave} = \frac{\sum_{i=1}^{n_{PRT}} (T_i^{PRT} + b_i^{PRT}) \cdot \Theta(i, j_{chan})}{\sum_{i=1}^{n_{PRT}} \Theta(i, j_{chan})} \quad (5)$$

$$\Theta = \begin{cases} 1, & \text{if the PRT is on the track of the feedhorn} \\ 0, & \text{if the PRT is not on the track of the feedhorn} \end{cases}$$

The weighting coefficients $w_i, i = 0, 1$ in (4) are computed using the BATC thermal model for the hot load. They depend on the horn as different horns see different areas of the hot load and can also depend on the hot sample. b_i^{PRT} is a constant (channel independent) bias of the PRT i which accounts for possible losses in the PRT wires.

The BATC thermal model shows that the error in T_h^{eff} using (4) is strongly correlated with the difference between the average hot load PRT reading $T_{PRT,ave}$ and the temperature reading of the PRT at the hot load tray $T_{PRT,tray}$. Therefore it is possible to derive a correction to (4) of the form

$$T_h^{eff} = [w_0 + w_1 T_{PRT,ave}] + [u_0 + u_1 (T_{PRT,tray} - T_{PRT,ave}) + u_2 (T_{PRT,tray} - T_{PRT,ave})^2 + u_3 (T_{PRT,tray} - T_{PRT,ave})^3] \quad (6)$$

which allows a more accurate calculation of the effective hot load temperature. For more details see: *BATC 2345335 Hot Load Calibration Error Assessment*.

The hot calibration module can also apply constant or scan position corrections to the effective hot load temperature, which can arise for example from intrusion of the cold pace into the hot load view. Those corrections will have to be derived post-launch (c.f. section 12.5).

4.4 Determination of Calibration Parameters

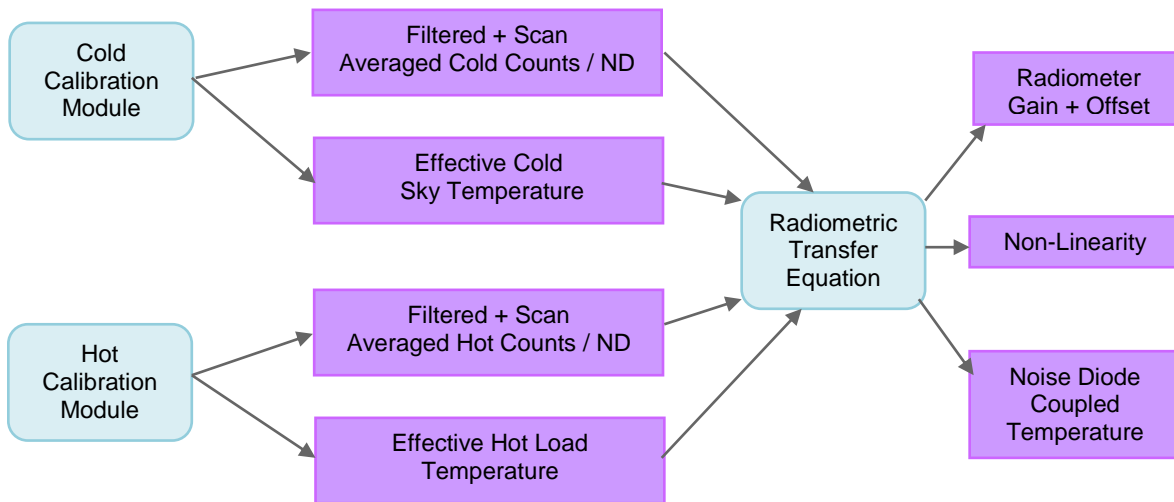


Figure 9: Flowchart for the calibration parameter module.

Figure 9 shows the flowchart for the determination of the calibration parameters. It uses the scan averaged hot and cold counts with and without noise diode injected temperature and the effective temperatures for hot load and cold sky view and computes the coupled temperature of the noise diode and the non-linearity. This is done for each GMI channel. For details see chapter 6.

4.5 Transformation from Radiometer Earth Measurements into Antenna Temperatures

Figure 10 shows the flowchart for the Earth count to TA module. This module uses the radiometer Earth measurements, the scan averaged hot and cold counts without noise diode, the effective temperatures for hot load and cold sky view and the non-linearity and computes the antenna temperature for each GMI channel. The Earth counts are filtered for out of bound (OOB) values, such as negative or zero counts or unphysically large values. The non-linearity can either be externally supplied using values from ground measurements, or one can use the value that was determined in section 4.4. Instead of the hot load calibration measurement, the algorithm can use the scan averaged cold counts with and without noise diode injected temperature together with the non-linearity and the value for the noise diode coupled temperature that was determined in section 4.4 (hot load backup mode). For details see chapter 6.



5 Key Interfaces

5.1 Algorithm Input

5.1.1 General Requirements for Input Data

In order to be able to perform the functional requirements (section 3.1), the GMI calibration algorithm needs input from a full orbit or at least a large enough parts of an orbit. The user can set the number of scans $n_{scans} > 500$ as input. The output for the first and last 50 - 200 scans will be either missing or degraded. The reason for this is that is:

1. the algorithm needs to calculate averages for hot and cold calibration counts (with and without noise diode injection) over multiple scans
2. flag the cold counts for lunar or RFI intrusion
3. interpolate over scans that were flagged for lunar intrusion

Therefore the user needs to ensure that there is sufficient overlap between successively processed orbits, if no data are to be lost. A convenient input format for the algorithm is the format of the TMI Level 1A and Level 1B files, which use one full orbit plus 50 scans from the prior orbit at the beginning and minus 50 scans from the following orbit at the end. This is necessary in order to:

In order to correct for moon or Earth intrusion into the cold sky view or solar intrusion into the hot load, the algorithm also needs certain input from the S/C and geolocation.

In the following section, we specify the input that is required for the algorithm. Hereby we will use the dimensional parameters that are listed in Table 6.

Table 6: Dimensional parameters.

n_{chan}	Number of GMI channels.
n_{freq}	Number of GMI frequencies (horns).
n_{scans}	Maximal number of scans in the input file. For missing scans, the entries should be the ones specified in section 5.4.
n_{cold}	Maximum number of cold calibration samples in each scan. It should be large enough to accommodate the channel with the most cold samples. For channels with less cold samples, the missing entries should be set to the <i>missing_count</i> value (section 5.4).
n_{hot}	Maximum number of hot calibration samples in each scan. It should be large enough to accommodate the channel with the most hot samples. For channels with less hot samples, the missing entries should be set to the <i>missing_count</i> value (section 5.4).
n_{Earth}	Maximum number of Earth view samples in each scan. It should be large enough to accommodate the channel with the most Earth samples. For channels with less samples, the missing entries should be set to the <i>missing_count</i> value (section 5.4).
n_{cells}	Maximum numbers of total samples in each scan. It should be large enough to accommodate the channel with the most Earth samples. For channels with less samples, the missing entries should be set to the <i>missing_count</i> value (section 5.4).
$n_{PRT,h}$	Number of thermistors that are embedded into the hot load (section 4.3).
$n_{PRT,MR}$	Number of thermistors at the main reflector (section 8.6).
$n_{PRT,rec}$	Number of thermistors at the receivers.

5.1.2 Geolocation Input

Table 7: Geolocation input for the calibration algorithm.

Quantity	Dimension	Unit	Description
time of scan	n_{scans}	sec (since 01JAN2000 00Z)	for each scan at start of Earth view can be interpolated from ephemeris records
moon location	3, n_{scans}	unit vector in GMI system (Appendix A.5)	for each scan this input needs to come from geolocation
sun location	3, n_{scans}	unit vector in GMI system (Appendix A.5)	for each scan this input needs to come from geolocation
Earth boresight location	2, n_{scans} , n_{cells}	deg	latitude + longitude for each sample this input needs to come from geolocation
intra-orbit position (orbital angle)	n_{scans}	deg	for each scan

Table 7 lists the necessary geolocation inputs for the pre-launch algorithm. The vectors pointing from the S/C to the moon and the sun, respectively, are unit vectors in the GMI system (Appendix A.5) and need to be determined during geolocation. The Earth boresight location is specified by latitude and longitude at each observation with and without noise diode injection.

5.1.3 On-Orbit Instrument Data

Table 8: On-orbit instrument input data for the calibration algorithm.

Quantity	Dimension	Unit	Description
noise diode indicator	n_{scans}		0 = noise diode off 1 = noise diode on
Earth view counts	n_{chan} , n_{scans} , n_{Earth}	counts	for each Earth observation for each channel
hot load PRT	n_{scans} , $n_{\text{PRT,h}}$	Kelvin	once for each scan
hot counts	n_{chan} , n_{scans} , n_{hot}	counts	for each hot observation for each channel for every 2 nd scan for channels 1 – 7 when noise diodes enabled for every scan for channels 1 – 7 when noise diodes disabled for every scan for channels 8 – 13
hot counts + noise diode	n_{chan} , n_{scans} , n_{hot}	counts	for each hot observation for each channel for every 2 nd scan for channels 1 – 7 when noise diodes enabled
cold counts	n_{chan} , n_{scans} , n_{cold}	counts	for each cold observation for each channel for every 2 nd scan for channels 1 – 7 when noise diodes enabled for every scan for channels 1 – 7 when noise diodes disabled for every scan for channels 8 – 13
cold counts + noise diode	n_{chan} , n_{scans} , n_{cold}	counts	for each cold observation for each channel for every 2 nd scan for channels 1 – 7 when noise diodes enabled
main reflector PRT	n_{scans} , $n_{\text{PRT,MR}}$	Kelvin	for each scan
cold sky reflector PRT	n_{scans}	Kelvin	for each scan
number of precipitation radar blanking pulses	2, n_{scans} , n_{cells}		BATC 37 V/H for each sample for each scan (Earth view, hot, cold)

Table 9: On-orbit instrument data for trending of noise-diode and non-linearity.

Quantity	Dimension	Unit	Description
receiver, mixer/preamp and LO-source PRTs	$n_{\text{scans}}, n_{\text{PRT,rec}}$	Kelvin	for each scan
noise diode physical temperature	$n_{\text{chan}}, n_{\text{scans}}$		for each scan for each channel that uses noise diode
receiver gain setting	n_{chan}		

Table 8 lists the instrument measurements that are inputs to the calibration algorithm. The noise diode is switched on and off every other scan. The noise diode indicator specifies if the calibration count (hot or cold) was taken with or without noise diode injection.

Table 9 lists the instrument data that are inputs to the on-orbit trending of non-linearity and noise diode coupled temperature.

5.1.4 External Input Data

Table 10 lists all necessary external input to the calibration algorithm and also the sources from which these inputs will be obtained.

Table 10: External input data to the calibration algorithm.

Quantity	Dimension	Unit	Source
cold mirror vector	3, n_{chan}	unit vector (GMI system)	BATC
static Earth average TB map	Earth grid $n_{\text{chan}}, 360, 180$	Kelvin	RSS simulated from RTM or post launch
Earth fraction of CSV	$n_{\text{chan}}, n_{\text{cold}}$		BATC RSS post launch analysis (12 months)
correction scheme for along scan biases in Earth sector	$n_{\text{chan}}, n_{\text{Earth}}$		TBD RSS from post-launch analysis (3 months)
correction scheme for intra-orbit biases in Earth sector	$n_{\text{chan}}, \text{TBD}$		TBD RSS from post-launch analysis (3 months)
correction scheme for along scan biases in CSV	$n_{\text{chan}}, n_{\text{cold}}$		BATC
correction scheme for along scan biases in hot load view	$n_{\text{chan}}, n_{\text{hot}}$		BATC
correction scheme for solar intrusion into hot load	$n_{\text{chan}}, \text{TBD}$		RSS post-launch
off-nadir angles	n_{chan}	deg	BATC
azimuth offset (off track angles) at beginning of Earth view	n_{chan}	deg	BATC
number of valid Earth view samples	n_{chan}		BATC
indices of valid Earth view samples	$n_{\text{chan}}, n_{\text{Earth}}$		RSS post launch
number of valid cold sky view samples	n_{chan}		BATC
indices of valid cold sky view samples	$n_{\text{chan}}, n_{\text{cold}}$		RSS post launch
number of valid hot load view samples	n_{chan}		BATC
indices of valid hot load view samples	$n_{\text{chan}}, n_{\text{hot}}$		RSS post launch
integration time	n_{chan}	msec	BATC
hot load PRT weights w_i and u_i , $i=0,1$	n_{chan}	see (6)	BATC thermal model
hot load thermistor bias b^{PRT}	$n_{\text{PRT,h}}$	Kelvin	BATC
indices of valid hot load PRT temps for each channel	$n_{\text{chan}}, n_{\text{hot}}$		BATC

APC coefficients			BATC antenna patterns RSS orbit simulator RSS update from post-launch analysis (3 months)
cross-pol correction coefficients for dual polarization frequencies (10, 18, 36, 89, 166 GHz)	10		
spillover correction coefficients	n_{chan}		
main reflector emissivity	n_{chan}		BATC
cold sky reflector emissivity	n_{chan}		BATC
ground or trended non-linearity parameter u (chapter 6)	n_{chan}	1/Kelvin	BATC
trended noise diode coupled temperature	n_{chan}	Kelvin	RSS post launch trending
duration of precipitation radar blanking pulse	2, n_{cells}	msec	BATC 37 V/H for each sample (Earth view, hot, cold)

5.2 Algorithm Output

Table 11 lists all the output data of the calibration algorithm.

Table 11: Output of the calibration algorithm.

Quantity	Dimension	Unit	Description
scan averaged cold counts	$n_{\text{chan}}, n_{\text{scans}}$	counts	once for each scan for each channel
scan averaged cold counts + noise diode	$n_{\text{chan}}, n_{\text{scans}}$	counts	once for each scan for each channel
scan averaged hot counts	$n_{\text{chan}}, n_{\text{scans}}$	counts	once for each scan for each channel
scan averaged hot counts + noise diode	$n_{\text{chan}}, n_{\text{scans}}$	counts	once for each scan for each channel
effective hot load temperature	$n_{\text{chan}}, n_{\text{scans}}$	Kelvin	once for each scan for each channel
effective cold sky temperature	$n_{\text{chan}}, n_{\text{scans}}$	Kelvin	once for each scan for each channel
flag for moon intrusion into cold sky view (combined with Q/C flag, section 5.5)	$n_{\text{chan}}, n_{\text{scans}}$		once for each scan for each channel
gain (unprimed, c.f. equation (17))	$n_{\text{chan}}, n_{\text{scans}}$	counts/Kelvin	once for each scan for each channel
offset (unprimed, c.f. equation (18))	$n_{\text{chan}}, n_{\text{scans}}$	counts	once for each scan for each channel
gain at reference tie point temperatures 3K and 300K (c.f. equation (24))	$n_{\text{chan}}, n_{\text{scans}}$	counts/Kelvin	once for each scan for each channel
offset at reference tie point temperatures 3K and 300K (c.f. equation (24))	$n_{\text{chan}}, n_{\text{scans}}$	counts	once for each scan for each channel
on-orbit non-linearity parameter u computed from 4-point calibration using noise diodes (for trending purposes) (c.f. equations (20) + (26))	$n_{\text{chan}}, n_{\text{scans}}$	1/Kelvin	once for each scan for each channel
noise diode coupled temperature computed from 4-point calibration using noise diodes (for trending purposes) (c.f. section 6.2.2)	$n_{\text{chan}}, n_{\text{scans}}$	Kelvin	once for each scan for each channel
antenna temperature	$n_{\text{chan}}, n_{\text{scans}}, n_{\text{Earth}}$	Kelvin	for each Earth observation for each channel
TOA brightness temperature	$n_{\text{chan}}, n_{\text{scans}}, n_{\text{Earth}}$	Kelvin	for each Earth observation for each channel
Q/C and exception flag	$n_{\text{chan}}, n_{\text{scans}}$		once for each scan

(combined with lunar flag, section 5.5)			for each channel
---	--	--	------------------

5.3 User Interface Design and Code Structure

The algorithm is delivered as standard FORTRAN90 code, which is divided into sub-modules as described in chapter 4. Each submodule corresponds to a separate FORTRAN90 module and contains:

1. A header with parameter definitions, type declarations and array declarations.
2. One or two master subroutine and possibly some other major routines that are called directly by the user during processing.
3. Some other subroutines that are only called internally but not designed to be called directly by the user.

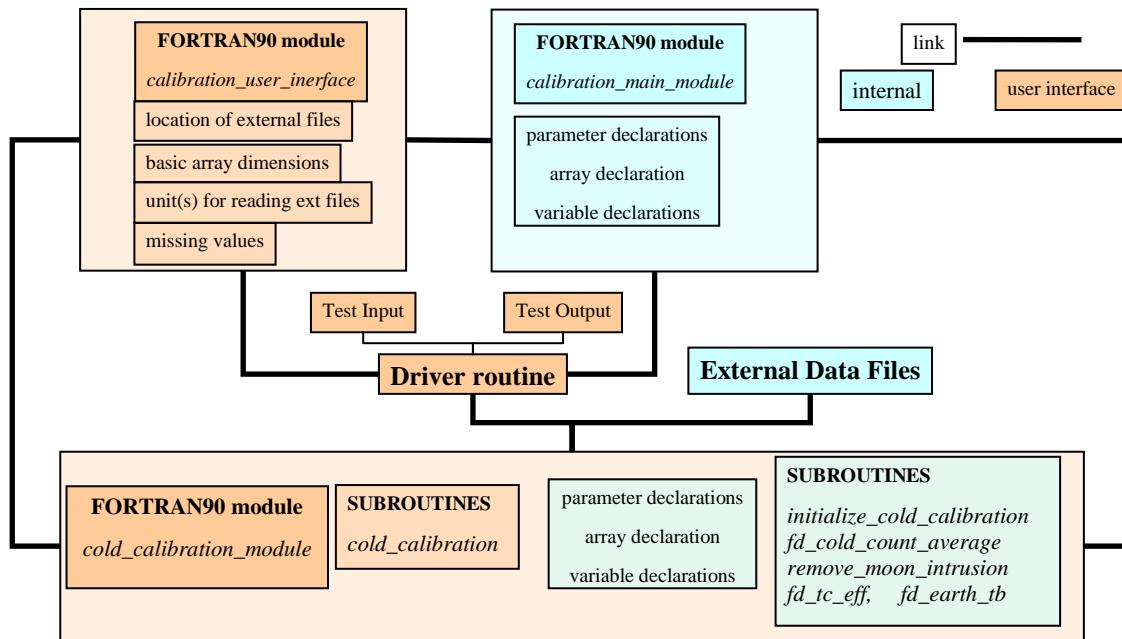


Figure 12: User interfacing diagram: Calling and linking for the cold calibration module as example.

The external input (Table 10) is supplied either through external files in ASCII format or through parameter statements which are located in the FORTRAN90 module *calibration_main_module*. This module is linked to all the other FORTRAN90 submodules and contains parameters and type or array declarations that are used by more than one of the submodules. However, the user will not directly interface with it.

The public FORTRAN90 module *calibration_user_interface* is designed for doing all interfacing with the user. It will contain:

1. The pathnames and locations for the external files (CHARACTER parameters).
2. Input units for reading all the external input (INTEGER (4) parameters).
3. Placeholder for missing values (section 5.4).
4. The basic dimensions from Table 6 (INTEGER (4) parameters).

Those values can be set and changed by the user as necessary. The module will link to all submodules and the user should link to this module in the calling routine. The submod-

ules whose master routine are to be called by the user's calling routine, need also to be linked to this routine.

All modules, parameters, variables and routines that are not directly interfacing with the user will be private. If and only if they are interfacing with the user they will be public.

Figure 12 shows the user interfacing with the cold calibration module example. The interfacing with the other submodules works analogous.

Further details are specified in the *Software User Manual for the GMI Calibration Algorithm*.

5.4 Format and Range for Submodule I/O

Table 12 - Table 20 specify the format and valid parameter range for the input and output to the master subroutines for each submodule. The submodules *cold_calibration*, *hot_calibration*, *calibration_par* (4pt and 2 pt) and *count_to_ta* are all called separately for each channel *ichan*. The submodule *ta_to_tb* is called separately for each frequency (horn) *ifreq*.

The cold counts with and without noise diode come combined into one array of dimension n_{scans} , n_{cold} . The noise diode is switched on and off for every other scan. The noise diode indicator is an array of dimension n_{scans} , whose value indicate if the measurement for this scan was taken with noise diode off (= 0) or on (= 1). The same applies to the hot count measurements with and without noise diode.

Table 12: I/O Format and valid range of variables for subroutine *cold_calibration* (cold calibration module).

Variable	Type	Array Dimension	Unit	Valid Range	I/O
channel index <i>ichan</i>	INTEGER(4)			[1, n_{chan}]	input
PRT reading of CSR	REAL(4)	n_{scans}	Kelvin	[T_{PRT0} , T_{PRT1}]	input
Earth boresight location (latitude, longitude)	REAL(4)	2, n_{scans} , n_{cold}	deg	[0,360[input
moon location (at center of cold scan)	REAL(4)	3, n_{scans}		[0,1]	input
noise diode indicator	INTEGER(2)	n_{scans}		0 or 1	input
cold counts	REAL(4)	n_{scans} , n_{cold}	counts	[CC_0 , CC_1], w/o ND [CN_0 , CN_1], w/i ND	input
scan averaged cold counts with or w/o noise diode	REAL(4)	n_{scans}	counts		output
effective cold sky temperature	REAL(4)	n_{scans}	Kelvin		output
scan flag	INTEGER(4)	n_{scans}			input/output

Table 13: I/O Format and valid range of variables for subroutine *hot_calibration* (hot calibration module).

Variable	Type	Array Dimension	Unit	Valid Range	I/O
channel index <i>ichan</i>	INTEGER(4)			[1, n_{chan}]	input
sun location	REAL(4)	3, n_{scans}		[0,1]	input
noise diode indicator	INTEGER(2)	n_{scans}		0 or 1	input
hot counts	REAL(4)	n_{scans} , n_{hot}	counts	[HH_0 , HH_1], w/o ND [HN_0 , HN_1], w/i ND	input
PRT weights	REAL(4)	$n_{PRT,h}$			input
hot load PRT reading	REAL(4)	n_{scans} , $n_{PRT,h}$	Kelvin	[T_{PRT0} , T_{PRT1}]	input

scan averaged hot counts with or w/o noise diode	REAL(4)	n_{scans}	counts		output
effective hot load temperature	REAL(4)	n_{scans}	Kelvin		output
scan flag	INTEGER(4)	n_{scans}			input/ output

Table 14: I/O Format and valid range of variables for subroutine *calibration_par_4pt* (calibration parameter module).

Variable	Type	Array Dimension	Unit	Valid Range	I/O
channel index ichan	INTEGER(4)			[1, 7]	input
scan averaged cold counts w/o noise diode	REAL(4)	n_{scans}	counts	[CC ₀ , CC ₁]	input
scan averaged cold counts with noise diode	REAL(4)	n_{scans}	counts	[CN ₀ , CN ₁]	input
scan averaged hot counts w/o noise diode	REAL(4)	n_{scans}	counts	[HH ₀ , HH ₁]	input
scan averaged hot counts with noise diode	REAL(4)	n_{scans}	counts	[HN ₀ , HN ₁]	input
effective cold sky temperature	REAL(4)	n_{scans}	Kelvin	[TC ₀ , TC ₁]	input
effective hot load temperature	REAL(4)	n_{scans}	Kelvin	[TH ₀ , TH ₁]	input
gain	REAL(4)	n_{scans}	counts/Kelvin		output
gain referenced to 3K and 300K	REAL(4)	n_{scans}	counts/Kelvin		output
offset counts	REAL(4)	n_{scans}	counts		output
offset referenced to 3K and 300K	REAL(4)	n_{scans}	counts		output
on-orbit non linearity	REAL(4)	n_{scans}	Kelvin		output
on-orbit non linearity parameter u	REAL(4)	n_{scans}	1/Kelvin		output
on-orbit noise diode coupled temperature	REAL(4)	n_{scans}	Kelvin		output
scan flag	INTEGER(4)	n_{scans}			input/ output

Table 15: I/O Format and valid range of variables for subroutine *calibration_par_2pt* (calibration parameter module).

Variable	Type	Array Dimension	Unit	Valid Range	I/O
channel index ichan	INTEGER(4)			[1, 7]	input
scan averaged cold counts w/o noise diode	REAL(4)	n_{scans}	counts	[CC ₀ , CC ₁]	input
scan averaged hot counts w/o noise diode	REAL(4)	n_{scans}	counts	[HH ₀ , HH ₁]	input
effective cold sky temperature	REAL(4)	n_{scans}	Kelvin	[TC ₀ , TC ₁]	input
effective hot load temperature	REAL(4)	n_{scans}	Kelvin	[TH ₀ , TH ₁]	input
gain	REAL(4)	n_{scans}	counts/Kelvin		output
offset counts	REAL(4)	n_{scans}	counts		output
scan flag	INTEGER(4)	n_{scans}			input/ output

Table 16: I/O Format and valid range of variables for subroutine *calibration_cons* (calibration parameter module).

Variable	Type	Array Dimension	Unit	Valid Range	I/O
channel index ichan	INTEGER(4)			[1, n _{chan}]	input
scan averaged cold counts w/o noise diode	REAL(4)	n _{scans}	counts	[CC ₀ , CC ₁]	input
scan averaged cold counts with noise diode	REAL(4)	n _{scans}	counts	[CN ₀ , CN ₁]	input
scan averaged hot counts w/o noise diode	REAL(4)	n _{scans}	counts	[HH ₀ , HH ₁]	input
scan averaged hot counts with noise diode	REAL(4)	n _{scans}	counts	[HN ₀ , HN ₁]	input
effective cold sky temperature	REAL(4)	n _{scans}	Kelvin	[TC ₀ , TC ₁]	input
effective hot load temperature	REAL(4)	n _{scans}	Kelvin	[TH ₀ , TH ₁]	input
non linearity parameter u	REAL(4)	n _{scans}	1/Kelvin		input
noise diode coupled temperature	REAL(4)	n _{scans}	Kelvin		input
gain calculated at 3 calibration points: g _{ref} = (g ₁ , g ₂ , g ₃) referenced to 3K and 300K (c.f. section 6.2.3)	REAL(4)	3, n _{scans}	counts/Kelvin		output
offset calculated at 3 calibration points: Ω _{ref} = (Ω ₁ , Ω ₂ , Ω ₃) referenced to 3K and 300K (c.f. section 6.2.3)	REAL(4)	3, n _{scans}	counts		output
scan flag	INTEGER(4)	n _{scans}			input/ output

Table 17: Format and valid range of variables for subroutine *count_to_ta_1* Earth TA module in normal mode, option 1: using cold and hot counts w/o noise diode as input.

Variable	Type	Array Dimension	Unit	Valid Range	I/O
channel index ichan	INTEGER(4)			[1, n _{chan}]	input
scan averaged cold counts without noise diode	REAL(4)	n _{scans}	counts	[CC ₀ , CC ₁]	input
effective cold sky temperature	REAL(4)	n _{scans}	Kelvin	[TC ₀ , TC ₁]	input
scan averaged hot counts without noise diode	REAL(4)	n _{scans}	counts	[HC ₀ , HC ₁]	input
effective hot load temperature	REAL(4)	n _{scans}	Kelvin	[TH ₀ , TH ₁]	input
non-linearity parameter u (ground or on-orbit trended)	REAL(4)		1/Kelvin	[TNL ₀ , TNL ₁]	input
Earth view counts	REAL(4)	n _{scans} , n _{Earth}	counts	[EC ₀ , EC ₁]	input
antenna temperature	REAL(4)	n _{scans} , n _{Earth}	Kelvin		output
scan flag	INTEGER(4)	n _{scans}			input/ output

Table 18: Format and valid range of variables for subroutine *count_to_ta_2* Earth TA module in normal mode, option 2: using gain and offset at reference temperatures (3K and 300 K) as input.

Variable	Type	Array Dimension	Unit	Valid Range	I/O
channel index ichan	INTEGER(4)			[1, n _{chan}]	input

gain referenced to 3K and 300K	REAL(4)		counts/Kelvin	TBD	input
offset referenced to 3K and 300K	REAL(4)		counts	TBD	input
non-linearity parameter u (ground or on-orbit trended)	REAL(4)		1/Kelvin	[TNL ₀ , TNL ₁]	input
Earth view counts	REAL(4)	n_{scans} , n_{Earth}	counts	[EC ₀ , EC ₁]	input
antenna temperature	REAL(4)	n_{scans} , n_{Earth}	Kelvin		output
scan flag	INTEGER(4)	n_{scans}			input/ output

**Table 19: Format and valid range of variables for subroutine *count_to_ta_bkp*
Earth TA module in hot-load backup mode: use cold counts with and w/o noise diode as input.**

Variable	Type	Array Dimension	Unit	Valid Range	I/O
channel index ichan	INTEGER(4)			[1, 7]	input
scan averaged cold counts without noise diode	REAL(4)	n_{scans}	counts	[CC ₀ , CC ₁]	input
scan averaged cold counts with noise diode	REAL(4)	n_{scans}	counts	[CN ₀ , CN ₁]	input
noise diode coupled temperature (ground or on-orbit trended)	REAL(4)	n_{scans}	Kelvin	[TND ₀ , TND ₁]	input
non-linearity parameter u (ground or on-orbit trended)	REAL(4)	n_{scans}	1/Kelvin	[TNL ₀ , TNL ₁]	input
Earth view counts	REAL(4)	n_{scans} , n_{Earth}	counts	[EC ₀ , EC ₁]	input
antenna temperature	REAL(4)	n_{scans} , n_{Earth}	Kelvin		output
scan flag	INTEGER(4)	n_{scans}			input/ output

Table 20: Format and valid range of variables for subroutine *ta_to_tb* (APC module).

Variable	Type	Array Dimension	Unit	Valid Range	I/O
frequency index ifreq	INTEGER(4)			[1, n_{freq}]	input
antenna temperature (1=v-pol, 2=h-pol)	REAL(4)	n_{scans} , n_{Earth} , 2	Kelvin	[TA ₀ , TA ₁]	input
main reflector PRT	REAL(4)	n_{scans} , $n_{PRT,MR}$	Kelvin	[T _{PRT0} , T _{PRT1}]	input
intra orbit position (fractional rev #, orbital angle)	TBD	n_{scans}	TBD	TBD	input
TOA brightness temperature (1=v-pol, 2=h-pol)	REAL(4)	n_{scans} , n_{Earth} , 2	Kelvin		output
scan flag	INTEGER(4)	n_{scans}			input/ output

5.5 Missing Observations and Exception Flag

The algorithm will check each input to the master subroutines if it lies on the valid range specified in Table 12 - Table 20. If this is not the case the entry will be regarded as missing input value. All missing input values should be set to the specific placeholder values which are listed in.

Table 21. If necessary, the user can change those values in the parameter statement of the *calibration_user_interface* module. Those values are also used by the algorithm for output missing values.

Table 21: Placeholders for missing input and output in the master subroutines.

Parameter	Type	suggested value	used for
<i>missing_count</i>	REAL(4)	-1.0	cold and hot counts without and with noise diode Earth counts
<i>missing_temp</i>	REAL(4)	-9999.0	hot load, MR. CSR effective hot load and cold sky temperatures non linearity noise diode coupled temperature antenna temperature TOA brightness temperatures
<i>missing_loc</i>	REAL(4)	-9999.0	Sun or moon vector Earth location (lat/lon of TA map)
<i>missing_pulse</i>	REAL(4)	-1.0	number/duration of blanking pulses

The action of the calibration algorithm if a missing input is encountered depends on the severity of the case.

The calibration algorithm produces a flag once at every scan that indicates if there are problems due to missing or invalid input, or if the quality of the output is degraded because certain corrections cannot be performed (e.g. lunar intrusion into the cold mirror). The flag in a 32 bit (INTEGER(4)) variable and is separately produced for each GMI channel. It is an array with the dimensions n_{scans} . It can be passed on between the master subroutines of different submodules, if they are called successively. If a specific Q/C or exception is met then the algorithm sets a specific bit position of the flag. Table 22 lists the bit positions of the scan flag and also specifies if the algorithm output is regular or missing.

Table 22: Exception handling and Q/C flag.

Set bit position of Q/C flag	Exception or degrading condition	Subroutine	Action
0	Sparse.		
1	Scan averaged cold counts without (with) noise diode are larger than or equal to scan averaged hot counts without (with) noise diode (ND). Scan averaged cold counts without noise diode are larger than or equal to scan averaged cold counts with ND. Scan averaged hot counts without noise diode are larger than or equal to scan averaged hot counts with ND.	calibration_par_4pt calibration_par_2pt calibration_cons count_to_ta count_to_ta_bkp	Invalid output. Set Q/C flag bit 6.
	Invalid cold count w/o ND. Invalid cold count with ND.	cold_calibration prbc_cold	Not used in scan average of cold counts. Missing output.
	Invalid hot count w/o ND. Invalid hot count with ND.	hot_calibration prbc_hot	Not used in scan average of hot counts. Missing output.
2	Insufficient number of valid cold counts w/o ND when computing scan average	cold_calibration calibration_par_4pt calibration_par_2pt calibration_cons	Missing output for scan average cold counts with ND. Missing output. Set Q/C flag bit 6. Missing $g_1, \omega_1, g_2, \omega_2$.

		count_to_ta	Missing output.
		count_to_ta_bkp	Missing output.
3	Insufficient number of valid hot counts w/o ND when computing scan average	hot_calibration	Missing output for scan average hot counts with ND.
		calibration_par_4pt	Missing output.
		calibration_par_2pt	Set Q/C flag bit 6.
		calibration_cons	Missing $g_1, \omega_1, g_3, \omega_3$.
		count_to_ta	Missing output.
		count_to_ta_bkp	Normal.
4	Insufficient number of valid cold counts with ND when computing scan average	cold_calibration	Missing output for scan average cold counts with ND.
		calibration_par_4pt	Missing output. Set Q/C flag bit 6.
		calibration_cons	Missing g_2, ω_2 .
		count_to_ta	Normal.
		count_to_ta_bkp	Missing output.
5	Insufficient number of valid hot counts with ND when computing scan average	hot_calibration	Missing output for scan average hot counts w/o ND.
		calibration_par_4pt	Missing output. Set Q/C flag bit 6.
		calibration_cons	Missing g_3, ω_3 .
		count_to_ta	Normal.
		count_to_ta_bkp	Normal.
6	Invalid or missing gain or offset.	count_to_ta	Missing output.
		count_to_ta_bkp	
		prbc_earth	Missing output. Set Q/C flag 19.
7	Invalid or missing trended/ pre-launch non-linearity.	calibration_cons	Missing output.
		count_to_ta	
		count_to_ta_bkp	
8	Invalid or missing trended/ pre-launch ND coupled temperature.	calibration_cons	Missing $g_2, \omega_2, g_3, \omega_3$.
		count_to_ta	Normal.
		count_to_ta_bkp	Missing output.
		prbc_earth	Missing output. Set Q/C flag bit 19.
9	Invalid or missing hot load PRT.	hot_calibration	Missing T_h^{eff} . Set Q/C flag bit 18.
10	Lunar intrusion into cold sky view. Correction was performed	cold_calibration	Normal.
11	Lunar intrusion into cold sky view. No correction could be performed.	cold_calibration	Normal.
12	Correction to hot load effective temperature due to sun intrusion into the hot load was performed.	hot_calibration	Normal.
13	Invalid or missing moon vector.	cold_calibration	No check or correction for lunar intrusion into the cold sky view.
14	Invalid or missing earth location.	cold_calibration	No correction for earth view intrusion onto the cold sky

			view.	
15	Invalid or missing sun vector.	hot_calibration	No correction for sun intrusion into hot load.	
16	Invalid or missing CSR PRT.	cold_calibration	No correction for CSR emissivity.	
17	Invalid or missing MR PRT.	ta_to_tb	No correction for MR emissivity.	
18	Invalid or missing T_c^{eff} .	calibration_par_4pt	Graceful stop.	
		calibration_par_2pt		
		calibration_cons		
		count_to_ta		
			count_to_ta_bkp	
			prbc_cold	Missing output. Set Q/C bit flag 19.
	Invalid or missing T_h^{eff} .	calibration_par_4pt	Missing output.	
		calibration_par_2pt	Set Q/C flag bit 6.	
		calibration_cons	Missing $g_1, \omega_1, g_3, \omega_3$.	
		count_to_ta	Missing output.	
count_to_ta_bkp		Normal.		
		prbc_hot	Missing output. Set Q/C bit flag 19.	
19	Invalid or missing PRB duration	prbc_cold prbc_hot prbc_earth	Missing output.	
	Invalid or missing PRB number.	prbc_cold prbc_hot prbc_earth	Missing output.	
20	Invalid or missing receiver physical temperature	prbc_cold prbc_hot prbc_earth	Missing output. Set Q/C flag bit 19.	
		fd_u_tnd	Missing output. Set Q/C flag bits 7 and 8.	
	Invalid or missing Earth count	count_to_ta	Missing output.	
		count_to_ta_bkp	Missing output.	
		prbc_earth	Missing output.	
	Invalid or missing TA for v-pol.	ta_to_tb	Missing output	
	Invalid or missing TA for h-pol.	ta_to_tb	Missing output for dual polarization bands. Normal for single polarization bands.	
21 - 31	Sparse.			

5.6 Other Errors and Exceptions

The cases discussed in section 5.5 covers all errors and exceptions that occur for any of the inputs from the user interface of section 5.4 during normal operation of the algorithm. In addition, also external input is fed to the algorithm, either by parameter statements or

by reading from external files. All the external files that the algorithm reads are of checked for correctness. However, there is the possibility that some of these external input files might be corrupted. The algorithm code will therefore perform soundness checks on each variable that is read in from an external file and if that check fails it will gracefully stop with an error message explaining the details.

The algorithm will also check the validity of the argument of certain mathematical operations and gracefully stop if the argument is invalid. Typical examples are:

1. Dividing by 0.
2. Taking the square root of negative argument.
3. Taking the *log* of a zero or negative argument.
4. Taking the *arc sin* or *arc cos* of an argument whose absolute value is larger than 1.

6 Radiometric Calibration

This chapter will cover the theoretical background for the submodules of sections 4.4 and 4.5. We will develop the general formalism for the radiometric calibration and the transformation from Earth counts into antenna temperatures.

6.1 Baseline Radiometric Calibration

6.1.1 Radiometric Transfer Function

GMI has similarity to other radiometers in that it measures radiation from two calibration loads, a cold sky view and a black body (hot load). GMI is distinct in that it also provides two additional measurements, a cold sky view with noise diode and hot load view with noise diode. Operational GMI has a calibration cycle that repeats every other rotation. On the first rotation, the cold sky view and the hot load are sampled and on the second rotation the cold sky view plus noise diode and hot load plus noise diode is sampled. This provides 4 calibration points, enough information to allow the excess noise temperature of the noise diodes and the nonlinearity of the receivers to be determined in addition to the gain and offset of the receivers.

The purpose of the calibration measurements is to accurately determine the radiometric transfer function, which relates the measured scene counts C_{scene} to the antenna temperature $T_{A,scene}$:

$$T_{A,scene} = F(C_{scene}) \quad (7)$$

The scene count C_{scene} can be either:

1. The Earth view count C_E
2. The scan averaged hot count without noise diode \bar{C}_h
3. The scan averaged hot count with noise diode \bar{C}_{hn}
4. The scan averaged cold count without noise diode \bar{C}_c
5. The scan averaged cold count with noise diode \bar{C}_{cn}

If the transfer function (7) was perfectly linear, two calibration points would uniquely determine its form at the time of the calibration measurements. While the goal is to provide receivers that are linear, in reality they are slightly nonlinear. To account for the nonlinearity, a quadratic radiometric transfer function will be used. The quadratic term will be computed from pre-launch data and receiver temperature. The assumption that the nonlinearity does not change from pre-launch form does not need to be made for GMI as with other radiometers. The nonlinearity is determined on-orbit by the four-point calibration method and provides confirmation of the nonlinearity over time. If nonlinearity drifts a statistically significant amount, the data can be updated on-orbit. The general form of a quadratic radiometric transfer function can be written as:

$$T_{A,scene} = x \cdot T_h^{eff} + (1-x) \cdot T_c^{eff} - 4T_{nl} \cdot x \cdot (1-x) \quad (8)$$

x is the normalized radiometer response

$$x = \frac{C_{scene} - \bar{C}_c}{\bar{C}_h - \bar{C}_c} \quad (9)$$

T_h^{eff} is the effective hot load temperature and T_c^{eff} the effective cold space temperature including the deviation from the RJ law (Appendix D) and Earth intrusion into the cold sky view and T_{nl} is the peak non-linearity.

We write out (8) and (9) for three relevant cases:

1. Earth counts

$$T_{A,E} = x_E T_h^{eff} + (1 - x_E) T_c^{eff} - 4T_{nl} x_E (1 - x_E) \quad x_E = \frac{C_E - \bar{C}_c}{\bar{C}_h - \bar{C}_c} \quad (10)$$

2. Cold counts+ noise diode

$$T_{cn} = T_c^{eff} + T_n = x_{cn} T_h^{eff} + (1 - x_{cn}) T_c^{eff} - 4T_{nl} x_{cn} (1 - x_{cn}) \quad x_{cn} = \frac{\bar{C}_{cn} - \bar{C}_c}{\bar{C}_h - \bar{C}_c} \quad (11)$$

3. Hot counts + noise diode

$$T_{hm} = T_h^{eff} + T_n = x_{hm} T_h^{eff} + (1 - x_{hm}) T_c^{eff} - 4T_{nl} x_{hm} (1 - x_{hm}) \quad x_{hm} = \frac{\bar{C}_{hm} - \bar{C}_c}{\bar{C}_h - \bar{C}_c} \quad (12)$$

T_n is the noise diode coupled (excess) temperature.

If, conversely, the scene temperature is given, then one can obtain the radiometer counts from inverting equations (8) and (9):

$$C_{scene} = \bar{C}_c + (\bar{C}_h - \bar{C}_c) \cdot \begin{cases} \frac{1}{2\alpha} (\sqrt{\beta^2 - 4\alpha\gamma} - \beta), & \text{if } T_{nl} \neq 0 \\ \frac{T_{A,scene} - T_c^{eff}}{T_h^{eff} - T_c^{eff}}, & \text{if } T_{nl} = 0 \end{cases} \quad (13)$$

$$\alpha = +4T_{nl} \quad \beta = T_h^{eff} - T_c^{eff} - 4T_{nl} \quad \gamma = T_c^{eff} - T_{A,scene}$$

In order to exhibit the dependence of $T_{A,scene}$ on C_{scene} directly, we rewrite equation (8) using equation (9). The terms are:

$$x = \frac{C_{scene} - \bar{C}_c}{\bar{C}_h - \bar{C}_c} \quad 1 - x = \frac{\bar{C}_h - C_{scene}}{\bar{C}_h - \bar{C}_c}$$

$$x \cdot (1 - x) = -\frac{C_{scene}^2}{(\bar{C}_h - \bar{C}_c)^2} + \frac{C_{scene} \cdot (\bar{C}_h + \bar{C}_c)}{(\bar{C}_h - \bar{C}_c)^2} - \frac{\bar{C}_h \cdot \bar{C}_c}{(\bar{C}_h - \bar{C}_c)^2} \quad (14)$$

$$x T_h^{eff} + (1 - x) T_c^{eff} = T_c^{eff} + x \cdot (T_h^{eff} - T_c^{eff}) = C_{scene} \cdot \frac{T_h^{eff} - T_c^{eff}}{\bar{C}_h - \bar{C}_c} + \left[T_c^{eff} - \bar{C}_c \cdot \frac{T_h^{eff} - T_c^{eff}}{\bar{C}_h - \bar{C}_c} \right]$$

which gives:

$$T_{A,scene} = 4 \cdot T_{nl}' \cdot C_{scene}^2 + \frac{1}{g'} C_{scene} + \omega' \quad (15)$$

The parameters T'_{nl} , g' and ω' in (15) are defined as

$$T'_{nl} = \frac{T_{nl}}{(\bar{C}_h - \bar{C}_c)^2} \quad (16)$$

$$\frac{1}{g'} = \frac{1}{g} - 4 \cdot T'_{nl} \cdot (\bar{C}_h + \bar{C}_c) \quad g = \frac{\bar{C}_h - \bar{C}_c}{T_h^{eff} - T_c^{eff}} \quad (17)$$

$$\omega' = \omega + 4 \cdot T'_{nl} \cdot \bar{C}_h \cdot \bar{C}_c \quad \omega = T_c^{eff} - \frac{1}{g} \cdot \bar{C}_c = \frac{(-\Omega)}{g} \quad \Omega = \bar{C}_c - g \cdot T_c^{eff} \quad (18)$$

g , ω , Ω are the conventional gain, offset temperature and offset count parameters, respectively, which are used in a linear two-point calibration. If the radiometric transfer function (7) is strictly quadratic, then the primed parameters T'_{nl} , g' and ω' in (15) do not depend on the tie points T_h^{eff} and T_c^{eff} that were chosen for the calibration. However, the conventional (unprimed) parameters T_{nl} , g , ω and Ω do depend on the tie points T_h^{eff} and T_c^{eff} .

Equation (15) can be rewritten as:

$$T_{A,scene} = 4T'_{nl} \cdot (C_{scene} - \bar{C}_h) \cdot (C_{scene} - \bar{C}_c) + \frac{C_{scene} - \bar{C}_c}{g} + T_c^{eff} \quad (19)$$

Though the non-linearity parameter T'_{nl} does not depend on the tie points T_h^{eff} and T_c^{eff} , it does depend on the gain g . If T_h^{eff} , T_c^{eff} and $T_{A,scene}$ in (19) are fixed and the non-linearity is small, then the product $(C_{scene} - \bar{C}_h) \cdot (C_{scene} - \bar{C}_c)$ scales like g^2 under a change of the gain g . That means that the non-linearity parameter u which is defined as

$$u \equiv 4 \cdot T'_{nl} \cdot g^2 = \frac{4 \cdot T_{nl}}{(T_h^{eff} - T_c^{eff})^2} \quad (20)$$

is independent of the tie points T_h^{eff} and T_c^{eff} and also independent on the gain g , if the non-linearity itself is small. The deviation from a constant value is of 2nd order in the non-linearity. It could depend on the physical temperature of the receiver. The parameter u has been used in the recalibration of the MSU [1] and will be used by BATC in the ground calibration (BATC 2298950). Rewriting equations (15), (17), (18) and (19) with u instead of T'_{nl} gives:

$$\begin{aligned} T_{A,scene} &= \frac{u}{g^2} \cdot C_{scene}^2 + \frac{1}{g'} C_{scene} + \omega' \\ &= \frac{u}{g^2} \cdot (C_{scene} - \bar{C}_h) \cdot (C_{scene} - \bar{C}_c) + \frac{C_{scene} - \bar{C}_c}{g} + T_c^{eff} \\ &= \frac{u}{g^2} \cdot (C_{scene} - \bar{C}_h) \cdot (C_{scene} - \bar{C}_c) + \frac{C_{scene} - \Omega}{g} \end{aligned} \quad (21)$$

with

$$\frac{1}{g'} = \frac{1}{g} - \frac{u}{g^2} \cdot (\bar{C}_h + \bar{C}_c) \quad g = \frac{\bar{C}_h - \bar{C}_c}{T_h^{eff} - T_c^{eff}} \quad (22)$$

and

$$\omega' = \omega + \frac{u}{g^2} \cdot \bar{C}_h \cdot \bar{C}_c \quad \omega = T_c^{eff} - \frac{1}{g} \cdot \bar{C}_c \quad \Omega = \bar{C}_c - g \cdot T_c^{eff} \quad (23)$$

6.1.2 Gain and Offset at Reference Tie Point Temperature 3K and 300K

As explained above, gain and offset are both dependent on the hot and cold temperature tie points, T_h and T_c : $g = g(T_c, T_h)$ and $\Omega = \Omega(T_c, T_h)$, if $u \neq 0$. For the purpose of on-orbit trending (section 6.2.4) we will use a gain and offset that is defined at the fixed reference temperatures $T_c^{ref} = 3K$ and $T_h^{ref} = 300K$, respectively. Section 6.1.1 shows how to calculate $g(T_c^{eff}, T_h^{eff})$ and $\Omega(T_c^{eff}, T_h^{eff})$ from the measured radiometer counts. The transformation into $g(T_c^{ref}, T_h^{ref})$ and $\omega(T_c^{ref}, T_h^{ref})$ can be done as follows:

1. Using (13) we can calculate the values of the hot counts at the reference hot temperature $C_h^{ref} = C_h(T_{A,scene} = T_h^{ref})$ and the values of the cold counts at the reference cold temperature $C_c^{ref} = C_c(T_{A,scene} = T_c^{ref})$, respectively.
2. The values for $g(T_c^{ref}, T_h^{ref})$ and $\Omega(T_c^{ref}, T_h^{ref})$ follow from (22) and (23), respectively:

$$g(T_c^{ref}, T_h^{ref}) = \frac{\bar{C}_h^{ref} - \bar{C}_c^{ref}}{T_h^{ref} - T_c^{ref}} \quad (24)$$

$$\Omega(T_c^{ref}, T_h^{ref}) = \bar{C}_c^{ref} - g(T_c^{ref}, T_h^{ref}) \cdot T_c^{ref}$$

6.1.3 Determination of Ground Non-Linearity

BATC will provide set of curves of radiometer counts as function of scene temperature (Table 5). The non-linearity parameter u can be determined by performing a quadratic fit of the temperature to the counts of the form (21).

6.2 On-Orbit Retrieval of Calibration Parameters and Trending

6.2.1 Determination and Trending of Non-Linearity

From the 4 calibration measurements \bar{C}_c , \bar{C}_h , \bar{C}_{cn} and \bar{C}_{hn} one can uniquely determine the values for T_{nl} and T_n assuming that the tie points T_c^{eff} and T_h^{eff} are known. Combining (11) and (12) we find:

$$(T_h^{eff} - T_c^{eff}) = (x_{hn} - x_{cn})T_h^{eff} - (x_{hn} - x_{cn})T_c^{eff} - 4T_{nl} [x_{hn}(1 - x_{hn}) - x_{cn}(1 - x_{cn})] \quad (25)$$

$$(T_h^{eff} - T_c^{eff}) = (x_{hn} - x_{cn}) \cdot (T_h^{eff} - T_c^{eff}) - 4T_{nl} [x_{hn}(1 - x_{hn}) - x_{cn}(1 - x_{cn})]$$

and

$$T_{nl} = \frac{1}{4} (T_h^{eff} - T_c^{eff}) \frac{(x_{hn} - x_{cn} - 1)}{[x_{hn}(1 - x_{hn}) - x_{cn}(1 - x_{cn})]} \quad (26)$$

The non-linearity u , which depends neither on the tie points T_c^{eff} and T_h^{eff} nor on the gain g , can be immediately calculated from (26) and (20). The on-orbit trending of u as function of the physical temperature of the receiver T_{rcv}^{phys} will consist of retrieving u over many orbits and compute the average values and standard deviations of u within sufficiently populated bins of T_{rcv}^{phys} . If the non-linearity is stable, we expect to find that u does not vary with T_{rcv} and that its value is consistent with the ground measurement (section 6.1.2). The on-orbit trended value for u can replace the ground measurement if we find significant drifts. The criteria are TBD post-launch. If the value of the non-linearity is small, it is always possible to reside to the standard 2-point calibration using only hot load and cold sky measurements and setting $u = 0$ in (21) or $T_{nl} = 0$ in (8).

6.2.2 Determination and Trending of Noise-Diode Coupled Temperature

Once we have computed T_{nl} from equation (26), we can calculate the noise diode coupled temperature T_n from either equation (11) or equation (12). We will trend T_n as function of the physical noise diode temperature T_n^{phys} by retrieving T_n over many orbits and compute the average values and standard deviations of T_n within sufficiently populated bins of T_n^{phys} . We compare the trended curves with those of pre-flight measurements to check noise diode performance. If this check fulfills criteria TBD post-launch then the noise diode measurements can be used in the hot-load backup radiometric calibration (section 6.3). The trended relation $T_n = T_n(T_n^{phys})$ can be put in form of a look-up table or a simple analytical relation between T_n and T_n^{phys} can be derived, which serves to compute T_n on-orbit from the thermistor measurement for T_n^{phys} .

6.2.3 Calibration Point Consistency Check

The gain $g(T_c^{ref}, T_h^{ref})$ and offset $\Omega(T_c^{ref}, T_h^{ref})$ at the reference tie point temperatures 3K and 300K are calculated according to section 6.1.2 in 3 different ways:

1. Using cold load + hot load measurements: These values are called $g_1(T_c^{ref}, T_h^{ref})$ and $\Omega_1(T_c^{ref}, T_h^{ref})$, respectively. To calculate them we use the values from the cold and hot calibration scans in equation (13).

2. Using cold load and cold load + ND: These values are called $g_2(T_c^{ref}, T_h^{ref})$ and $\Omega_2(T_c^{ref}, T_h^{ref})$, respectively. To calculate them we substitute in equation (13):

$$T_h^{eff} \rightarrow T_c^{eff} + T_n \quad \bar{C}_h \rightarrow \bar{C}_{cn} \quad (27)$$

3. Using cold load and cold load + ND: These values are called $g_3(T_c^{ref}, T_h^{ref})$ and $\Omega_3(T_c^{ref}, T_h^{ref})$, respectively. To calculate them we substitute in equation (13):

$$\begin{aligned} T_c^{eff} &\rightarrow T_h^{eff} & \bar{C}_c &\rightarrow \bar{C}_h \\ T_h^{eff} &\rightarrow T_h^{eff} + T_n & \bar{C}_h &\rightarrow \bar{C}_{hh} \end{aligned} \quad (28)$$

T_n is the trended noise diode coupled temperature. We will compare the 3 values $g_i, i=1,2,3$ and $\Omega_i, i=1,2,3$. If the three values do not agree within a certain error, whose value is TBD post-launch, it means that there are problems with the calibration system that would need to be further investigated. Those problems could for example result from:

1. Hot load anomaly: Sun intrusion into the hot load causing gradients within the hot load which leads to an erroneous effective hot load temperature computation from (4). This will be discussed in more detail in section 11.5.
2. Contamination of the cold sky view (chapter 11) that were not properly corrected.
3. Problems with the noise diodes.
4. The assumption of a quadratic form (15) is not valid.
5. The value of the non-linearity u is incorrect.

A similar consistency check can be performed for the modified offset ω' from (15) and (18).

6.2.4 Trending of Gain and Offset

The gain $g(T_c^{ref}, T_h^{ref})$ and offset $\Omega(T_c^{ref}, T_h^{ref})$ at the reference tie point temperatures 3K and 300K (see section 6.1.2) will be trended as function of the physical receiver temperature T_{rcv}^{phys} . We retrieve $g(T_c^{ref}, T_h^{ref})$ and $\Omega(T_c^{ref}, T_h^{ref})$ over many orbits and compute average and standard deviation within sufficiently populated bins of T_{rcv}^{phys} . We will compare the curves $g(T_c^{ref}, T_h^{ref}; T_{rec}^{phys})$ and $\Omega(T_c^{ref}, T_h^{ref}; T_{rec}^{phys})$ to the ones that were measured in thermal-vacuum testing.

6.3 Hot-Load Backup Radiometric Calibration

The hot-load backup calibration uses the cold load and cold load + noise diode measurement together with either the ground-measured or trended noise diode coupled temperature T_n and the non-linearity parameter u . The radiometric transfer equations (8) and (9) take the form:

$$\begin{aligned}
 T_{A,Earth} &= x \cdot (T_c^{eff} + T_n) + (1-x) \cdot T_c^{eff} - 4T_{nl} \cdot x \cdot (1-x) \\
 x &= \frac{C_{Earth} - \bar{C}_c}{\bar{C}_{cn} - \bar{C}_c} \\
 T_{nl} &= \frac{1}{4} \cdot u \cdot T_n^2
 \end{aligned} \tag{29}$$

If we find a significant hot load anomaly due to sun intrusion into the hot load and if the noise diode coupled temperature is found to be sufficiently stable, the hot load backup calculation (29) of $T_{A,scene}$ will be used instead of the conventional calculation (8).

6.4 Precipitation Radar Blanking Correction

The GMI Instrument will incorporate a blanking technique to mitigate electromagnetic interference from the Ka-band precipitation radar. The blanking will pause the integration of channels 6-7 (36.64 GHz V/H) during the pulsing of the radar. Since the radar is

asynchronous with the GMI, the blanking will cause the effective integration period of channels 6-7 to vary by up to one blanking pulse for each measurement. The blanking will be enabled/ disabled by ground command. The duration of the blanking pulse τ_{pulse} will be a settable parameter determined on-orbit, which can range between 8 and 32 microseconds. The number of blanking pulses n_{pulse} received by the GMI receiver subsystem during each sample period will be available as part of the GMI science data record, and will be between 14 and 17 per 3.6 millisecond sample period.

The purpose of the precipitation radar blanking correction (PRBC) algorithm is to transform cold calibration counts $C_c(n_{pulse})$, hot calibration counts $C_h(n_{pulse})$ and Earth view counts $C_{Earth}(n_{pulse})$ to a reference value of n_{pulse}^{ref} , which we choose to be $n_{pulse}^{ref} = 16.0$.

BATC provided a characterization of the blanking by tabulating the radiometer gain and offset as function of the receiver physical temperature T_{rec}^{phys} and the duration of the blanking pulse τ_{pulse} assuming a fixed value of $n_{pulse} = 16.0$. This characterization can be transformed using the effective integration time, which is given as:

$$\tau_{int}^{eff} = \tau_{int} - n_{pulse} \cdot \tau_{pulse} \quad (30)$$

The τ_{int} is the standard integration time of 3.6 msec.

For a given value of T_{rec}^{phys} the gain g increases approximately linearly and the offset Ω decreases approximately linearly with increasing effective integration time τ_{int}^{eff} . The slope of the linear fits itself changes with the value of T_{rec}^{phys} . For the PRBC algorithm we assume a strictly linear model:

$$g(T_{rec}^{phys}; \tau_{int}^{eff}) = g_0(T_{rec}^{phys}) + \frac{\partial g}{\partial \tau_{int}^{eff}}(T_{rec}^{phys}) \cdot \tau_{int}^{eff} \quad (31)$$

$$\Omega(T_{rec}^{phys}; \tau_{int}^{eff}) = \Omega_0(T_{rec}^{phys}) + \frac{\partial \Omega}{\partial \tau_{int}^{eff}}(T_{rec}^{phys}) \cdot \tau_{int}^{eff}$$

The key element of the PRBC is to adjust all of the calibration parameters from the actual value of n_{pulse} to the reference value $n_{pulse}^{ref} = 16.0$. For the following we assume that the value of T_{rec}^{phys} is fixed. We also assume that the PB has no effect on the non-linearity.

Assume that one knows gain $g(n_{pulse,1})$ and offset $\Omega(n_{pulse,1})$ for a certain number $n_{pulse,1}$ of PB, then the values $g(n_{pulse,2})$ and offset $\Omega(n_{pulse,2})$ at a different number $n_{pulse,2}$ follow directly from equations (30) and (31):

$$g(n_{pulse,2}) = g(n_{pulse,1}) + \frac{\partial g}{\partial \tau_{int}^{eff}} \cdot (n_{pulse,1} - n_{pulse,2}) \cdot \tau_{pulse}$$

$$\Omega(n_{pulse,2}) = \Omega(n_{pulse,1}) + \frac{\partial \Omega}{\partial \tau_{int}^{eff}} \cdot (n_{pulse,1} - n_{pulse,2}) \cdot \tau_{pulse} \quad (32)$$

where

$$\tau_{int,1}^{eff} = \tau_{int} - n_{pulse,1} \cdot \tau_{pulse} \quad \tau_{int,2}^{eff} = \tau_{int} - n_{pulse,2} \cdot \tau_{pulse}$$

Assume that one knows the counts $C(n_{pulse,1}; T_A)$ at a given scene temperature T_A for a certain number $n_{pulse,1}$ of PB. The value $C(n_{pulse,2}; T_A)$ at a different number $n_{pulse,2}$ can be calculated as follows. Neglecting again the non-linearity ($T_{nl} \approx 0$):

$$\begin{aligned} C(n_{pulse,1}; T_A) &= g(n_{pulse,1}) \cdot T_A + \Omega(n_{pulse,1}) \\ C(n_{pulse,2}; T_A) &= g(n_{pulse,2}) \cdot T_A + \Omega(n_{pulse,2}) \end{aligned} \quad (33)$$

Using (32) and (33) one finds:

$$\begin{aligned} C(n_{pulse,2}; T_A) &= g(n_{pulse,2}) \cdot T_A + \Omega(n_{pulse,2}) = \\ & \left[g(n_{pulse,1}) + \frac{\partial g}{\partial \tau_{int}^{eff}} \cdot [\tau_{int,2}^{eff} - \tau_{int,1}^{eff}] \right] \cdot T_A + \left[\Omega(n_{pulse,1}) + \frac{\partial \Omega}{\partial \tau_{int}^{eff}} \cdot [\tau_{int,2}^{eff} - \tau_{int,1}^{eff}] \right] = \\ & C(n_{pulse,1}; T_A) + (\tau_{int,2}^{eff} - \tau_{int,1}^{eff}) \cdot \left[\frac{\partial g}{\partial \tau_{int}^{eff}} \cdot T_A + \frac{\partial \Omega}{\partial \tau_{int}^{eff}} \right] = \\ & C(n_{pulse,1}; T_A) + (n_{pulse,1} - n_{pulse,2}) \cdot \tau_{pulse} \cdot \left[\frac{\partial g}{\partial \tau_{int}^{eff}} \cdot T_A + \frac{\partial \Omega}{\partial \tau_{int}^{eff}} \right] \end{aligned} \quad (34)$$

and therefore the master equation for the PRBC of a count $C(T_A)$:

$$\boxed{C(n_{pulse,2}; T_A) = C(n_{pulse,1}; T_A) + (n_{pulse,1} - n_{pulse,2}) \cdot \tau_{pulse} \cdot \left[\frac{\partial g}{\partial \tau_{int}^{eff}} \cdot T_A + \frac{\partial \Omega}{\partial \tau_{int}^{eff}} \right]} \quad (35)$$

Implementing this correction into the calibration algorithm requires explicit knowledge of the scene temperature T_A . For the cold calibration counts $T_A = T_c^{eff}$ and for the hot counts $T_A = T_h^{eff}$. For the PRBC of the Earth view counts we can calculate a first guess of the scene temperature in the following way:

$$\begin{aligned} T_A^{(1)} &\approx \frac{C(n_{pulse}) - \Omega(n_{pulse}^{ref})}{g(n_{pulse}^{ref})} \\ g(n_{pulse}^{ref}) &\approx \frac{\bar{C}_h(n_{pulse}^{ref}) - \bar{C}_c(n_{pulse}^{ref})}{T_h^{eff} - T_c^{eff}} \\ \Omega(n_{pulse}^{ref}) &\approx T_c^{eff} - \frac{\bar{C}_c(n_{pulse}^{ref})}{g(n_{pulse}^{ref})} \end{aligned} \quad (36)$$

This value $T_A^{(1)}$ is then used in (35).

We note that the blanking algorithm given in this section is a first-order correction, and does not take into account blanking pulses that may overlap into the integration reset time, or onto the following sample. Experience with ground test data has shown that a more sophisticated blanking correction may need to be derived after launch if blanking is used.

6.5 On-Orbit NEDT Verification

Random fluctuations in the received power of a radiometer measurement for a given scene are manifested in the value of the raw noise equivalent temperature (NEDT):

$$\Delta T_{NEDT,i} = (T_{rcv} + T_i) \frac{1}{\sqrt{B\tau_{int}}} \quad i = c, h, cn, hn, E \quad (37)$$

B is the bandwidth and τ_{int} is the integration time. T_i is the temperature of the scene and T_{rcv} is the noise temperature of the receiver. This NEDT translates into a fluctuation of the scene counts ΔC_i according to equation (15):

$$\Delta T_{NEDT,i} = 2 \cdot \frac{u}{g^2} \cdot C_i \cdot \Delta C_i + \frac{\Delta C_i}{g'} \quad (38)$$

If the non-linearity is zero, (38) simplifies to:

$$\Delta T_{NEDT,i} = \frac{\Delta C_i}{g} \quad (39)$$

Hereby we have assumed that the scene temperature T_i does not vary. This assumption is fulfilled for using calibration scenes $i = c, h, cn, hn$ but in general not for Earth scenes. Therefore we use only the calibration counts for NEDT verification. We can calculate ΔC_i as the standard deviation of the counts over all samples within $\pm n_i$ scans. The number n_i of scans should be large enough to have a sufficient number of samples but small enough so that the gain g as well as the scene temperature T_i of the calibration target do not vary within the n_i scans of the calibration cycle. We can also calculate ΔC_i as the standard deviation of the either the scan-to-scan, or sample to sample difference, divided by square-root 2, which removes the majority of the drift of the gain or hot load temperature.

If B and τ_{int} are fixed, the NEDT verification is basically equivalent to determining the receiver noise temperature T_{rcv} from equation (37) or verifying its pre-launch value. The value for T_{rcv} that we determine that way should not depend which calibration target (c, cn, h or hn) has been used in (38) and (37). T_{rcv} can depend on the physical temperature of the receiver T_{rcv}^{phys} . Using data from many orbits one can trend T_{rcv} as function of T_{rcv}^{phys} the same way as gain, offset and non-linearity (section 6.2).

Once T_{rcv} has been determined, one can use its value in order to compute the general NEDT that includes calibration amplification factors (CAF) and possible gain variations within a calibration cycle (c.f. BATC 2249401 and BATC 2249262).

7 Antenna Pattern Theory

This chapter describes the general background and formalism for the GMI antenna pattern and conversion from TOA brightness temperatures into antenna temperatures, which will be used for the in-flight orbit simulator (section 8.6) and the derivation of the antenna pattern coefficients (chapter 9).

7.1 Vector Effective Height

Let $\boldsymbol{\varepsilon}_p, \boldsymbol{\varepsilon}_q, p, q = 1, 2$ be arbitrary orthogonal polarization basis unit vectors. We assume that its components are real numbers. The *complex vector effective height* \mathbf{I} of the antenna polarization port p specifies the complex electric field vector (up to some geometrical factors and constants) at a far distance from the transmitting antenna [2-5]. It is given in terms of the radiation pattern (amplitude f and phase β):

$$\begin{aligned} \mathbf{I}(p) &= I_{pp}^* \boldsymbol{\varepsilon}_p + I_{pq}^* \boldsymbol{\varepsilon}_q \\ I_{pp} &= f_{pp} e^{i\beta_{pp}} \quad I_{pq} = f_{pq} e^{i\beta_{pq}} \end{aligned} \quad (40)$$

The I_{pp} is called the co-pol and I_{pq} the cross pol effective height vector. One can align the polarization basis with the Earth h-pol/v-pol basis at boresight by properly clocking the feedhorns, but for the moment we consider any general polarization basis. Using complex conjugation in the definition of the vector components of \mathbf{I} in (40) is purely a matter of convenience. The reason for doing it will become clear when taking the complex scalar products between \mathbf{I} and other vectors.

The normalization of the radiation pattern functions in (40) is:

$$\int d\Omega \left[|f_{pp}|^2 + |f_{pq}|^2 \right] = 1 \quad \int d\Omega \left[|f_{qp}|^2 + |f_{qq}|^2 \right] = 1 \quad (41)$$

7.2 Incident and Received Fields

We now use the antenna as receiver. For that, we consider an incident quasi-monochromatic, plane electric wave:

$$\mathbf{E} = E_p \boldsymbol{\varepsilon}_p + E_q \boldsymbol{\varepsilon}_q \quad (42)$$

with bandwidth $d\nu$ coming from an incident direction subtitled by the solid angle

$$d\Omega = d\theta \sin(\theta) d\phi \quad (43)$$

θ, ϕ are spherical polar coordinates with respect to an arbitrary coordinate system. It is common to put the z-axis of the coordinate system along boresight, which is the direction in which the amplitude of the co-pol pattern is maximal. We label this coordinate system the Main Beam System *MBS* (Appendix A.7). BATC uses a different coordinate system for specifying the antenna patterns, which the Main reflector coordinate System *MRCs* (Appendix A.6 and slightly different (section 7.4). For the following it is not necessary to make a specific assumption about the coordinate system.

The reciprocity theorem states that switching from a transmitting to a receiving antenna means switching ingoing and outgoing fields. The electric field component received by port p is the complex scalar product between the effective height vector and the electric field:

$$\mathbf{E}'_p \propto \mathbf{I}(p)^\dagger \cdot \mathbf{E} = I_{pp} \mathbf{E}_p + I_{pq} \mathbf{E}_q \quad (44)$$

or:

$$\begin{pmatrix} \mathbf{E}'_p \\ \mathbf{E}'_q \end{pmatrix} \propto \begin{pmatrix} I_{pp} & I_{pq} \\ I_{qp} & I_{qq} \end{pmatrix} \cdot \begin{pmatrix} \mathbf{E}_p \\ \mathbf{E}_q \end{pmatrix} \quad (45)$$

where the primed \mathbf{E}' refers to the received electric field and the unprimed \mathbf{E} to the incoming electric field.

7.3 Incident and Received Power – Stokes Vector

The power that is received at port p from the electric field (44) is:

$$dP_p \propto \langle |\mathbf{E}'_p|^2 \rangle d\Omega \quad (46)$$

where $\langle \rangle$ denotes the time average.

More generally, we consider the components of the coherency tensor matrix:

$$\rho \equiv \left\langle \begin{pmatrix} \mathbf{E}'_p \\ \mathbf{E}'_q \end{pmatrix} \otimes (\mathbf{E}'_p^*, \mathbf{E}'_q^*) \right\rangle \equiv \begin{pmatrix} \langle |\mathbf{E}'_p \cdot \mathbf{E}'_p^*| \rangle & \langle |\mathbf{E}'_p \cdot \mathbf{E}'_q^*| \rangle \\ \langle |\mathbf{E}'_q \cdot \mathbf{E}'_p^*| \rangle & \langle |\mathbf{E}'_q \cdot \mathbf{E}'_q^*| \rangle \end{pmatrix} \quad (47)$$

Substituting (44) and (40), and using the relation:

$$\alpha\beta + \alpha^*\beta^* = 2\text{Re}(\alpha\beta) - 2\text{Im}(\alpha\beta) \quad (48)$$

we find for the components in (48):

$$\begin{aligned} \langle |\mathbf{E}'_p \cdot \mathbf{E}'_p^*| \rangle &= [I_{pp} \mathbf{E}_p + I_{pq} \mathbf{E}_q] \cdot [I_{pp} \mathbf{E}_p + I_{pq} \mathbf{E}_q]^* = \\ &|I_{pp}|^2 |\mathbf{E}_p|^2 + |I_{pq}|^2 |\mathbf{E}_q|^2 + I_{pp} \mathbf{E}_p I_{pq}^* \mathbf{E}_q^* + I_{pq} \mathbf{E}_q I_{pp}^* \mathbf{E}_p^* = \\ &|f_{pp}|^2 |\mathbf{E}_p|^2 + |f_{pq}|^2 |\mathbf{E}_q|^2 + \text{Re}[I_{pp} I_{pq}^*] 2\text{Re}[\mathbf{E}_p \mathbf{E}_q^*] - \text{Im}[I_{pp} I_{pq}^*] 2\text{Im}[\mathbf{E}_p \mathbf{E}_q^*] \end{aligned} \quad (49)$$

$$\begin{aligned} \langle |\mathbf{E}'_q \cdot \mathbf{E}'_q^*| \rangle &= [I_{qp} \mathbf{E}_p + I_{qq} \mathbf{E}_q] \cdot [I_{qp} \mathbf{E}_p + I_{qq} \mathbf{E}_q]^* = \\ &|I_{qp}|^2 |\mathbf{E}_p|^2 + |I_{qq}|^2 |\mathbf{E}_q|^2 + I_{qp} \mathbf{E}_p I_{qq}^* \mathbf{E}_q^* + I_{qq} \mathbf{E}_q I_{qp}^* \mathbf{E}_p^* = \\ &|f_{qp}|^2 |\mathbf{E}_p|^2 + |f_{qq}|^2 |\mathbf{E}_q|^2 + \text{Re}[I_{qp} I_{qq}^*] 2\text{Re}[\mathbf{E}_p \mathbf{E}_q^*] - \text{Im}[I_{qp} I_{qq}^*] 2\text{Im}[\mathbf{E}_p \mathbf{E}_q^*] \end{aligned} \quad (50)$$

$$\begin{aligned} \langle |\mathbf{E}'_p \cdot \mathbf{E}'_q^*| \rangle &= [I_{pp} \mathbf{E}_p + I_{pq} \mathbf{E}_q] \cdot [I_{qp} \mathbf{E}_p + I_{qq} \mathbf{E}_q]^* = \\ &I_{pp} I_{qp}^* |\mathbf{E}_p|^2 + I_{pq} I_{qq}^* |\mathbf{E}_q|^2 + I_{pq} I_{qp}^* \mathbf{E}_q \mathbf{E}_p^* + I_{pp} I_{qq}^* \mathbf{E}_p \mathbf{E}_q^* = \\ &I_{pp} I_{qp}^* |\mathbf{E}_p|^2 + I_{pq} I_{qq}^* |\mathbf{E}_q|^2 + \\ &[I_{pp} I_{qq}^* + I_{pq} I_{qp}^*] \text{Re}(\mathbf{E}_p \mathbf{E}_q^*) + i [I_{pp} I_{qq}^* - I_{pq} I_{qp}^*] \text{Im}(\mathbf{E}_p \mathbf{E}_q^*) \end{aligned} \quad (51)$$

The real and imaginary parts of (51) are:

$$\begin{aligned}
2\text{Re}\left(\left\langle\left|E'_p \cdot E_q'^*\right|\right\rangle\right) &= 2\text{Re}\left(I_{pp}I_{qp}^*\right)\left|E_p\right|^2 + 2\text{Re}\left(I_{pq}I_{qq}^*\right)\left|E_q\right|^2 + \\
\text{Re}\left[I_{pp}I_{qq}^* + I_{pq}I_{qp}^*\right]2\text{Re}\left[E_pE_q^*\right] &- \text{Im}\left[I_{pp}I_{qq}^* - I_{pq}I_{qp}^*\right]2\text{Im}\left[E_pE_q^*\right]
\end{aligned} \tag{52}$$

$$\begin{aligned}
2\text{Im}\left(\left\langle\left|E'_p \cdot E_q'^*\right|\right\rangle\right) &= 2\text{Im}\left(I_{pp}I_{qp}^*\right)\left|E_p\right|^2 + 2\text{Im}\left(I_{pq}I_{qq}^*\right)\left|E_q\right|^2 + \\
\text{Im}\left[I_{pp}I_{qq}^* + I_{pq}I_{qp}^*\right]2\text{Re}\left[E_pE_q^*\right] &+ \text{Re}\left[I_{pp}I_{qq}^* - I_{pq}I_{qp}^*\right]2\text{Im}\left[E_pE_q^*\right]
\end{aligned} \tag{53}$$

It is convenient to rearrange (47) as *modified Stokes vector*^{*}:

$$I_S d\Omega dv \propto \begin{pmatrix} \langle E'_p \cdot E_p'^* \rangle \\ \langle E'_q \cdot E_q'^* \rangle \\ 2\text{Re}\left[\langle E'_p \cdot E_q'^* \rangle\right] \\ 2\text{Im}\left[\langle E'_p \cdot E_q'^* \rangle\right] \end{pmatrix} d\Omega dv \tag{54}$$

We can then write (49), (50), (52) and (53) in compact form as a matrix multiplication:

$$\begin{pmatrix} \langle E'_p \cdot E_p'^* \rangle \\ \langle E'_q \cdot E_q'^* \rangle \\ 2\text{Re}\left[\langle E'_p \cdot E_q'^* \rangle\right] \\ 2\text{Im}\left[\langle E'_p \cdot E_q'^* \rangle\right] \end{pmatrix} d\Omega dv = \Gamma \cdot \begin{pmatrix} \langle E_p \cdot E_p^* \rangle \\ \langle E_q \cdot E_q^* \rangle \\ 2\text{Re}\left[\langle E_p \cdot E_q^* \rangle\right] \\ 2\text{Im}\left[\langle E_p \cdot E_q^* \rangle\right] \end{pmatrix} d\Omega dv \tag{55}$$

with

$$\Gamma = \begin{pmatrix} |f_{pp}|^2 & |f_{pq}|^2 & \text{Re}\left[I_{pp}I_{pq}^*\right] & -\text{Im}\left[I_{pp}I_{pq}^*\right] \\ |f_{qp}|^2 & |f_{qq}|^2 & \text{Re}\left[I_{qp}I_{qq}^*\right] & \text{Im}\left[I_{qp}I_{qq}^*\right] \\ 2\text{Re}\left[I_{pp}I_{qp}^*\right] & 2\text{Re}\left[I_{qq}I_{pq}^*\right] & \text{Re}\left[I_{pp}I_{qq}^* + I_{pq}I_{qp}^*\right] & -\text{Im}\left[I_{pp}I_{qq}^* - I_{pq}I_{qp}^*\right] \\ 2\text{Im}\left[I_{pp}I_{qp}^*\right] & -2\text{Im}\left[I_{qq}I_{pq}^*\right] & \text{Im}\left[I_{pp}I_{qq}^* + I_{pq}I_{qp}^*\right] & \text{Re}\left[I_{pp}I_{qq}^* - I_{pq}I_{qp}^*\right] \end{pmatrix} \tag{56}$$

The antenna temperature received at port p is related to the received average power

$$T_{A,p} \propto \int d\Omega \int dv \left\langle \left|E'_p\right|^2 \right\rangle \tag{57}$$

More generally, the antenna temperature Stokes vector is:

$$\mathbf{T}_A \propto \int d\Omega dv I_S \tag{58}$$

The modified brightness temperature Stokes vector is

^{*} It does not transform like a vector under rotations of the coordinate system. The coherency matrix (47) transforms like a tensor under rotations of the coordinate system.

$$\mathbf{T}_B \propto \int d\nu \begin{pmatrix} \langle E_p \cdot E_p^* \rangle \\ \langle E_q \cdot E_q^* \rangle \\ 2\text{Re}[\langle E_p \cdot E_q^* \rangle] \\ 2\text{Im}[\langle E_p \cdot E_q^* \rangle] \end{pmatrix} \quad (59)$$

Assuming that the antenna pattern functions are independent of ν within the bandwidth $d\nu$, one can then write:

$$\begin{pmatrix} T_{A,p} \\ T_{A,q} \\ T_{A,S3} \\ T_{A,S4} \end{pmatrix} = \int d\Omega \Gamma(\theta, \phi) \cdot \begin{pmatrix} T_{B,p}(\theta, \phi) \\ T_{B,q}(\theta, \phi) \\ T_{B,S3}(\theta, \phi) \\ T_{B,S4}(\theta, \phi) \end{pmatrix} \quad (60)$$

with

$$\Gamma(\theta, \phi) = \begin{pmatrix} |f_{pp}|^2 & |f_{pq}|^2 & \text{Re}[I_{pp}I_{pq}^*] & -\text{Im}[I_{pp}I_{pq}^*] \\ |f_{qp}|^2 & |f_{qq}|^2 & \text{Re}[I_{qq}I_{qp}^*] & \text{Im}[I_{qq}I_{qp}^*] \\ 2\text{Re}[I_{pp}I_{qp}^*] & 2\text{Re}[I_{qq}I_{pq}^*] & \text{Re}[I_{pp}I_{qq}^* + I_{pq}I_{qp}^*] & -\text{Im}[I_{pp}I_{qq}^* - I_{pq}I_{qp}^*] \\ 2\text{Im}[I_{pp}I_{qp}^*] & -2\text{Im}[I_{qq}I_{pq}^*] & \text{Im}[I_{pp}I_{qq}^* + I_{pq}I_{qp}^*] & \text{Re}[I_{pp}I_{qq}^* - I_{pq}I_{qp}^*] \end{pmatrix} \quad (61)$$

The indices $S3$ and $S4$ in (60) denote the 3rd and 4th Stokes parameters, respectively.

A special case occurs, if the radiation is unpolarized and isotropic at a temperature T .

$$\text{Then: } \begin{pmatrix} T_{B,p}(\theta, \phi) \\ T_{B,q}(\theta, \phi) \\ T_{B,S3}(\theta, \phi) \\ T_{B,S4}(\theta, \phi) \end{pmatrix} = \begin{pmatrix} T \\ T \\ 0 \\ 0 \end{pmatrix} \text{ and because of the normalization condition (41) also}$$

$$\begin{pmatrix} T_{A,p} \\ T_{A,q} \\ T_{A,S3} \\ T_{A,S4} \end{pmatrix} = \begin{pmatrix} T \\ T \\ 0 \\ 0 \end{pmatrix}.$$

7.4 Polarization Basis Rotation

Equation (60) is given in terms of an arbitrary antenna polarization basis $\boldsymbol{\varepsilon}_p, \boldsymbol{\varepsilon}_q$. Ultimately we are interested in the components of the electric field that are given in the Earth vertical (v) and horizontal (h) polarization basis $\boldsymbol{\varepsilon}_v, \boldsymbol{\varepsilon}_h$, which is defined as:

$$\boldsymbol{\varepsilon}_h = \frac{\mathbf{k} \times \mathbf{n}}{|\mathbf{k} \times \mathbf{n}|} \quad \boldsymbol{\varepsilon}_v = \boldsymbol{\varepsilon}_h \times \mathbf{k} \quad (62)$$

where \mathbf{k} is a unit vector pointing in the propagation direction of the electromagnetic

wave from the Earth point to the S/C and \mathbf{n} is the Earth surface normal unit vector. In this section we will derive how the modified Stokes vector (59) transforms under rotations of the polarization basis.

Let $\boldsymbol{\varepsilon}_{p1}, \boldsymbol{\varepsilon}_{q1}$ and $\boldsymbol{\varepsilon}_{p2}, \boldsymbol{\varepsilon}_{q2}$ be 2 different polarization basis systems, which are rotated by an angle α , i.e.:

$$\boldsymbol{\varepsilon}_{p2} \cdot \boldsymbol{\varepsilon}_{p1} = \boldsymbol{\varepsilon}_{q2} \cdot \boldsymbol{\varepsilon}_{q1} = \cos(\alpha) \quad \boldsymbol{\varepsilon}_{q2} \cdot \boldsymbol{\varepsilon}_{p1} = \sin(\alpha) = -\boldsymbol{\varepsilon}_{q1} \cdot \boldsymbol{\varepsilon}_{p2} \quad (63)$$

We assume that all the basis vector components are real numbers. For the incident electric field (42):

$$\begin{aligned} \mathbf{E} &= E_{p2} \boldsymbol{\varepsilon}_{p2} + E_{q2} \boldsymbol{\varepsilon}_{q2} \\ &= E_{p2} \left[(\boldsymbol{\varepsilon}_{p2} \cdot \boldsymbol{\varepsilon}_{p1}) \boldsymbol{\varepsilon}_{p1} + (\boldsymbol{\varepsilon}_{p2} \cdot \boldsymbol{\varepsilon}_{q1}) \boldsymbol{\varepsilon}_{q1} \right] + E_{q2} \left[(\boldsymbol{\varepsilon}_{q2} \cdot \boldsymbol{\varepsilon}_{p1}) \boldsymbol{\varepsilon}_{p1} + (\boldsymbol{\varepsilon}_{q2} \cdot \boldsymbol{\varepsilon}_{q1}) \boldsymbol{\varepsilon}_{q1} \right] \\ &= \left[E_{p2} (\boldsymbol{\varepsilon}_{p2} \cdot \boldsymbol{\varepsilon}_{p1}) + E_{q2} (\boldsymbol{\varepsilon}_{q2} \cdot \boldsymbol{\varepsilon}_{p1}) \right] \boldsymbol{\varepsilon}_{p1} + \left[E_{p2} (\boldsymbol{\varepsilon}_{p2} \cdot \boldsymbol{\varepsilon}_{q1}) + E_{q2} (\boldsymbol{\varepsilon}_{q2} \cdot \boldsymbol{\varepsilon}_{q1}) \right] \boldsymbol{\varepsilon}_{q1} \\ &\equiv E_{p1} \boldsymbol{\varepsilon}_{p1} + E_{q1} \boldsymbol{\varepsilon}_{q1} \end{aligned} \quad (64)$$

Therefore

$$\begin{aligned} E_{p1} &= \left[E_{p2} (\boldsymbol{\varepsilon}_{p2} \cdot \boldsymbol{\varepsilon}_{p1}) + E_{q2} (\boldsymbol{\varepsilon}_{q2} \cdot \boldsymbol{\varepsilon}_{p1}) \right] \\ E_{q1} &= \left[E_{p2} (\boldsymbol{\varepsilon}_{p2} \cdot \boldsymbol{\varepsilon}_{q1}) + E_{q2} (\boldsymbol{\varepsilon}_{q2} \cdot \boldsymbol{\varepsilon}_{q1}) \right] \end{aligned} \quad (65)$$

or

$$\begin{pmatrix} E_{p1} \\ E_{q1} \end{pmatrix} = \begin{pmatrix} (\boldsymbol{\varepsilon}_{p1} \cdot \boldsymbol{\varepsilon}_{p2}) & (\boldsymbol{\varepsilon}_{p1} \cdot \boldsymbol{\varepsilon}_{q2}) \\ (\boldsymbol{\varepsilon}_{q1} \cdot \boldsymbol{\varepsilon}_{p2}) & (\boldsymbol{\varepsilon}_{q1} \cdot \boldsymbol{\varepsilon}_{q2}) \end{pmatrix} \cdot \begin{pmatrix} E_{p2} \\ E_{q2} \end{pmatrix} = \begin{pmatrix} \cos(\alpha) & \sin(\alpha) \\ -\sin(\alpha) & \cos(\alpha) \end{pmatrix} \cdot \begin{pmatrix} E_{p2} \\ E_{q2} \end{pmatrix} \equiv r[\alpha] \cdot \begin{pmatrix} E_{p2} \\ E_{q2} \end{pmatrix} \quad (66)$$

The transformation for the components of the (59) are:

$$\begin{aligned} E_{p1} E_{p1}^* &= \left[\cos(\alpha) E_{p2} + \sin(\alpha) E_{q2} \right] \cdot \left[\cos(\alpha) E_{p2}^* + \sin(\alpha) E_{q2}^* \right] = \\ &\cos^2(\alpha) E_{p2} \cdot E_{p2}^* + \left[\cos(\alpha) \sin(\alpha) \right] \left[E_{p2} E_{q2}^* + E_{q2} E_{p2}^* \right] + \sin^2(\alpha) E_{q2} \cdot E_{q2}^* = \\ &\cos^2(\alpha) E_{p2} \cdot E_{p2}^* + \sin^2(\alpha) E_{q2} \cdot E_{q2}^* + \cos(\alpha) \sin(\alpha) 2 \operatorname{Re} \left[E_{p2} E_{q2}^* \right] = \\ &\cos^2(\alpha) E_{p2} \cdot E_{p2}^* + \sin^2(\alpha) E_{q2} \cdot E_{q2}^* + \frac{1}{2} \sin(2\alpha) 2 \operatorname{Re} \left[E_{p2} E_{q2}^* \right] \end{aligned} \quad (67)$$

$$\begin{aligned} E_{q1} E_{q1}^* &= \left[\cos(\alpha) E_{q2} - \sin(\alpha) E_{p2} \right] \cdot \left[\cos(\alpha) E_{q2}^* - \sin(\alpha) E_{p2}^* \right] = \\ &\cos^2(\alpha) E_{q2} \cdot E_{q2}^* - \left[\cos(\alpha) \sin(\alpha) \right] \left[E_{p2} E_{q2}^* + E_{q2} E_{p2}^* \right] + \sin^2(\alpha) E_{p2} \cdot E_{p2}^* = \\ &\cos^2(\alpha) E_{q2} \cdot E_{q2}^* + \sin^2(\alpha) E_{p2} \cdot E_{p2}^* - \cos(\alpha) \sin(\alpha) 2 \operatorname{Re} \left[E_{p2} E_{q2}^* \right] = \\ &\cos^2(\alpha) E_{q2} \cdot E_{q2}^* + \sin^2(\alpha) E_{p2} \cdot E_{p2}^* - \frac{1}{2} \sin(2\alpha) 2 \operatorname{Re} \left[E_{p2} E_{q2}^* \right] \end{aligned} \quad (68)$$

$$\begin{aligned}
2 \operatorname{Re} \left[E_{p1} \cdot E_{q1}^* \right] &= \\
2 \operatorname{Re} \left[\left(\cos(\alpha) E_{p2} + \sin(\alpha) E_{q2} \right) \left(\cos(\alpha) E_{q2}^* - \sin(\alpha) E_{p2}^* \right) \right] &= \\
-2 \cos(\alpha) \sin(\alpha) E_{p2} \cdot E_{p2}^* + 2 \cos(\alpha) \sin(\alpha) E_{q2} \cdot E_{q2}^* + & \quad (69)
\end{aligned}$$

$$\begin{aligned}
\left[\cos^2(\alpha) - \sin^2(\alpha) \right] 2 \operatorname{Re} \left[E_{p2} E_{q2}^* \right] &= \\
-\sin(2\alpha) E_{p2} \cdot E_{p2}^* + \sin(2\alpha) E_{q2} \cdot E_{q2}^* + \cos(2\alpha) 2 \operatorname{Re} \left[E_{p2} E_{q2}^* \right] & \\
2 \operatorname{Im} \left[E_{p2} \cdot E_{q2}^* \right] &= \\
2 \operatorname{Im} \left[\left(\cos(\alpha) E_{p2} + \sin(\alpha) E_{q2} \right) \left(\cos(\alpha) E_{q2}^* - \sin(\alpha) E_{p2}^* \right) \right] &= \\
\cos^2(\alpha) 2 \operatorname{Im} \left[E_{p2} E_{q2}^* \right] - \sin^2(\alpha) 2 \operatorname{Im} \left[E_{q2} E_{p2}^* \right] &= \\
\left[\cos^2(\alpha) + \sin^2(\alpha) \right] 2 \operatorname{Im} \left[E_{p2} E_{q2}^* \right] = 2 \operatorname{Im} \left[E_{p2} E_{q2}^* \right] & \quad (70)
\end{aligned}$$

Equations (67) - (70) can be written compact in matrix form as:

$$\begin{pmatrix} \langle E_{p1} \cdot E_{p1}^* \rangle \\ \langle E_{q1} \cdot E_{q1}^* \rangle \\ 2 \operatorname{Re} \left[\langle E_{p1} \cdot E_{q1}^* \rangle \right] \\ 2 \operatorname{Im} \left[\langle E_{p1} \cdot E_{q1}^* \rangle \right] \end{pmatrix} = R[\alpha] \cdot \begin{pmatrix} \langle E_{p2} \cdot E_{p2}^* \rangle \\ \langle E_{q2} \cdot E_{q2}^* \rangle \\ 2 \operatorname{Re} \left[\langle E_{p2} \cdot E_{q2}^* \rangle \right] \\ 2 \operatorname{Im} \left[\langle E_{p2} \cdot E_{q2}^* \rangle \right] \end{pmatrix} \quad (71)$$

with the rotation matrix:

$$R[\alpha] = \begin{pmatrix} \cos^2(\alpha) & \sin^2(\alpha) & \frac{1}{2} \sin(2\alpha) & 0 \\ \sin^2(\alpha) & \cos^2(\alpha) & -\frac{1}{2} \sin(2\alpha) & 0 \\ -\sin(2\alpha) & \sin(2\alpha) & \cos(2\alpha) & 0 \\ 0 & 0 & 0 & 1 \end{pmatrix} = R^{-1}[-\alpha] \quad (72)$$

Inserting (71) into (59) gives:

$$\begin{pmatrix} T_{B,p1}(\theta, \phi) \\ T_{B,q1}(\theta, \phi) \\ T_{B,S3,1}(\theta, \phi) \\ T_{B,S4,1}(\theta, \phi) \end{pmatrix} = R[\alpha(\theta, \phi)] \cdot \begin{pmatrix} T_{B,p2}(\theta, \phi) \\ T_{B,q2}(\theta, \phi) \\ T_{B,S3,2}(\theta, \phi) \\ T_{B,S4,2}(\theta, \phi) \end{pmatrix} \quad (73)$$

7.5 BATC Antenna Patterns

7.5.1 BATC Patterns in the MRCS

The antenna patterns are specified in the main reflector coordinate system *MRCS* (Appendix A.6). BATC provides simulation results for the directivity amplitude D and the

phase angle β of the antenna pattern. Directivity D' and the amplitude f' in (40) are related by:

$$D_{pq}(\theta', \phi') \equiv 4\pi |f'_{pq}(\theta', \phi')|^2 \quad (74)$$

The prime indicates that the patterns are given in the *MRCs*. Polar angle θ' and azimuth angle ϕ' are the spherical polar coordinates in the *MRCs*.

The polarization axes $\mathbf{e}'_p, \mathbf{e}'_q, p, q = 1, 2$, that BATC uses to specify the patterns, are the spherical unit vectors into the θ' and ϕ' direction of the *MRCs*:

$$\begin{aligned} \mathbf{e}'_1 &= \mathbf{f}'_\phi = -\sin(\phi')\mathbf{f}'_1 + \cos(\phi')\mathbf{f}'_2 \\ \mathbf{e}'_2 &= \mathbf{f}'_\theta = \cos(\theta')\cos(\phi')\mathbf{f}'_1 + \cos(\theta')\sin(\phi')\mathbf{f}'_2 - \sin(\theta')\mathbf{f}'_3 \end{aligned} \quad (75)$$

Co and cross-pol values of D and β for the ϕ' port are given on a regular θ', ϕ' grid consisting of 1800 equally spaced θ' -values ranging from 0° to 180° and 359 equally spaced ϕ' -values ranging from -180° to $+179^\circ$.

7.5.2 Port Symmetry

We assume symmetry in the ports for the simulated patterns. That means that effect of the antenna on a vertical polarized field is the same as on an horizontal polarized wave. As a consequence, the total received power must be equal to the incoming power

or:

$$\int d\Omega \left[\langle E_p \cdot E_p^* + E_q \cdot E_q^* \rangle \right]_{rec} = \left[\langle E_p \cdot E_p^* + E_q \cdot E_q^* \rangle \right]_{inc} \quad (76)$$

$$T_{A,p} + T_{A,q} = T_{B,p} + T_{B,q}$$

Using (45) that translates into:

$$\int d\Omega \begin{pmatrix} I'_{pp} & I'_{pq} \\ I'_{qp} & I'_{qq} \end{pmatrix}^\dagger \cdot \begin{pmatrix} I'_{pp} & I'_{pq} \\ I'_{qp} & I'_{qq} \end{pmatrix} = \int d\Omega \begin{pmatrix} I'^{*}_{pp} \cdot I'_{pp} + I'^{*}_{qp} \cdot I'_{qp} & I'^{*}_{pp} \cdot I'_{pq} + I'^{*}_{qp} \cdot I'_{qq} \\ I'^{*}_{pq} \cdot I'_{pp} + I'^{*}_{qq} \cdot I'_{qp} & I'^{*}_{pq} \cdot I'_{pq} + I'^{*}_{qq} \cdot I'_{qq} \end{pmatrix} = \begin{pmatrix} 1 & 0 \\ 0 & 1 \end{pmatrix} \quad (77)$$

which is fulfilled for:

$$\begin{aligned} I'_{pp} &= I'^{*}_{qq} \\ I'_{pq} &= -I'^{*}_{qp} \end{aligned} \quad (78)$$

We want to note that (76) and (78) hold if and only if there is symmetry in the ports.

7.5.3 Consistency Checks

We have performed the following consistency checks on the BATC values for the 10.65 GHz patterns:

1. We have checked that the normalization (41) is fulfilled, which is equivalent to:

$$\int d\Omega' [D_{pp}(\theta', \phi') + D_{pq}(\theta', \phi')] = \int_0^\pi d\theta' \sin(\theta') \int_0^{2\pi} d\phi' [D_{pp}(\theta', \phi') + D_{pq}(\theta', \phi')] = 4\pi \quad (79)$$

It is correct up to about 0.3%. The small error is almost independent on the method used for performing the numerical integration. We attribute it to the finite grid resolution.

2. At $\theta' = 0$ and at $\theta' = 180^\circ$ all values of the azimuth angle correspond to the same point in space. However, according to (75) the polarization basis unit vectors change with ϕ' . This is an artifact of the spherical coordinate basis, whose coordinate unit vectors are not constant as in a Cartesian basis but vary from point to point. Therefore, also the values of $f(\theta' = 0, \phi')$ and $\beta(\theta' = 0, \phi')$ or $f(\theta' = 180^\circ, \phi')$ and $\beta(\theta' = 180^\circ, \phi')$ in (40) vary with ϕ' , even though all values of ϕ' correspond to the same point in space. However, when we transform the components of (40) into the Cartesian basis $\mathbf{f}'_i, i = 1, \dots, 3$, in which the unit vectors are constant, we find that they do not depend on ϕ' .

7.5.4 Scanning

The provided antenna patterns correspond to a nominal boresight direction or plane of incidence. During the scan the boresight and plane of incidence are rotating around the nadir pointing the z-axis of F , i.e. \mathbf{e}_3 by the scan angle α_{scan} . Therefore also the whole $MRCs$ is rotating around \mathbf{e}_3 by α_{scan} .

7.5.5 Transformation of the Antenna Patterns into the MBS

For the determination of the APC coefficients it is most convenient to use the MBS rather than the $MRCs$. This requires a coordinate transformation of the antenna patterns.

$$\begin{aligned} \mathbf{I}'(p) &= I'_{pp} \mathbf{e}'_p + I'_{pq} \mathbf{e}'_q \\ I'_{pp} &= f'_{pp} e^{i\beta'_{pp}} \quad I'_{pq} = f'_{pq} e^{i\beta'_{pq}} \\ p &= \phi', q = \theta' \end{aligned} \quad (80)$$

is the complex effective height vector in the $MRCs$ using the spherical polarization basis $\mathbf{f}'_\phi, \mathbf{f}'_\theta$ from (75). The first step to properly transforming \mathbf{I}' into the MBS , is to write it into Cartesian components of the basis vectors $\mathbf{f}'_i, i = 1, 2, 3$ using (75). The transformation of the complex Cartesian $MRCs$ vector \mathbf{I}' to the complex Cartesian MBS vector \mathbf{I} is done by the 3 successive rotations (for details c.f. Appendix A.6 and A.7, equation (185)):

$$\begin{aligned} \mathbf{I} &= \mathbf{r}_2(\theta_N) \cdot \mathbf{r}_3(\phi_0) \cdot \mathbf{r}_{F-MRCs} \cdot \mathbf{I}' \\ \mathbf{r}_{F-MRCs} &\approx \mathbf{r}_2(-\theta_N) \end{aligned} \quad (81)$$

As the APC coefficients do not depend on the scan position so for deriving the APC coefficients we can assume without restriction that the antenna is not scanning or that $\alpha_{scan} = 0$.

The final step is to write the complex effective height vector \mathbf{I} in spherical components using the spherical unit vectors $\mathbf{f}_\phi, \mathbf{f}_\theta$ of the MBS , where θ and ϕ denote the MBS spherical polar coordinates.

Representing $\mathbf{I}(\theta, \phi)$ on a regular θ, ϕ grid requires a 2-dimensional interpolation from the original θ', ϕ' to the new θ, ϕ grid. We use a bi-cubic spline.

7.6 Polarization Basis Alignment

7.6.1 Earth V-H Basis

Consider a point at the Earth surface. The intersection of the line between the earth point and the S/C is specified by the spherical polar coordinates θ, ϕ . The vertical (v) and horizontal (h) basis vectors at θ, ϕ are:

$$\boldsymbol{\varepsilon}_{h(\theta,\phi)} = \frac{\mathbf{k}(\theta,\phi) \times \mathbf{n}(\theta,\phi)}{|\mathbf{k}(\theta,\phi) \times \mathbf{n}(\theta,\phi)|} \quad \boldsymbol{\varepsilon}_{v(\theta,\phi)} = \boldsymbol{\varepsilon}_{h(\theta,\phi)} \times \mathbf{k}(\theta,\phi) \quad (82)$$

where $\mathbf{k}(\theta,\phi)$ is a unit vector pointing from the Earth surface point to the S/C and $\mathbf{n}(\theta,\phi)$ is the Earth surface normal unit vector. For a spherical Earth the vectors $\mathbf{k}(\theta,\phi)$, $\mathbf{n}(\theta,\phi)$ and \mathbf{e}_3 , the S/C nadir pointing vector of the geodetic reference frame or nominal nadir pointing flight system (Appendix A.2) lie in the same plane. Therefore in (82):

$$\boldsymbol{\varepsilon}_{h(\theta,\phi)} = \frac{\mathbf{k}(\theta,\phi) \times \mathbf{n}(\theta,\phi)}{|\mathbf{k}(\theta,\phi) \times \mathbf{n}(\theta,\phi)|} \approx \frac{\mathbf{k}(\theta,\phi) \times (-\mathbf{e}_3)}{|\mathbf{k}(\theta,\phi) \times \mathbf{e}_3|} \quad \boldsymbol{\varepsilon}_{v(\theta,\phi)} = \boldsymbol{\varepsilon}_{h(\theta,\phi)} \times \mathbf{k}(\theta,\phi) \quad (83)$$

In the following we will use the approximation (83).

7.6.2 S/C V-H Basis

Boresight is the direction $\theta_{bore}, \phi_{bore}$ at which the co-pol antenna pattern $|f_{pp}(\theta,\phi)|$ peaks. In the MBS $\theta_{bore} = 0$. The vertical (v) and horizontal (h) polarization basis of the S/C at boresight is defined as

$$\boldsymbol{\varepsilon}'_{h,bore} = \frac{\mathbf{k}_{bore} \times (-\mathbf{e}'_3)}{|\mathbf{k}_{bore} \times (-\mathbf{e}'_3)|} \quad \boldsymbol{\varepsilon}'_{v,bore} = \boldsymbol{\varepsilon}'_{h,bore} \times \mathbf{k}_{bore} \quad (84)$$

where $\mathbf{e}'_i, i = 1, 2, 3$ are the Cartesian axes of the in flight system F (Appendix A.5). For the moment we assume that the S/C flies with nominal attitude (no roll, pitch, yaw).

Then F is aligned with the nominal geodetic reference frame and according to (83) the v-h polarization basis of the S/C is the same as the v-h basis of the Earth surface.

7.6.3 Aligning the S/C V-H Basis with the Polarization Basis of the Antenna Pattern

The main task is now to align polarization basis of the antenna pattern with the v-h basis of the Earth at boresight. In 7.5.5 we have shown how to transform the BATC pattern, which are given on a spherical *MRCS* grid to a spherical *MBS* grid. The polarization basis of this transformed pattern are the spherical *MBS* unit vectors $\mathbf{f}_\phi, \mathbf{f}_\theta$. These vectors are not aligned with the v-h polarization vectors $\boldsymbol{\varepsilon}'_{v,bore}$ and $\boldsymbol{\varepsilon}'_{h,bore}$ and therefore the co-pol and cross-pol patterns from 7.5.5 are not the patterns we need. Co-pol and cross pol patterns are polarization dependent. The 3rd method by A. Ludwig [6] describes the most commonly used way to define co-pol and cross-pol components, which guarantees automatically that, aside from unimportant sign differences, the co-pol and cross-pol basis vectors are aligned with the Earth v-h basis at basis.

Ludwig's 3rd definition of the polarization basis vectors $\boldsymbol{\varepsilon}_i, i=1,2$ is:

$$\begin{aligned}\boldsymbol{\varepsilon}_1 &= \sin(\phi)\mathbf{f}_\theta + \cos(\phi)\mathbf{f}_\phi \\ \boldsymbol{\varepsilon}_2 &= \cos(\phi)\mathbf{f}_\theta - \sin(\phi)\mathbf{f}_\phi\end{aligned}\quad (85)$$

The expansions of the spherical unit vectors \mathbf{f}_θ and \mathbf{f}_ϕ into Cartesian unit vectors are:

$$\begin{aligned}\mathbf{f}_\phi &= -\sin(\phi)\mathbf{f}_1 + \cos(\phi)\mathbf{f}_2 \\ \mathbf{f}_\theta &= \cos(\theta)\cos(\phi)\mathbf{f}_1 + \cos(\theta)\sin(\phi)\mathbf{f}_2 - \sin(\theta)\mathbf{f}_3\end{aligned}\quad (86)$$

Therefore in the $\mathbf{f}_1, \mathbf{f}_2, \mathbf{f}_3$ system the polarization vectors $\boldsymbol{\varepsilon}_i, i=1,2$ have the components:

$$\begin{aligned}\boldsymbol{\varepsilon}_1 &= \begin{pmatrix} \cos(\theta)\cos(\phi)\sin(\phi) - \cos(\phi)\sin(\phi) \\ \cos(\theta)\sin^2(\phi) + \cos^2(\phi) \\ -\sin(\theta)\sin(\phi) \end{pmatrix} \\ \boldsymbol{\varepsilon}_2 &= \begin{pmatrix} \cos(\theta)\cos^2(\phi) + \sin^2(\phi) \\ \cos(\theta)\cos(\phi)\sin(\phi) - \cos(\phi)\sin(\phi) \\ -\sin(\theta)\cos(\phi) \end{pmatrix}\end{aligned}\quad (87)$$

At boresight: $\theta = 0$ and therefore

$$\boldsymbol{\varepsilon}_1 = \mathbf{f}_2 \quad \boldsymbol{\varepsilon}_2 = \mathbf{f}_1 \quad (88)$$

The unit vector from the Earth cell to the S/C is in *MBS* Cartesian coordinates:

$$\mathbf{k} = -\begin{pmatrix} \sin(\theta)\cos(\phi) \\ \sin(\theta)\sin(\phi) \\ \cos(\theta) \end{pmatrix} \quad (89)$$

At boresight: $\theta = 0$ and therefore

$$\mathbf{k}_{bore} = -\mathbf{f}_3 \quad (90)$$

Using (84), (184) and assuming that the S/C flies at nominal attitude ($\mathbf{e}'_3 = \mathbf{e}_3$):

The Earth (far field) v-pol and h-pol vectors are:

$$\begin{aligned}\boldsymbol{\varepsilon}_{h,bore} &= \frac{\mathbf{k}_{bore} \times (-\mathbf{e}_3)}{|\mathbf{k}_{bore} \times \mathbf{e}_3|} = \frac{(-\mathbf{f}_3) \times (-\mathbf{e}_3)}{|\mathbf{f}_3 \times \mathbf{e}_3|} = -\mathbf{f}_3 \times \mathbf{f}_1 = -\mathbf{f}_2 = -\boldsymbol{\varepsilon}_1 \\ \boldsymbol{\varepsilon}_{v,bore} &= \boldsymbol{\varepsilon}_{h,bore} \times \mathbf{k}_{bore} = (-\mathbf{f}_2) \times (-\mathbf{f}_3) = \mathbf{f}_1 = \boldsymbol{\varepsilon}_2\end{aligned}\quad (91)$$

That means that in Ludwig's 3rd definition, the Earth polarization basis and the polarization basis of the antenna patterns in the *MBS* are indeed aligned up to a sign.

7.6.4 Principal Plane Cuts of the Antenna Patterns in the V-H Basis

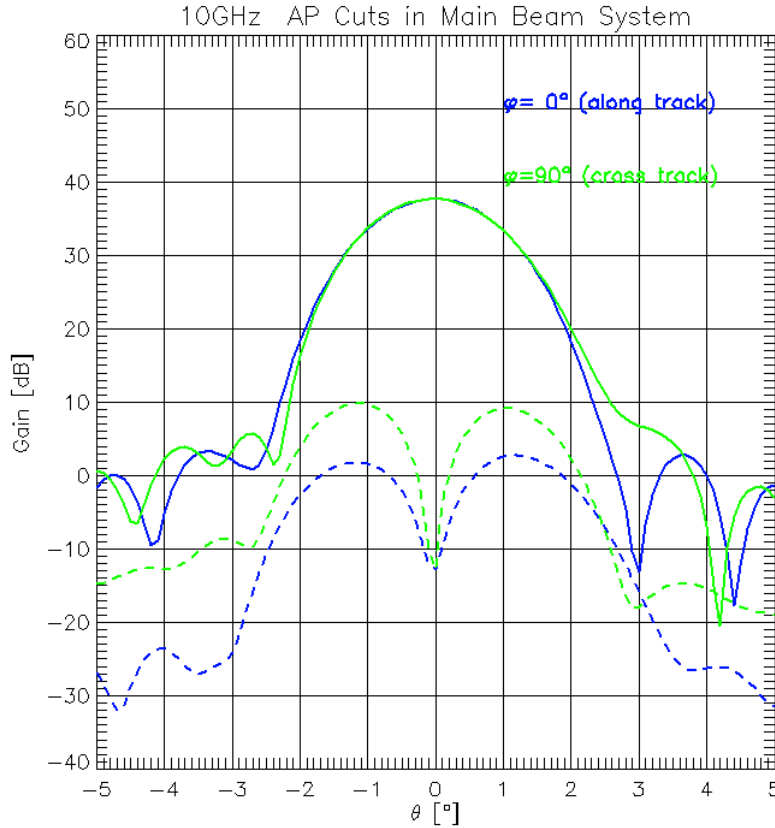


Figure 13: Principal plane cuts of the 10.65 GHz patterns in the MBS v/h basis. The full lines are co-pol (vv and hh), the dashed lines are cross pol (vh and hv). The blue lines are the cuts in the plane $\phi = 0^\circ$ (positive θ) / $\phi = 180^\circ$ (negative θ). The green lines are the cuts in the plane $\phi = +90^\circ$

(positive θ) / $\phi = -90^\circ$ (negative θ). The plots are displaying the values $\frac{1}{2}4\pi|f_{vv}|^2$ and

$\frac{1}{2}4\pi|f_{vh}|^2$, respectively.

Figure 13 shows the principal plane cuts of the co-pol gain ($\frac{1}{2}4\pi|f_{vv}|^2$) and cross-pol gain ($\frac{1}{2}4\pi|f_{vh}|^2$) in the $\phi = 0^\circ / \phi = 180^\circ$ plane and the $\phi = +90^\circ / \phi = -90^\circ$ plane at 10.65 GHz using the MBS v/h basis from section 7.6.3.

Of course the patterns need to fulfill the normalization conditions (41) with $p = v$ and $q = h$ while performing the integration over the θ, ϕ coordinates of the MBS. Because of the finite grid resolution it is again possible that the integrals in (41) are not exactly 1. One way to deal with it is to divide the amplitudes f_{vv} and f_{vh} by the $\sqrt{}$ of the value for the integral (41), which ensures automatically that the patterns are correctly normalized.

Figure 13 shows that the peak of the cross-pol pattern occurs off boresight. The cross-pol peak suppressed from the co-pol peak by about 28 dB, which means that cross polarization contamination is very small.

7.7 Transformation between Earth Brightness Temperatures and Antenna Temperatures

We are now ready to write down the full transformation from the modified Stokes vector of brightness temperatures that are emitted at the Earth surface into the modified Stokes vector that is measured by the feeds. In the following, we assume the antenna pattern Γ is given in the *MBS* and θ, ϕ denote the spherical polar coordinates of the *MBS*.

7.7.1 Faraday Rotation

The polarization vector of an electromagnetic wave of frequency ν in the microwave range that propagates from the Earth to the S/C through the geomagnetic field and the Earth's ionosphere undergoes a rotation (Faraday rotation) by the angle φ_F [7;8]:

$$\varphi_F(\theta, \phi) = \frac{135}{\nu^2} \int n_e \mathbf{B}_{geo} \cdot d\mathbf{s} \quad (92)$$

n_e is the free ionospheric electron density, \mathbf{B}_{geo} is the geomagnetic field vector, $\mathbf{k} = \mathbf{k}(\theta, \phi)$ is the unit vector in the propagation direction (from equation (82)) and $d\mathbf{s}$ is the vector line element in the direction of propagation. The units in equation (92) are: $[\nu] = Hz$, $[\mathbf{B}_{geo}] = Gauss$, $[n_e] = m^{-3}$ and $[ds] = m$. When looking into the propagation direction \mathbf{k} of the electromagnetic wave, the electric field polarization vector rotates clockwise if $\varphi_F > 0$, that is, if the geomagnetic field is pointing along the direction of

propagation. The rotation for the rotation of the electric field with components $\mathbf{E} = \begin{pmatrix} E_v \\ E_h \end{pmatrix}$

is therefore:

$$\begin{pmatrix} E_v \\ E_h \end{pmatrix}_F = \begin{pmatrix} \cos(\varphi_F) & -\sin(\varphi_F) \\ +\sin(\varphi_F) & \cos(\varphi_F) \end{pmatrix} \cdot \begin{pmatrix} E_v \\ E_h \end{pmatrix} = r[-\varphi_F] \cdot \begin{pmatrix} E_v \\ E_h \end{pmatrix} \quad (93)$$

where we have used the definition of the rotation matrix $r[\dots]$ from equation (66). Note that the Faraday rotation is an active rotation of the electric field vector rather than a passive rotation of the polarization basis vector (66), though the mathematical form is the same in both cases.

According to (92) the magnitude of the Faraday rotation angle grows with $1/\nu^2$. Because the rotation effect on v-pol and h-pol brightness temperatures is proportional to $\cos^2(\varphi_F)$ (equations (72) + (73)) it is already very small at 10.7 GHz and therefore we can neglect Faraday rotation for the GMI antenna pattern correction.

7.7.2 Polarization Basis at Boresight

Boresight is the direction $\theta_{bore}, \phi_{bore}$ at which the co-pol antenna pattern $|f_{pp}(\theta, \phi)|$ peaks. The boresight v-h polarization basis is:

$$\boldsymbol{\varepsilon}_{h,bore} = \frac{\mathbf{k}_{bore} \times (-\mathbf{e}_3)}{|\mathbf{k}_{bore} \times (-\mathbf{e}_3)|} \quad \boldsymbol{\varepsilon}_{v,bore} = \boldsymbol{\varepsilon}_{h,bore} \times \mathbf{k}_{bore} \quad (94)$$

The basis transformation from $\boldsymbol{\varepsilon}_{v(\theta,\phi)}, \boldsymbol{\varepsilon}_{h(\theta,\phi)}$ to $\boldsymbol{\varepsilon}_{v,bore}, \boldsymbol{\varepsilon}_{h,bore}$ is done by the rotation matrix:

$$r[\psi] = \begin{pmatrix} \cos(\psi) & \sin(\psi) \\ -\sin(\psi) & \cos(\psi) \end{pmatrix} = \begin{pmatrix} (\boldsymbol{\varepsilon}_{v,bore} \cdot \boldsymbol{\varepsilon}_v(\theta,\phi)) & (\boldsymbol{\varepsilon}_{v,bore} \cdot \boldsymbol{\varepsilon}_h(\theta,\phi)) \\ (\boldsymbol{\varepsilon}_{h,bore} \cdot \boldsymbol{\varepsilon}_v(\theta,\phi)) & (\boldsymbol{\varepsilon}_{h,bore} \cdot \boldsymbol{\varepsilon}_h(\theta,\phi)) \end{pmatrix} \quad (95)$$

The rotation angle $\psi = \psi(\theta, \phi)$ depends on θ, ϕ .

7.7.3 Polarization Rotation due to Deviation of the S/C Attitude from the Nominal Attitude

If the actual flight coordinate system (F) does not coincide with the nominal (nadir pointing) system due to S/C attitude variation (Appendix A.5), then that actual v-h polarization basis of (F) at boresight is:

$$\boldsymbol{\varepsilon}'_{h,bore} = \frac{\mathbf{k}_{bore} \times (-\mathbf{e}'_3)}{|\mathbf{k}_{bore} \times (-\mathbf{e}'_3)|} \quad \boldsymbol{\varepsilon}'_{v,bore} = \boldsymbol{\varepsilon}'_{h,bore} \times \mathbf{k}_{bore} \quad (96)$$

where the S/C z-axis \mathbf{e}'_3 is defined in Appendix A.5. This leads to an additional basis rotation by an angle β_{att} , that can be calculated from (66) and (173) if the S/C attitude (roll, pitch and yaw) is known.

7.7.4 Full Transformation from Brightness Temperatures into Antenna Temperatures

Putting all the active and passive rotations together, we can write down the transformation between the brightness temperature that is emitted from direction θ, ϕ and the antenna temperature that is received at ports $p = v, bore$ and $q = h, bore$ by the feeds:

$$\begin{pmatrix} T_{A,v,bore} \\ T_{A,h,bore} \\ T_{A,S3} \\ T_{A,S4} \end{pmatrix} = \int d\Omega \Gamma(\theta, \phi) \cdot R[\beta_{att}] \cdot R[\psi(\theta, \phi)] \cdot R[-\varphi_F(\theta, \phi)] \cdot \begin{pmatrix} T_{B,v(\theta,\phi)}(\theta, \phi) \\ T_{B,h(\theta,\phi)}(\theta, \phi) \\ T_{B,S3}(\theta, \phi) \\ T_{B,S4}(\theta, \phi) \end{pmatrix} \quad (97)$$

For our special case: $\beta_{att} = \varphi_F(\theta, \phi) \equiv 0$.

8 Orbit Simulator

8.1 Purpose and Overview

The orbit simulator is the key element for the algorithm verification and derivation of the error budget. Its basic element is the simulation of TOA TBs for a wide range of typical conditions under which the GMI instruments will be operating. Those simulated TOA TBs constitute the exact measurements which the calibration algorithm tries to recover.

In order to do that we simulate a GMI swath using the orbital geometry and the instrument's scan geometry. We fly the GMI instrument over a wide range of environmental scenes that are obtained from a numerical weather prediction model. The main lobe TOA TBs are calculated using an accurate radiative transfer model (RTM).

As a next step we go from brightness temperatures to antenna temperatures (TAs) using the antenna pattern theory from chapter 6 together with the simulated or measured antenna patterns that are supplied by BATC. The final step is go from TAs to radiometer counts. In order to this, BATC will provide sets of thermal environments (reflector temperature, hot load temperature, receiver temperature and gain setting, noise diode physical temperature) that are encountered during typical GMI instrument operation.

The simulated sets for TOA TBs and TAs will be the basis for deriving the antenna pattern correction (APC) coefficients. These coefficients will be used by the algorithm to convert from TA back to TB (chapter 1).

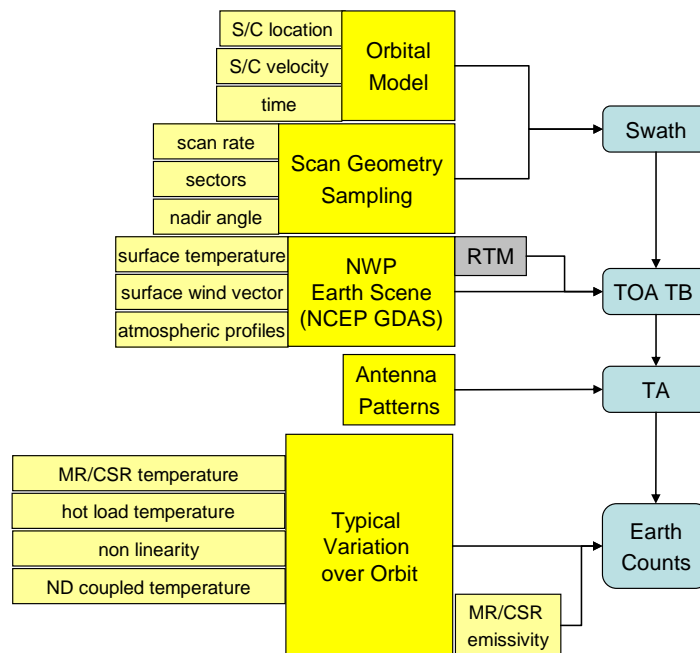


Figure 14: Schematic overview of the orbit simulator.

In this chapter we focus exclusively on the simulation of TOA TBs, TA, and radiometer counts without including any additional error sources. Figure 14 shows a schematic diagram of the steps and inputs for the orbit simulator.

8.2 S/C Orbit Simulation

We model the GMI orbit as an unperturbed, spherical orbit around the Earth center with radius $R_{S/C} = 6776.14$ km and inclination of $i = 65^\circ$. The spherical assumption is justified as the nominal average eccentricity is 0.0001 and the maximum eccentricity is 0.0005.

The gravitational force between Earth and S/C is:

$$\mathbf{F} = -\frac{GM_E m_{S/C} \mathbf{R}_{S/C}}{R_{S/C}^3} \quad (98)$$

$$GM_E = 398600.4405 \text{ km}^3 \text{ s}^{-2}$$

$\mathbf{R}_{S/C}$ is the S/C location vector, $\mathbf{V}_{S/C} = \frac{d}{dt} \mathbf{R}_{S/C}$ is the S/C velocity vector and

$\mathbf{L}_0 = \frac{\mathbf{R}_{S/C} \times \mathbf{V}_{S/C}}{|\mathbf{R}_{S/C} \times \mathbf{V}_{S/C}|}$ is the orbit normal vector pointing into the direction of the S/C angular

momentum. We neglect all other forces, such as drag forces or gravitational forces from the sun and other celestial objects to the S/C.

The orbital period $T_{S/C}$ and angular velocity $\omega_{S/C} = \frac{2\pi}{T_{S/C}}$ of the satellite are determined

from the radial equation of motion:

$$m_{S/C} \omega_{S/C}^2 R_{S/C} = \frac{m_{S/C} GM_E}{R_{S/C}^2} \quad (99)$$

which gives:

$$\omega_{S/C} = \sqrt{\frac{GM_E}{R_{S/C}^3}} \quad T_{S/C} = \frac{2\pi R_{S/C}^{3/2}}{\sqrt{GM_E}} \quad (100)$$

t_0 is the time of the ascending equatorial crossing measured since 12Z on 01 JAN 2000, and α is right ascension of the ascending node, which is the angle between the vernal equinox and the ascending equatorial crossing. α is directly related to the longitude λ_0 of the ascending equatorial crossing by equation (170) (Appendix A.4). If the orbit had an eccentricity, then there would be one more parameter necessary to determine the orbit, which the angle of perigee (measured from the direction of the ascending node to the direction of perigee), but for a circular orbit this is obsolete. We assume that the perigee is aligned with the ascending equatorial crossing.

The time t_0 and longitude λ_0 of the ascending equatorial crossing, respectively, are parameters of the orbit simulator and can be varied arbitrarily. That means that we can fly the orbit at any arbitrary start time and have it starting at any arbitrary location.

Given all these orbital parameters the vectors $\mathbf{R}_{S/C}$ and $\mathbf{V}_{S/C}$ can be easily written down in the Gaussian orbital frame (Appendix A.3). Using the transformation procedure be-

tween Gauss and *ECI* system from Appendix A.4 we can transform it first into the *ECI* system and successively also determine the geodetic S/C coordinates (Appendix A.2).

We want to note that for the purpose of the orbit simulation we are neglecting the precession and nutation of the Earth axis and therefore the *ECI* systems at different dates are the identical.

We also want to mention that our simple assumption of an unperturbed Keplerian orbit means that the orbital plane will not change. That is certainly a good approximation if one considers just one single orbit, but in reality the normal vector of the GMI orbit is precessing around the Earth axis. We expect that GSFC will provide ephemeris S/C coordinates based on the calculation of GMI orbits from the Flight Dynamics Facility.

8.3 Swath Simulation

For the swath simulation, we assume that the instruments scans counterclockwise from -70° (right of forward) to $+70^\circ$ (left of forward) in time steps of:

$$\tau_{int} = 3.6ms = 1.875s \frac{140^\circ}{360^\circ} \frac{1}{202} \quad (101)$$

The boresight azimuth angle ω at cell position $m = 0, \dots, 202$ is:

$$\omega_m = -70^\circ + m \cdot \tau_{int} \cdot \frac{360^\circ}{1.875s} \quad (102)$$

We also assume that the S/C flies plumb. That means that the axes of the in flight S/C system $F \mathbf{e}'_i, i = 1, 2, 3$ (Appendix A.5) are aligned with the nominal geodetic axes $\mathbf{e}_i, i = 1, 2, 3$ (Appendix A.2) and geodetic roll, pitch and yaw vanish.

Given ω_m and the nadir angle θ_N we can determine the boresight location using the geolocation procedure that is explained in detailed in Appendix B . This completes the simulation of an GMI swath over the S/C ground track. Figure 15 shows a typical example.

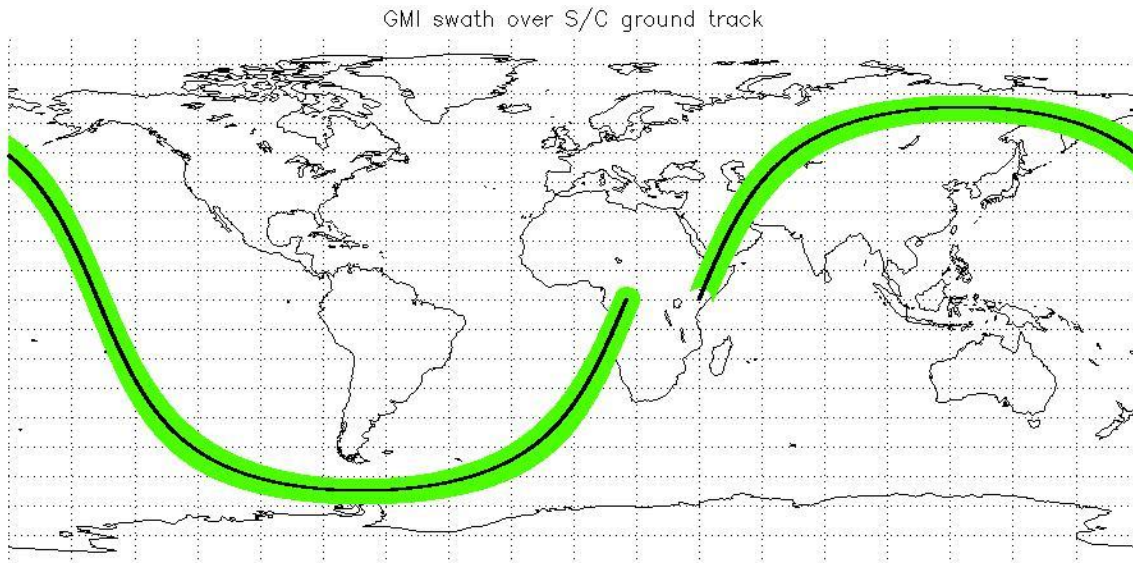


Figure 15: GMI swath (green) over S/C ground track. The longitude of the ascending equatorial crossing is 40° E.

8.4 TOA Brightness Temperature Simulation

The environmental scenes are taken from a numerical weather forecast model. We use the National Center of Environmental Prediction (NCEP) General Data Assimilation System (GDAS). It is provided every 6 hours on a 1deg by 1deg (latitude – longitude) grid. The fields we need are:

1. Surface temperature.
2. Surface wind speed and direction.
3. Vertical atmospheric profiles for pressure, temperature, water vapor density and liquid cloud water density.

The NCEP fields are tri-linearly interpolated to the time and location (latitude and longitude) of the boresight location. For sea surface salinity we use the climatology from the World Ocean Atlas (WOA98, N.O.D.C, CD-ROM). Over land the surface emissivity is set to a constant value of 0.85 for all GMI channels. TOA TBs are calculated from our radiative transfer model (RTM), which is explained in section 8.5.

Figure 16 and Figure 17 show the TOA TB of the swath of Figure 15 for the 10.65 GHz and 36.64 GHz h-pol channels, respectively.

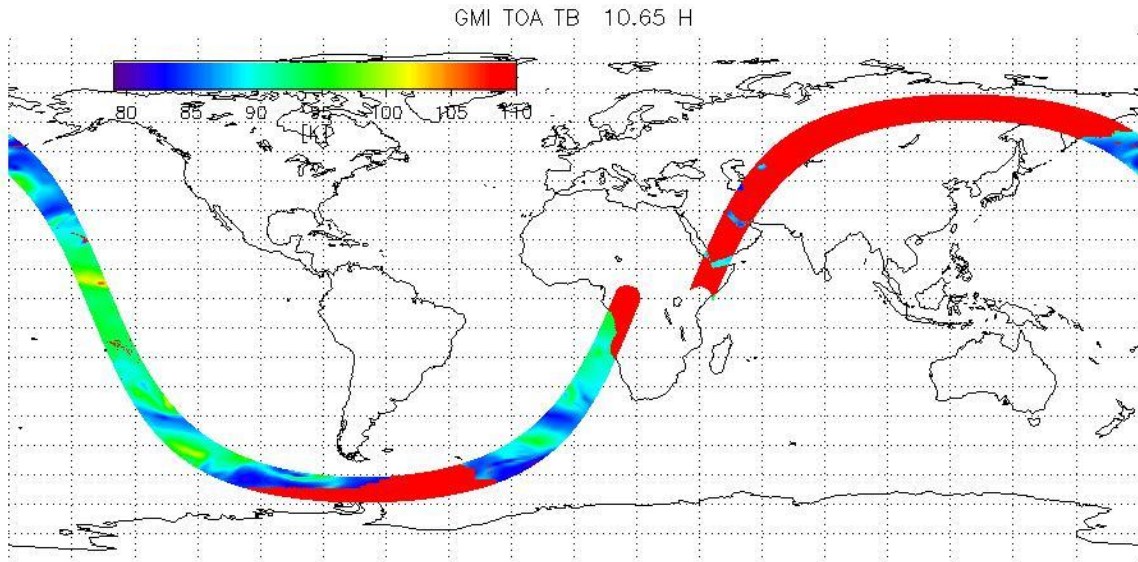


Figure 16: TOA TB simulation for the 10.65 GHz h-pol channel using the swath of Figure 15.

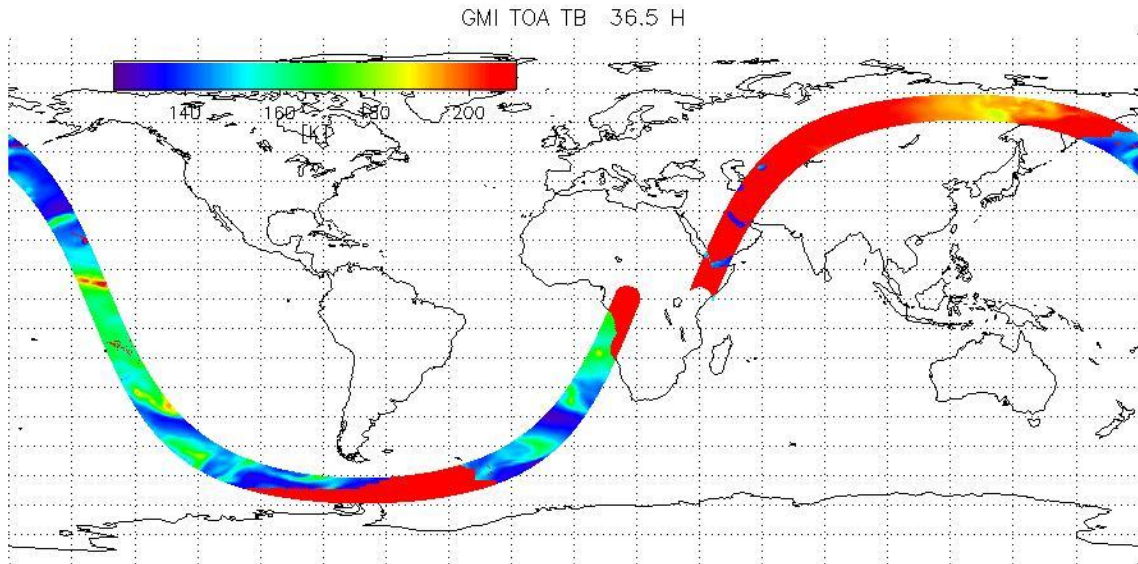


Figure 17: TOA TB simulation for the 36.64 GHz h-pol channel using the swath of Figure 15.

8.5 Radiative Transfer Model

The brightness temperature T_B that is received by the satellite radiometer consists of 3 parts:

1. The radiation that is emitted by the ocean surface and travels upward through the Earth's atmosphere.
2. The atmospheric radiation plus cold space radiation that travels downward and is scattered back from the ocean surface.
3. The upward traveling atmospheric radiation.

The microwave radiation is attenuated while traveling through the Earth's atmosphere. In the absence of rain, the atmospheric absorption and emission in the frequency range of interest are basically governed by 3 physical processes:

1. Oxygen absorption consisting of a set of rotational lines near 60 GHz and an isolated line at 118.8 GHz [9;10]. This process is characterized by the vertical atmospheric profile for air pressure $p(z)$ and temperature $T(z)$. The variable z denotes the distance along some specified path through the atmosphere from the surface 0 to the satellite location S .
2. Water vapor absorption consisting of rotational lines at 22.2 GHz, 183.3 GHz and several lines in the submillimeter wave region (above 300 GHz). This process can be characterized by the atmospheric water vapor density profile: $\rho_v(z)$. We use the absorption model of Rosenkranz [11].

We have found it necessary to make some adjustments in the atmospheric absorption models in order to match the observed and calculated TB using WindSat, AMSR-E and SSM/I measurements. The most noticeable are changing the strengths of the foreign and self-broadened H_2O continua which is consistent with the findings in [12]. We have also adjusted the temperature coefficient of the non-resonant O_2 continuum based on observations with the WindSat 6.8 and 10.7 GHz channels, where this contribution becomes dominant.

3. Rayleigh absorption by cloud water droplets, whose radii are small compared with the radiation wavelength. This process can be characterized by the atmospheric liquid cloud water density profile $\rho_L(z)$ and the dielectric constant of pure water [13]. For all of our RTM calculations we will use only rain free atmospheres where the size of the cloud water droplets are small enough so that the Rayleigh approximation is applicable.

The TOA TB is given by [14]:

$$T_B = T_{BU} + \tau ET_S + \tau R(1 + \Omega)(T_{BD} + \tau T_c) - \tau R \Omega T_c \quad (103)$$

The T_{BU} and T_{BD} are the up- and downwelling atmospheric brightness temperatures and are given by the atmospheric integrals:

$$T_{BU} = \int_0^S dz \alpha(z) T(z) \tau(z, S) \quad (104)$$

$$T_{BD} = \int_0^S dz \alpha(z) T(z) \tau(0, z)$$

Hereby $\alpha(z)$ is the total atmospheric absorption coefficient and $T(z)$ is the atmospheric temperature at location z . S denotes z -value at the TOA.

The atmospheric transmittance between z_1 and z_2 is:

$$\tau(z_1, z_2) = \exp\left(-\int_{z_1}^{z_2} dz \alpha(z)\right) \quad (105)$$

Our RTM is 1-dimensional. That means we assume that all the atmospheric profiles depend only on the altitude h above ground and are constant over the horizontal area through which the electromagnetic wave passes. The integrals over z in (104) and (105) can then simply transformed into integral over h using the relation:

$$(h + R_E)^2 = z^2 + R_E^2 + 2R_E z \cos(\theta) \quad (106)$$

where R_E is the Earth radius assuming a spherical Earth and θ is the angle between the propagation direction of the wave and the surface normal, i.e. the Earth incidence angle.

The 2nd term in (103) represents the radiation that is emitted by the ocean surface and attenuated by the Earth's atmosphere. $\tau \equiv \tau(0, S)$ is the total atmospheric transmittance.

The term $\tau R T_{BD}$ represents the downwelling atmospheric radiation that is reflected by the ocean surface and is transmitted back through the atmosphere to the satellite. The term τT_c adds the small contribution due to the cold space temperature T_c , which is transmitted through the whole atmosphere before it is reflected at the ocean surface. The surface reflectivity R is related to the surface emissivity E by Kirchhoff's law:

$$R = 1 - E \quad (107)$$

Over land we use a constant value of $E = 0.85$ for the surface emissivity for all GMI channels. Over ocean the surface emissivity has 3 components:

$$E = E_0(T_S, s) + \Delta E_{iso}(W, T) + \Delta E_{dir}(W, \varphi_r) \quad (108)$$

T_s is the sea surface temperature (SST). s is the ocean salinity. W is the sea surface wind speed (10m above ground) and φ_r the surface wind direction relative to the azimuth look direction. All terms depend also on incidence angle, frequency and polarization. The three terms in (108) are:

1. $E_0(T_s, s)$ is the specular sea surface emissivity. It is determined from the dielectric constant of sea water [13] by the Fresnel equations. It is the largest part of the sea surface emissivity.
2. $\Delta E_{iso}(W, T_s)$ is the isotropic (direction independent) part of the wind induced sea surface emissivity. When the ocean surface becomes rough, the emission increases and becomes less polarized (except at incidence angles above 55° for which the vertical polarized emission decreases). There are three mechanisms that are responsible for this variation in the emissivity, all three of them depending mainly on the ocean surface wind speed. First, surface waves with wavelengths that are long compared to the radiation wavelength mix the horizontal and vertical polarization states and change the local incidence angle. This phenomenon can be modeled as a collection of tilted facets, each acting as an independent specular surface [15] (geometric optics model). The second roughness effect is the diffraction of microwaves by surface waves that are small compared to the radiation wavelength. The third mechanism is sea foam. The mixture of air and water increases the emissivity of both polarizations. This effect is dominant for wind speeds above 7 m/s. There exist small scale ocean surface roughness models and models for ocean foam coverage and foam emission, which try to model the second and third mechanism. However, we have found that those models are not accurate enough for our purposes. Therefore we have obtained it phenomenologically from extensive studies that use satellite measured brightness temperatures and wind speeds from *in situ* observations (buoys) or numerical weather forecast models (NCEP). Our most recent study uses WindSat measurements [16;17]. The size of this term depends on wind speed, frequency, incidence angle and, to a small extent also on SST.
3. $\Delta E(W, \varphi_r)$ is the wind direction signal of the wind induced sea surface emissivity. It arises due to anisotropy of the sea surface. It is only a few Kelvin, which is very small compared to the two other terms. It can be written as a harmonic Fourier series [18]:

$$\Delta E_{dir}(W, \varphi_r) = \begin{cases} A_1 \cos(\varphi_r) + A_2 \cos(2\varphi_r) + \dots & \text{for v-pol and h-pol} \\ B_1 \sin(\varphi_r) + B_2 \sin(2\varphi_r) + \dots & \text{for 3rd and 4th Stokes} \end{cases} \quad (109)$$

Similar as for the isotropic part we derive it from phenomenological observations rather than modeling it. In [19] we have calculated it for v and h pol based on collocated SSM/I, TMI and buoy measurements. The results are consistent with our most recent analysis [16;17], which uses WindSat observations and calculates the signal for all 4 Stokes parameters.

The correction term proportional to Ω in (103) accounts for the increase of the reflected radiation due to surface scattering as compared with simple specular reflection [14]. If there is no wind ($W = 0$) and the sea surface is smooth, then $\Omega = 0$. At a wind speed of 7 m/s typical values for Ω range from 0.04 at 7 GHz v-pol to 0.05 at 37 GHz v-pol and from 0.07 at 7 GHz h-pol to 0.15 at 37 GHz h-pol. We calculate this term in the geometric optics approximation based on a statistical collection of titled facets whose slopes are distributed according to the Cox-Munk form [20].

We have validated our RTM based on comparisons between satellite measured and RTM calculated brightness temperatures. For our most recent study we use WindSat brightness temperature measurements that have been collocated within a 1 hour time window to SSM/I measurements for columnar water vapor and liquid cloud water. For SST we take the Reynolds optimum interpolated (OI) product [21]. Wind speed and direction as well as atmospheric profiles for pressure, temperature, water vapor density and liquid cloud water density are obtained from NCEP GDAS. The profiles for water vapor density and liquid cloud water density are scaled so that the columnar integrals match the SSM/I values. After correcting for spatial and temporal sampling mismatch within the collocated data set we have validated that the accuracy of our RTM for rain free atmospheres is about 0.2 Kelvin for frequencies up to 37 GHz. For details see section 12.6.

8.6 Antenna Temperature Simulation

The transformation from TOA TB into TA is described in detail in chapter 6. The antenna pattern integration is performed over the whole 4π solid angle, which covers the whole range of the polar θ and azimuthal ϕ coordinates of the *MBS*. An arbitrary vector \mathbf{b} that points from the S/C to the far field antenna pattern point can be written in the *MBS* as:

$$\mathbf{b} = \cos(\phi)\sin(\theta)\mathbf{f}_1 + \sin(\phi)\sin(\theta)\mathbf{f}_2 + \cos(\theta)\mathbf{f}_3 \quad (110)$$

Using the transformation procedures described in Appendix A we can transform \mathbf{b} in the S/C in flight system F and the *ECI* system. The procedure for locating the intersection between \mathbf{b} and the Earth surface is the same as obtaining the boresight location from Appendix B. If the argument of the $\sqrt{\quad}$ term in (192) of Appendix B is negative, then no intersection between \mathbf{b} and the Earth surface exists. In this case we assume that the brightness temperature is the effective cold space temperature T_c (Appendix D, i.e. in (97):

$$\begin{pmatrix} T_{B,v}(\theta, \phi) \\ T_{B,h}(\theta, \phi) \\ T_{B,3}(\theta, \phi) \\ T_{B,4}(\theta, \phi) \end{pmatrix} = \begin{pmatrix} T_c \\ T_c \\ 0 \\ 0 \end{pmatrix} \quad (111)$$

If \mathbf{b} intersects the Earth surface we calculate the $T_{B,i}, i = v, h, 3, 4$ the same way as we have described in section 8.4 for the boresight TOA TB using our RTM (section 8.5) but we take the NCEP GDAS environmental scene of the point where \mathbf{b} intersects the Earth. This completes the simulation of antenna temperatures T_A if the main reflector is not emissive.

8.7 Radiometer Count Simulation

Using the instrument characteristics input from Table 5 and (13) we can convert the antenna temperature T_A into radiometer Earth counts.

9 Antenna Pattern Correction

9.1 Purpose and General Method

The purpose of the antenna pattern correction is to derive the main lobe TOA brightness temperatures T_B from the measured antenna temperatures T_A for all GMI channels.

We first consider the case of dual polarization (v and h-pol) measurements at a given frequency. This applies to the 10.65, 18.7, 36.5, 89.0 and 166 GHz channels. We also assume, for the moment, that the main reflector is completely reflective and has no emissivity: $E_{refl} \equiv 0$. The transformation from T_A to T_B cannot be done exactly, as it is not possible to find a simple inversion of equation (97). However, from experience with other radiometers, we know that the relation between T_A and T_B can be very accurately approximated by the two simple linear transformations:

$$\begin{pmatrix} \tilde{T}_{A,v} \\ \tilde{T}_{A,h} \end{pmatrix} = \mathbf{A} \cdot \begin{pmatrix} T_{B,v} \\ T_{B,h} \end{pmatrix} = \begin{pmatrix} 1 - a_{vh} & a_{vh} \\ a_{hv} & 1 - a_{hv} \end{pmatrix} \cdot \begin{pmatrix} T_{B,v} \\ T_{B,h} \end{pmatrix} \quad (112)$$

and

$$\begin{aligned} T_{A,v} &= \eta_v \tilde{T}_{A,v} + (1 - \eta_v) T_c \\ T_{A,h} &= \eta_h \tilde{T}_{A,h} + (1 - \eta_h) T_c \end{aligned} \quad (113)$$

The coefficients a_{pq} , $p, q = v, h$ are the cross polarization contamination coefficients and η_p , $p = v, h$ are the spillover factors.

If there is symmetry in the antenna ports (c.f. equations (78)), then:

$$\begin{aligned} \eta_v &= \eta_h \\ a_{vh} &= a_{hv} \end{aligned} \quad (114)$$

If the a_{pq} and η_p for this frequency are known, we can then simply invert the linear transformations (113) and (112) taking us from T_A back to T_B :

$$\begin{aligned} \tilde{T}_{A,v} &= \frac{T_{A,v} - (1 - \eta_v) T_c}{\eta_v} \approx \frac{T_{A,v}}{\eta_v} \\ \tilde{T}_{A,h} &= \frac{T_{A,h} - (1 - \eta_h) T_c}{\eta_h} \approx \frac{T_{A,h}}{\eta_h} \end{aligned} \quad (115)$$

and

$$\begin{aligned}
\begin{pmatrix} T_{B,v} \\ T_{B,h} \end{pmatrix} &= \mathbf{A}^{-1} \cdot \begin{pmatrix} \tilde{T}_{A,v} \\ \tilde{T}_{A,h} \end{pmatrix} = \begin{pmatrix} 1-a_{vh} & a_{vh} \\ a_{hv} & 1-a_{hv} \end{pmatrix}^{-1} \cdot \begin{pmatrix} \tilde{T}_{A,v} \\ \tilde{T}_{A,h} \end{pmatrix} \\
&= \frac{1}{\det(\mathbf{A})} \begin{pmatrix} 1-a_{hv} & -a_{hv} \\ -a_{vh} & 1-a_{vh} \end{pmatrix} \cdot \begin{pmatrix} \tilde{T}_{A,v} \\ \tilde{T}_{A,h} \end{pmatrix} \\
&\approx \begin{pmatrix} 1+a_{vh} & -a_{hv} \\ -a_{vh} & 1+a_{hv} \end{pmatrix} \cdot \begin{pmatrix} \tilde{T}_{A,v} \\ \tilde{T}_{A,h} \end{pmatrix} \\
\det(\mathbf{A}) &= (1-a_{vh})(1-a_{hv}) - a_{vh} \cdot a_{hv}
\end{aligned} \tag{116}$$

For the approximations \approx we have assumed that $\eta_p \approx 1, a_{pq} \ll 1$ and therefore we can neglect 2nd order terms in a_{pq} and $1-\eta_p$.

9.2 Antenna Pattern Correction for Emissive Main Reflector

In general, if the main reflector has a small but finite emissivity E_{refl} and is at physical temperature T_{refl} , then an incident radiation with antenna temperature $T_{A,1}$ is changed after the reflection into $T_{A,2}$, where:

$$T_{A,2} = (1 - E_{refl}) \cdot T_{A,1} + E_{refl} \cdot T_{refl} = T_{A,1} + E_{refl} \cdot (T_{refl} - T_{A,1}) \tag{117}$$

When doing the antenna pattern correction, we assume that all of the radiation coming from cold space (spillover) is entering directly into the feedhorns without getting reflected at the main antenna. This is fulfilled to a very good approximation. The full linearized transformation between TOA TB T_B and antenna temperature T_A that is entering the feeds with an emissive antenna reads then instead of (112) and (113):

$$\begin{aligned}
\begin{pmatrix} \tilde{T}_{A,v} \\ \tilde{T}_{A,h} \end{pmatrix} &= \mathbf{A} \cdot \begin{pmatrix} T_{B,v} \\ T_{B,h} \end{pmatrix} = \begin{pmatrix} 1-a_{vh} & a_{vh} \\ a_{hv} & 1-a_{hv} \end{pmatrix} \cdot \begin{pmatrix} T_{B,v} \\ T_{B,h} \end{pmatrix} \\
\tilde{\tilde{T}}_{A,p} &= \tilde{T}_{A,p} \cdot (1 - E_{refl,p}) + E_{refl,p} \cdot T_{refl} \\
T_{A,p} &= \eta_p \cdot \tilde{\tilde{T}}_{A,p} + (1 - \eta_p) \cdot T_c
\end{aligned} \tag{118}$$

where $p = v, h$.

The antenna pattern correction then consists in the inversion of (118):

$$\begin{aligned}
\tilde{\tilde{T}}_{A,p} &= \frac{T_{A,p} - (1 - \eta_p) T_c}{\eta_p} \quad p = v, h \\
\tilde{T}_{A,p} &= \frac{\tilde{\tilde{T}}_{A,p} - E_{refl,p} \cdot T_{refl}}{(1 - E_{refl,p})} \quad p = v, h \\
\begin{pmatrix} T_{B,v} \\ T_{B,h} \end{pmatrix} &= \mathbf{A}^{-1} \cdot \begin{pmatrix} \tilde{T}_{A,v} \\ \tilde{T}_{A,h} \end{pmatrix} = \frac{1}{\det(\mathbf{A})} \begin{pmatrix} 1-a_{hv} & -a_{hv} \\ -a_{vh} & 1-a_{vh} \end{pmatrix} \cdot \begin{pmatrix} \tilde{T}_{A,v} \\ \tilde{T}_{A,h} \end{pmatrix} \\
\det(\mathbf{A}) &= (1-a_{vh})(1-a_{hv}) - a_{vh} \cdot a_{hv}
\end{aligned} \tag{119}$$

9.3 Determination of the APC Coefficients

9.3.1 Conventional Method: Antenna Pattern Integration

The method for determining the APC coefficients, that has been used so far for most microwave radiometers [22] is based on the assumption that the T_B in (97) is constant over the whole pattern as long as the boresight vector intersects the Earth surface, i.e. it does not depend on θ or ϕ . We also set the 3rd and 4th Stokes parameter in (97) to zero. Furthermore we abbreviate $\Gamma' \equiv \Gamma \cdot R[\psi]$. The v-pol component of equation (97) can then be written as:

$$T_{A,v} = \left[\int d\Omega \Gamma'_{vv}(\Omega) \right] \cdot T_{B,v} + \left[\int d\Omega \Gamma'_{vh}(\Omega) \right] \cdot T_{B,h} = \left[\int_{\text{Earth}} d\Omega \Gamma'_{vv}(\Omega) \right] T_{B,v} + \left[\int_{\text{Earth}} d\Omega \Gamma'_{vh}(\Omega) \right] T_{B,h} + \left[\int_{\text{Space}} d\Omega (\Gamma'_{vv}(\Omega) + \Gamma'_{vh}(\Omega)) \right] T_c \quad (120)$$

Comparing with (112) and (113) gives:

$$1 - \eta_v = \int_{\text{Space}} d\Omega [\Gamma'_{vv}(\Omega) + \Gamma'_{vh}(\Omega)]$$

$$\eta_v (1 - a_{vh}) = \int_{\text{Earth}} d\Omega [\Gamma'_{vv}(\Omega)] \quad (121)$$

$$\eta_v a_{vh} = \int_{\text{Earth}} d\Omega [\Gamma'_{vh}(\Omega)]$$

The normalization condition (41) implies:

$$\left[\int d\Omega (\Gamma'_{vv}(\Omega) + \Gamma'_{vh}(\Omega)) \right] = \left[\int_{\text{Earth}} d\Omega (\Gamma'_{vv}(\Omega) + \Gamma'_{vh}(\Omega)) \right] + \left[\int_{\text{Space}} d\Omega (\Gamma'_{vv}(\Omega) + \Gamma'_{vh}(\Omega)) \right] = 1 \quad (122)$$

Taking the ratio of the last 2 equations in (121) and substituting (122) into the 1st equation in (121) leads to:

$$\eta_v = \int_{\text{Earth}} d\Omega [\Gamma'_{vv}(\Omega) + \Gamma'_{vh}(\Omega)]$$

$$\frac{a_{vh}}{(1 - a_{vh})} = \frac{\int_{\text{Earth}} d\Omega [\Gamma'_{vh}(\Omega)]}{\int_{\text{Earth}} d\Omega [\Gamma'_{vv}(\Omega)]} \quad (123)$$

Analogous relations hold for the h-pol components.

We will use this method to determine the APC over land and ice surfaces. This is justified because:

1. The incidence angle and emissivity of these surface types shows little variation.
2. The brightness temperature difference between v-pol and h-pol is small.

9.3.2 Determination of the APC Coefficients from Orbit Simulator

Over the ocean, the brightness temperature difference between v-pol and h-pol is in the order of 100 Kelvin. Therefore the assumptions from section 9.3.1 are not necessarily justified and deriving the APC that way might therefore lead to biases in the retrieved TOA TB over the ocean. The more accurate determination of the APC coefficients is based on the orbit simulator (chapter 8). We run the orbit simulator over NCEP GDAS environmental scenes for several orbits on several days of the year and for several local equatorial crossing times. This can be achieved by simply varying the parameter t_0 in section 8.2. Using the NCEP environmental scenes over the whole globe will guarantee that we have a set that contains all representative meteorological and physical conditions that occur (variability of SST, wind speed, cloud, vapor etc.). It is not necessary to use every point on the swath but only a small subset (e.g. a few looking directions and every 10th scan), but still have a set that is representative for the environmental conditions that are encountered during the GMI operation.

Near coastlines and other geographical interfaces there can be considerable contamination to the main lobe scene as a result of main lobe seeing ocean where the near-sidelobes are seeing land, which has a very different brightness temperature. We do not want that the derivation of the APC is affected by these contaminations. Therefore we use only orbits whose boresight observations are far from land. If the sidelobe observation starts hitting land, the magnitude of the antenna pattern are already so far reduced that it will not have a significant contribution to the integral (97). This can be done for example by centering the swath over the Pacific and skip any observation whose boresight is closer than 100 km from land or ice. The far-sidelobes can still hit land or ice. For the purpose of carrying out the integration in (97) over the whole Earth, we assume for the far-sidelobes that the environmental scene is over water. We use surface temperature and atmospheric profile from NCEP GDAS, vary the wind speed randomly between 0 and 15 m/s and the wind direction randomly between 0 and 360 deg, set the salinity to 38 ppt, and calculate the surface emissivity as if it was sea water.

This method leaves us with a large training set of TA and TB values for each GMI channel. Finally, we fit the coefficients a_{pq} , and η_p from section 9.1 in a least-square sense by performing linear regressions.

9.4 Antenna Pattern Correction for Single Polarization Frequencies

We now briefly discuss the special case of the frequencies with only a single polarization channel (23.8 and 183 GHz). Without a second frequency to perform cross-pol correction, the correction for spillover and overall cross-pol contribution can be combined into a single linear relationship.

We can still perform the full forward calculation from the orbit-simulator as explained in section 9.3 and obtain simulated values for both polarizations of $T_{B,p}$ and $T_{A,p}$. The v-pol component of the first relation in (118) reads:

$$\tilde{T}_{A,v} = (1 - a_{vh}) \cdot T_{B,v} + a_{vh} \cdot T_{B,h} \quad (124)$$

For the 183 GHz channels and for 23.8 GHz land observations, in Equation (119) we can set $T_{B,v} \approx T_{B,h}$ and therefore also $T_{B,v} = \tilde{T}_{A,v}$.

For 23.8 GHz ocean observations we assume a constant ocean scene brightness temperature of the h-pol $T_{B,h} = \text{const}$. Then (119) becomes effectively a linear transformation between $T_{A,v}$ and $\tilde{\tilde{T}}_{A,v}$ followed by the emissivity correction,

$$\begin{aligned}\tilde{\tilde{T}}_{A,v} &= \lambda T_{A,v} + \xi, \\ \tilde{T}_{A,v} &= \frac{\tilde{\tilde{T}}_{A,v} - E_{\text{refl},v} T_{\text{refl}}}{1 - E_{\text{refl},v}}\end{aligned}\tag{125}$$

$$T_{B,v} = \tilde{T}_{A,v}$$

The coefficients λ and ξ can be found from the forward simulation of $T_{B,p}$ and $T_{A,p}$.

This method effectively eliminates any static bias error (see section 10.1) in the APC of the single polarization channels. The remaining dynamical error arises due to the dynamical variation of the ocean scene brightness temperature $T_{B,h}$.

10 Pre-Launch Verification and Testing

This chapter contains the methods that we use to verify and test the GMI calibration algorithm pre-launch and the derivation of the error budgets.

10.1 Calibration Uncertainty Errors and Error Budgeting

We assume that the calibration uncertainty includes all terms that are *static bias* errors and *dynamic* errors. The following defines the static and dynamic errors and how they are combined.

1. *Static errors* are constant *bias* terms. There are three types of these:
 - a) *Random Static Bias Errors*: Constant bias terms that have an equal likelihood of being positive or negative. These are generally static terms that are corrected, leaving only the uncertainty in the correction, which could be positive or negative.
 - b) *Positive Static Bias Errors*: Bias terms that are known before-hand to be positive. These are generally static terms that are not corrected.
 - c) *Negative Static Bias Errors*: Bias terms that are known before-hand to be negative. These are generally static terms that are not corrected.
2. *Random dynamic errors* are zero-mean errors that vary on time scales from one calibration cycle to less than the length of the mission.

Static and dynamic errors are kept separate. The handling of the various errors and booking onto the error budget is done the following way:

1. For each independent static error we assume the worst case. That means we use a thermal environment of the instrument (hot load temperature, reflector temperature, receiver temperature, ...) and an environmental scene that will give the largest error.
2. We add all worst case independent positive static bias errors.
3. We add all worst case independent negative static bias errors.
4. We root sum square (RSS) all worst case independent random static errors.
5. We RSS the positive, negative and random static bias errors to obtain a combined static bias error.
6. All independent dynamic errors will be modeled as Gaussian random derivatives [23], booked as 3-sigma values and combined in an RSS sense.
7. The combined static and combined 3σ dynamic errors will be combined in an RSS sense to yield the number for the total error, which will be compared against the performance requirements of section 3.2.
8. Errors due to calibration anomalies (chapter 11) are not included in the error budget.
9. NEDT for scene, hot counts and cold counts are booked into the NEDT budget and will not be included in the calibration error budget.

10.2 Error Sources and Verification of the Cold Calibration

To first order, the effective cold sky radiometric temperature may be expressed in the following form:

$$\left[T_c^{eff} \right]_{true} = f_c \left[R_{crefl} T_c + (1 - R_{crefl}) T_{crefl} \right] + f_E T_{A,E} + f_{inst} T_{inst} + f_{S/C} T_{S/C} + f_{strut} T_{strut} + T_{LO} \quad (126)$$

where each of the terms in equation (126) has the following meanings:

f_c : Cold sky beam fraction.

$R_{crefl} = 1 - E_{crefl}$: Reflectivity of the cold sky reflector (CSR).

E_{crefl} : Emissivity of the CSR.

T_c : Cold space temperature after accounting for the deviation from the RJ approximation (c.f. Appendix D)

T_{crefl} : Temperature of the CSR.

f_E : Beam fraction that falls on the Earth.

$T_{A,E}$: Antenna temperature coming from the Earth.

f_{inst} : Beam fraction that falls on the instrument deck.

T_{inst} : Brightness temperature of the instrument deck.

$f_{S/C}$: Beam fraction that falls on the S/C.

$T_{S/C}$: Brightness temperature of the S/C.

f_{strut} : Beam fraction that falls on the struts.

T_{strut} : Brightness temperature of the struts.

T_{LO} : Increase in the cold sky effective temperature due to leakage from the local oscillator that is reflected from the cold sky reflector into the feeds.

The cold calibration algorithm does not correct for intrusion from the instruments, S/C or strut. It corrects for emissivity of the cold sky reflector and we will derive a post-launch correction for Earth intrusion (section 11.3). The value for T_c^{eff} from the calibration algorithm is then (c.f. equation (2)):

$$\left[T_c^{eff} \right]_{calc} = (1 - f_E) \cdot R_{crefl} \cdot T_c + (1 - f_E) \cdot (1 - R_{crefl}) \cdot T_{crefl} + f_E \cdot T_{A,E} \quad (127)$$

Because of

$$f_c + f_E + f_{instr} + f_{S/C} + f_{strut} = 1 \quad (128)$$

$f_i \leq 1$, $i = E, S/C, instr, strut$, $1 - R_{crefl} \leq 1$ and $T_c \leq T_i$, $i = E, S/C, instr, strut$, the error in T_c^{eff} can be written in first order as:

$$\Delta T_c^{eff} \equiv \left[T_c^{eff} \right]_{true} - \left[T_c^{eff} \right]_{calc} \approx \sum_{i=instr, S/C, strut} f_i T_i + \Delta \left[E_{crefl} \cdot T_{crefl} \right] + \Delta \left[f_E \cdot T_{A,E} \right] \quad (129)$$

$\Delta \left[f_E \cdot T_{A,E} \right]$ is the residual error from the correction for the Earth view intrusion. It is basically due to the deviation of the Earth scene temperature from the static map that we use for doing the correction. It will be treated as a random dynamic error.

$\Delta \left[E_{crefl} \cdot T_{crefl} \right]$ is the residual error from the correction for the CSR emissivity. If the knowledge errors for E_{crefl} and T_{crefl} are uncorrelated it can be calculated as:

$$\Delta \left[E_{crefl} \cdot T_{crefl} \right]^2 = \left(T_{crefl} \cdot \Delta \left[E_{crefl} \right] \right)^2 + \left(E_{crefl} \cdot \Delta \left[T_{crefl} \right] \right)^2 \quad (130)$$

The first term arises due to the knowledge error of the reflector emissivity. It is treated as random static bias error. The second term arises due to the deviation of the true reflector physical temperature from the readings of the PRT. It is treated as dynamic random error.

The intrusions $\sum_{i=\text{instr}, S/C, \text{strut}} f_i \cdot T$ are treated as positive static bias errors, using the worst case values for the beam fractions f_i and brightness temperatures T_i of the intruding components $i = \text{instr}, S/C, \text{strut}$.

The contribution of the local oscillator leakage T_{LO} is, if left uncorrected, a random static bias error. If corrected, the residual knowledge error will be a random static bias error. BATC has provided maximal values for this error at each frequency. We assume that half of it can be corrected and book the other half as random static bias error into the error budget.

10.3 Error Sources and Verification of the Hot Calibration

To first order, the effective hot load radiometric temperature may be expressed in the following form:

$$\begin{aligned} [T_h^{eff}]_{true} = & f_h \cdot E_h \left[[T_h^{eff}]_{calc} + \Delta T_{grad} \right] + \\ & f_h \cdot (1 - E_h) T_h^{refl} + f_{shroud} \cdot E_{shroud} \cdot T_{shroud} + f_{shroud} \cdot (1 - E_{shroud}) \cdot T_{shroud}^{refl} + \\ & f_{gap} \cdot T_{gap} + f_{other} \cdot T_{other} + T_{LO} \end{aligned} \quad (131)$$

where

f_h : Beam fraction of the feed main beam to the hot load.

E_h : Emissivity of the hot load.

w_i : PRT weight.

T_i^{PRT} : PRT reading.

ΔT_{grad} : Contribution to the hot load effective temperature due to gradients within the hot load.

f_{shroud} : Beam fraction from the feeds onto the shroud surrounding the hot load.

E_{shroud} : Emissivity of the shroud.

T_{shroud} : Physical temperature of the shroud.

T_{shroud}^{refl} : Brightness temperature reflected from the shroud.

f_{gap} : Beam fraction from the gap. The *gap* is defined as the view by the feeds to cold space or anything that may have brightness temperature that is cold compared with the hot load.

T_{gap} : Brightness temperature from the gap.

f_{other} : Beam fraction from other warm sources. These include the instrument bay, hot load brim, and anything that has a brightness temperature similar to the hot load.

T_{other} : Brightness temperature from those other warm sources.

T_{LO} : Increase in the hot load effective temperature due to leakage from the local oscillator reflected of the hot load.

The hot calibration algorithm computes the effective hot load temperature as:

$$\left[T_h^{eff} \right]_{calc} = \left[w_0 + w_1 \cdot T_{PRT,ave} \right] + \left[u_0 + u_1 \cdot (T_{PRT,ray} - T_{PRT,ave}) \right] \quad (132)$$

Using

$$f_h + f_{shroud} + f_{gap} + f_{other} = 1 \quad (133)$$

the error in T_h^{eff} can be written in first order as:

$$\begin{aligned} \Delta T_h^{eff} &\equiv \left[T_h^{eff} \right]_{true} - \left[T_h^{eff} \right]_{calc} \approx \\ &\Delta T_{grad} + (1 - E_h) \cdot (T_h^{refl} - T_h^{eff}) + \\ &f_{shroud} \cdot E_{shroud} (T_{shroud} - T_h^{eff}) + f_{shroud} \cdot (T_{shroud}^{refl} - T_h^{eff}) + \\ &f_{gap} \cdot (T_{gap} - T_h^{eff}) + f_{other} \cdot (T_{other} - T_h^{eff}) + T_{OL} \end{aligned} \quad (134)$$

BATC has provided data from its thermal model which contain the effective brightness temperature of the hot load together with the PRT readings over the course of several representative orbits. The best fit for the PRT weights w_i can be found by a least square fit.

The residuum of this fit is ΔT_{grad} which is treated as a dynamic random error.

The contribution from the gap is treated as negative static bias error.

The contribution of the local oscillator leakage T_{LO} is, if left uncorrected, a random static bias error. If corrected, the residual knowledge error will be a random static bias error. BATC has provided maximal values for this error at each frequency. We assume that half of it can be corrected and book the other half as random static bias error into the error budget.

The other terms will be treated as random dynamical errors. We assume that T_h^{refl} , T_{shroud} , T_{shroud}^{refl} , T_{other} are randomly distributed around T_h^{eff} .

10.4 Error Sources and Verification of the APC

10.4.1 Error of the APC

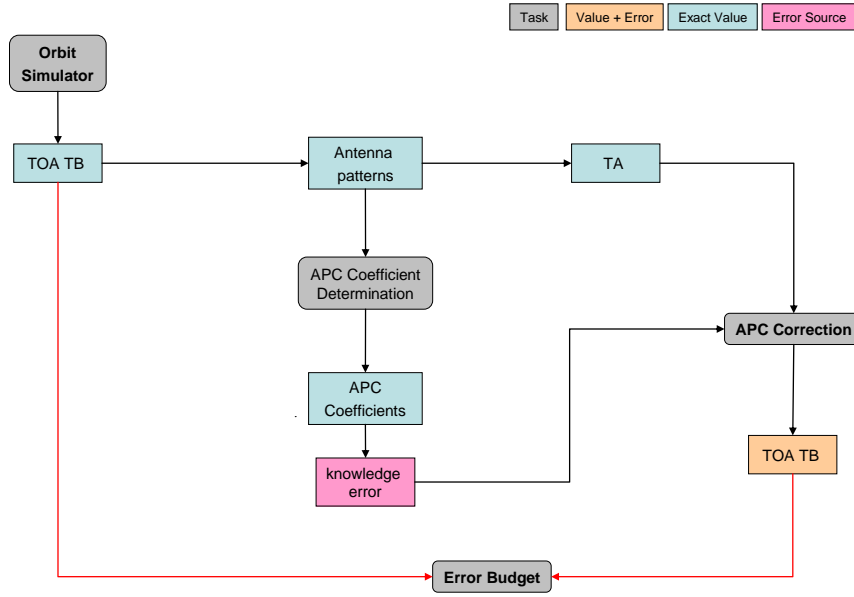


Figure 18: Pre-launch verification scheme of the APC based on the orbit simulator.

To first order, the error in the antenna temperature due to the APC has the following contributions:

$$[\Delta T_A]_{APC} = [\Delta T_A]_I + [\Delta T_A]_{AP} + \Delta \left[E_{refl} \cdot (T_{refl} - T_A) \right] + \sum_{i=inst, S/C, strut} f_i \cdot (T_i - T_A) \quad (135)$$

where

$[\Delta T_A]_I$: Contribution from sidelobes + backlobes + cross polarization.

$[\Delta T_A]_{AP}$: Error due to the antenna pattern knowledge error.

f_{inst} : Beam fraction that falls on the instrument deck.

T_{inst} : Brightness temperature of the instrument deck.

$f_{S/C}$: Beam fraction that falls on the S/C.

$T_{S/C}$: Brightness temperature of the S/C.

f_{struts} : Beam fraction that falls on the struts.

T_{struts} : Brightness temperature of the struts.

T_A : Brightness temperature of the scene.

$\Delta \left[E_{refl} \cdot (T_{refl} - T_A) \right]$: Residual error from the correction for the MR emissivity.

The basic scheme for calculating the errors $[\Delta T_A]_I$ and $[\Delta T_A]_{AP}$ are shown in Figure 18.

These error sources are now discussed in detail.

10.4.2 Contribution from Sidelobes, Backlobes and Cross Polarization

The determination of this part of the APC error uses the orbit simulator (chapter 8), but we make a further simplification about the environmental scenes. When performing the integration over the antenna patterns in (49), we will assume that the whole Earth environmental scene is identical to the boresight environmental scene (SST, wind, vapor, cloud, atmospheric profiles). The brightness temperature still varies with location because:

1. The local incidence angle varies. The major effect on the brightness temperature comes from the variation of the specular surface emissivity (section 8.5) according to the Fresnel equations.
2. The local polarization rotation angle in (47) also varies, even though the environmental scene is homogenous.

We generate a test set of TA and TB values for each GMI channel the same way as described in section 9.2.2 but with a homogeneous environmental ocean scene. We take the simulated antenna temperatures, apply the APC that was derived from the training set and compare with the main lobe TOA TB. We book the difference into the error budget for the antenna pattern correction. It contains the error from the APC from all side and backlobes and cross polarization contamination from the whole pattern. For the dual polarization channels we expect this error to be very small, because the environmental scenes are homogeneous and contains no geographical interfaces (ocean-land etc.). For the single polarization channels we cannot do a cross polarization correction but only a spillover correction in the form of (125). We therefore expect a significant error from cross polarization for the single polarization channels.

The error is treated as random dynamic error. We use whole TOA TB test set or computing this error. This corresponds to weighting the various geographical and geophysical conditions according to how likely they occur in nature.

We have also performed test runs of the APC algorithm using realistic Earth scenes that contain land contamination both in the near and the far sidelobes. To do this, the TAs are simulated according to the method described in section 8.6. If the Earth location is over land we use a constant value of 0.85 for the land emissivity. Especially for the lower frequencies where the beam fraction is small, we can expect significant errors in the retrieved TOA TBs near the cost lines. However, these errors will not be booked into the error budget. A possible way to reduce these errors is the near-sidelobe correction algorithm. The idea is to resample the individual field of view brightness temperatures for each observation cell onto the pattern of the main beam of this cell using the measurements of the surrounding cells. The basic method is outlined in Appendix C .

10.4.3 Knowledge Error in the Antenna Patterns

We expect this error to be the dominant contribution of the antenna pattern error. BATC will provide knowledge error of the antenna patterns. We use the simplified equations (121) to estimate how the error in the pattern relates to an error in the spillover η_i and the cross polarization contamination a_{ij} . We take a set of TBs from the orbit simulator over several representative orbits. We use the simplified forms (112) + (113) together with the values for a_{ij} and η_i that we have obtained from the antenna patterns without error to transform the TBs into TAs. When doing the inversion from TA to TB (116) we use the APC that contain the error. The difference between the original and retrieved TB is an

estimate for $[\Delta T_A]_{AP}$. This will be done for the whole TOA TB test set and we will book the maximum error as random static bias error.

Alternatively, we can calculate the combined error $[\Delta T_A]_i$ and $[\Delta T_A]_{AP}$ the way it is shown in Figure 18. We calculate TA from the TOA TB doing the full antenna pattern integration (97) with the exact antenna patterns. When retrieving the TOA TB from the simulated TB we take coefficients a_{ij} and η_i containing the knowledge error.

If BATC does not supply knowledge errors on the antenna patterns, we can use the requirement on this error to derive a requirement for the antenna pattern knowledge error.

10.4.4 Knowledge Error in the Main Reflector (MR) Emissivity and Temperature

$\Delta[E_{refl} \cdot (T_{refl} - T_A)]$ is the residual error from the correction for the MR emissivity. As the worst case for the scene brightness temperature T_A we assume cold space and therefore $\Delta[E_{refl} \cdot (T_{refl} - T_A)] \approx \Delta[E_{refl} \cdot T_{refl}]$. We can write:

$$\Delta[E_{refl} \cdot T_{refl}]^2 = (T_{refl} \cdot \Delta[E_{refl}])^2 + (E_{refl} \cdot \Delta[T_{refl}])^2 \quad (136)$$

assuming that the errors for R_{refl} and T_{refl} are uncorrelated. The first term (knowledge error of MR reflector emissivity) is treated as random static bias error. The second term (knowledge error of MR temperature) is treated as random dynamic error. We use the worst case values.

10.4.5 Contamination from Instrument, S/C and Strut

BATC will provide a blockage matrix which shows which part of the antenna pattern (section 7.5) is blocked by the instrument, S/C and struts. From this blockage matrix we can calculate the beam fractions f_i , $i = S/C, instr, strut$.

Each term is treated as independent random static bias error and calculated using the worst value for scene temperature T_A .

10.5 Error Sources and Verification of the Non-Linearity Correction

If the value of the ground-non linearity is used in the calibration algorithm, then the error budget for the non-linearity correction is determined by the error in that measurement.

The on-orbit retrieval and trending of the non-linearity is described in section 6.2. The error for one retrieval of T_{nl} is in principle dominated by the NEDT. However, because the trending is done for a large number of events (several 100 orbits), the NEDT and therefore its impact on the non-linearity retrieval can be kept arbitrarily small. The residual error in T_{nl} is then given by the errors in T_h^{eff} and T_c^{eff} according to equation (26):

$$\Delta T_{nl} = \frac{\Delta(T_h^{eff} - T_h^{eff})}{(T_h^{eff} - T_h^{eff})} \cdot T_{nl} \quad (137)$$

10.6 Verification of the Calibration Uncertainty

The total error for the uncertainty of the antenna temperature $\Delta^2[T_A]$ is obtained from (8) using error propagation:

$$\Delta^2[T_A] = x^2 \cdot \Delta^2[T_h^{eff}] + (1-x)^2 \cdot \Delta^2[T_c^{eff}] + 16(x-x^2)^2 \cdot \Delta^2[T_{nl}^{eff}] \quad (138)$$

$\Delta^2[T_c^{eff}]$ is the cold calibration error (section 10.2).

$\Delta^2[T_h^{eff}]$ is the hot calibration error (section 10.3).

$\Delta^2[T_{nl}^{eff}]$ is the error in the non linearity (section 10.5).

$x = \frac{C_{scene} - \bar{C}_c}{\bar{C}_h - \bar{C}_c} \approx \frac{T_{scene}}{T_h}$ can vary between 0 (cold space) to 1.36 (hot Earth surface). We

use the value of x for which (138) is maximal. In order to obtain the final value for the calibration uncertainty in the TOA TB $\Delta[T_B]$, we combine $\Delta[T_A]$ with the APC error (135) in an RSS sense.

10.7 Testing of Functional Requirements

All functional requirements from the *Algorithm Requirements and Interfaces Specification* are documented and tracked in the ATBD. The basic method of verification is inspection of the equations and their derivations in the ATBD.

In addition, we will deliver software to demonstrate the verification of some requirements. The functionality of each individual submodule will be tested before delivery with data from the orbit simulator. As explained in chapter 8, RSS will generate radiometer counts from simulated TOA TB. Testing and verification of the functional requirements of each individual submodule is done through visual inspection of the sample input and output files that accompany the code.

Finally, we will test the functionality of the whole algorithm with the submodules being linked together. For this purpose, we will generate radiometer counts from simulated TOA TB without adding any errors and set also all the NEDT are zero. In the antenna pattern integration we assume a constant brightness temperature over the whole Earth field of view, so that the antenna pattern correction can be exactly inverted. We then run the calculated radiometer counts through the whole calibration algorithm. Aside from small numerical roundoff errors, the output TOA TB of the code needs to be identical to the input TOA TB.

The verification of the flagging and removal of lunar intrusion into the CSV can be done post-launch as explained in section 11.1 by producing similar plots than Figure 19 (before flagging and correcting) and Figure 20 (after flagging and correcting).

11 Sensor and Calibration Anomalies

The basic parts of the radiometer calibration procedure have been explained in chapters 6 and 9. Applying these procedures assumes that the calibration system works perfectly. From all our experience with other instruments (SSM/I, SSMIS, TMI, AMSR, WindSat) we know that this is unfortunately not the case. Even for a well designed and constructed calibration and measurement system certain error sources, commonly referred to as anomalies, typically occur. It is an important part of the calibration procedure to analyze the impact of these error sources and find corrections for it in order to keep them on a minimal level. Those corrections will generally need to be derived from post-launch calibration as it is unknown before launch how and how much the instrument calibration will be impacted by the various error sources. Errors that arise due to calibration anomalies will in general not be booked into the error budget. This chapter gives an overview over the most important anomalies and how the GMI will try to do the appropriate corrections. The derived methods are largely based on experience with radiometer heritage.

11.1 Moon Intrusion into the Cold Sky View

The geometry of the orbit and the cold sky view lead to lunar intrusion into the cold sky view. For a polar orbiting, sun-synchronous orbit this happens about twice every month, once during the ascending and once during the descending swath. The GMI calibration algorithm uses the same technique that we have developed and applied for SSM/I, SSMIS and TMI.

Figure 19 shows a map of the scan averaged cold counts for SSMIS 37V using 1500 orbits. The x-axis corresponds to orbit number (rev #) or time (days after the first orbit). The y-axis corresponds to the intra-orbit position of the S/C (fractional rev #). The fractional rev # is 0.0 if the S/C is at its southernmost latitude, 0.25 at the ascending equatorial crossing, 0.5 at the northernmost latitude, 0.75 at the descending equatorial crossing and 1.0 again at the southernmost equatorial crossing. The moon is clearly visible as red spot in the map.

The moon intrusion occurs if the vector between the S/C and the moon $\hat{\mathbf{r}}_{moon}$ is closely aligned with the boresight vector of the cold mirror $\hat{\mathbf{r}}_{CSV}$. Typical the S/C – moon vector is given in the ECI2000 system [24] and the boresight vector of the cold mirror in the GMI coordinate system (Appendix A.5). Using the transformation procedure in Appendix A, we transform both vectors into the same coordinate system, take the scalar product and calculate the angle ξ between the 2 vectors at each scan:

$$\xi = \arccos\langle \hat{\mathbf{r}}_{moon} \cdot \hat{\mathbf{r}}_{CSV} \rangle \quad (139)$$

If $|\xi| < \xi_{crit}$ we flag the scan for moon intrusion into the cold sky view by setting bit 11 of the scan flag (Table 22). The critical value ξ_{crit} depends on frequency. If the frequency is larger, the moon intrusion spot is visible sharper in the cold count map and one can use a smaller value for ξ_{crit} . The value for ξ_{crit} is chosen large enough so that all the scans with lunar intrusion are flagged. Some small margin should be added.

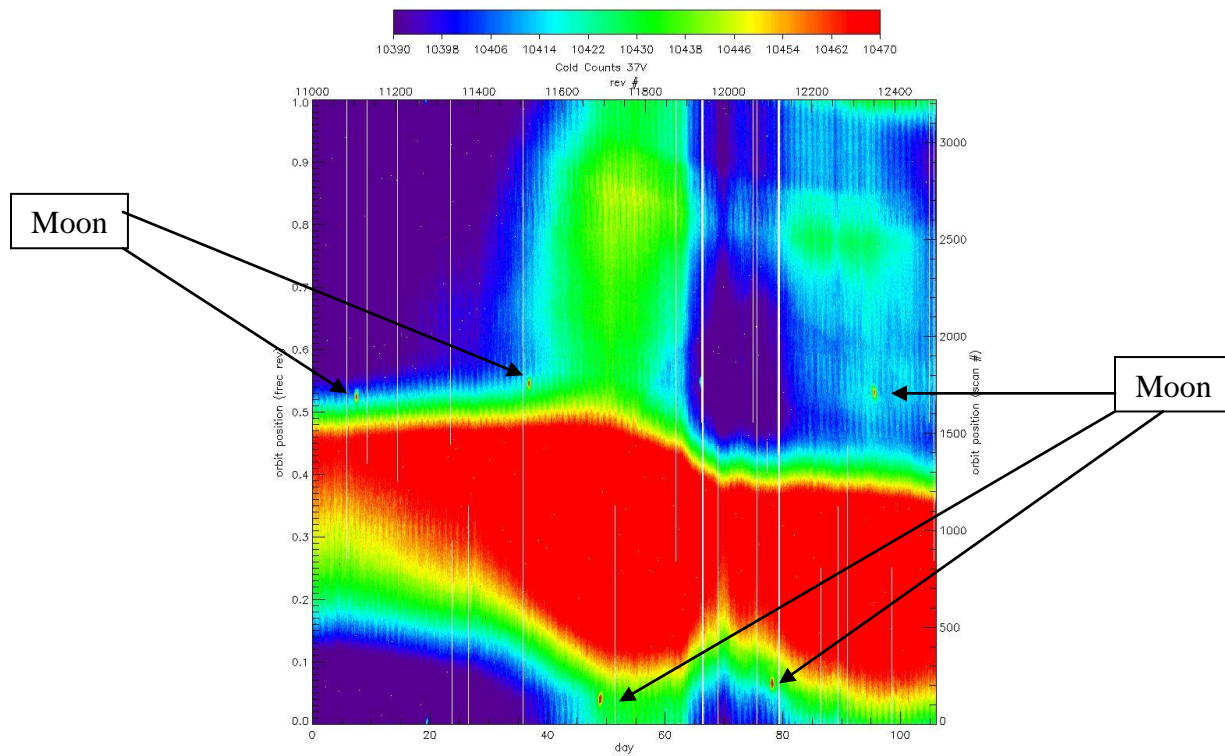


Figure 19: Cold count map for SSMIS 37V before correction of moon intrusion. The x-axis is time (orbit # or day since the starting orbit). The y-axis is the intra-orbit position (fractional rev #).

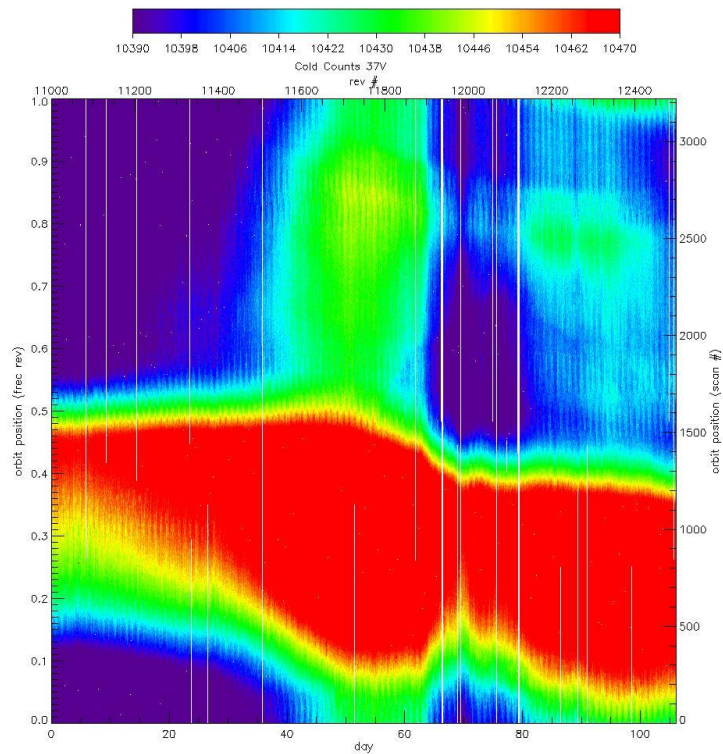


Figure 20: Cold count map for SSMIS 37V after correction of moon intrusion.

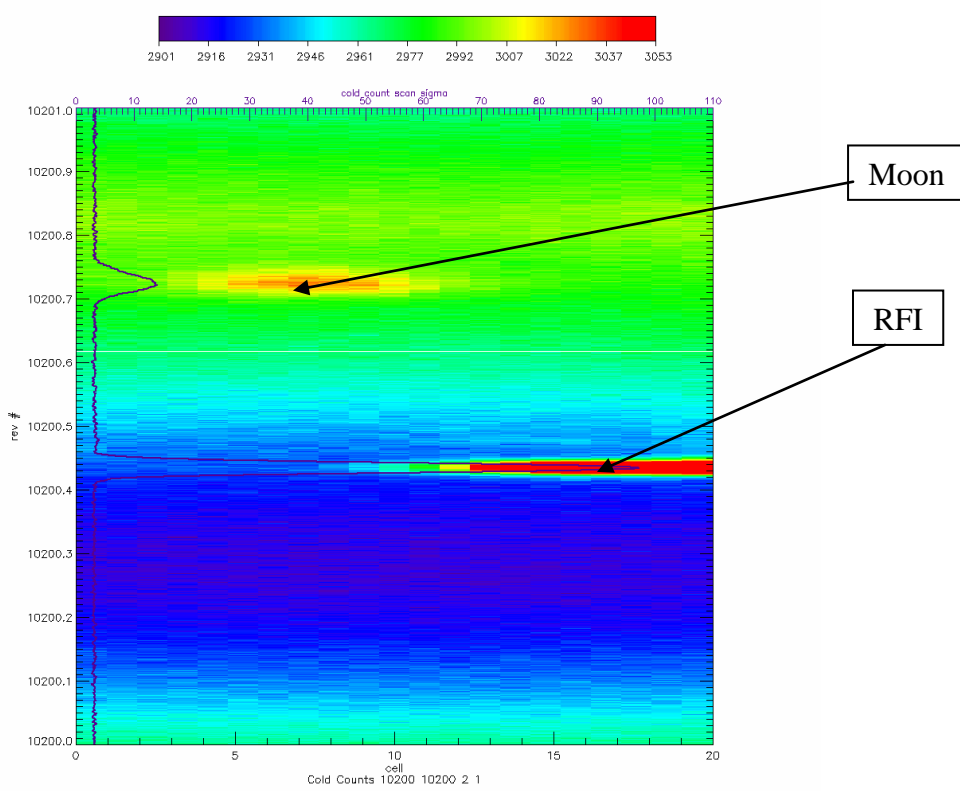


Figure 21: WindSat 10.7 GHz cold swath of orbit # 10200 showing moon and RFI intrusion.

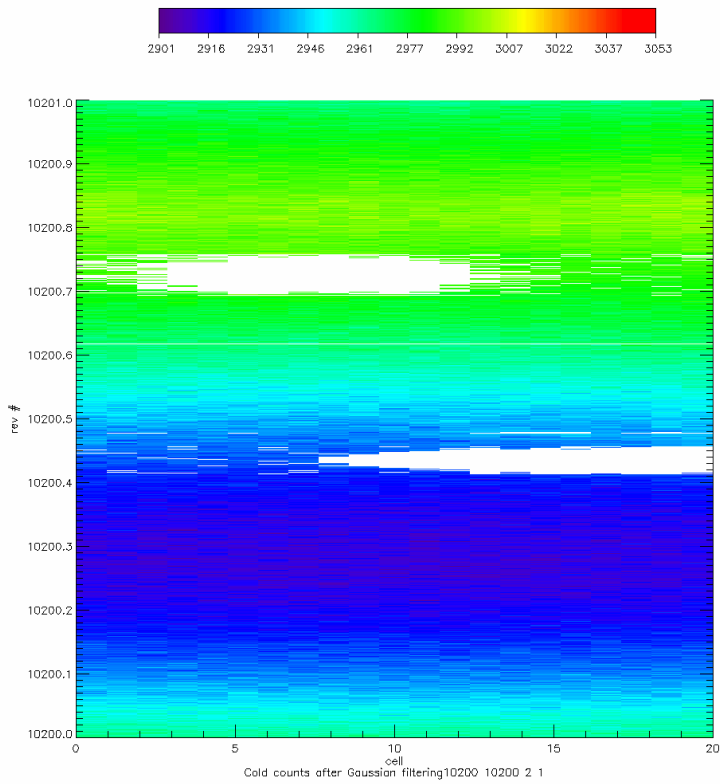


Figure 22: WindSat 10.7 GHz cold swath of orbit # 10200 after applying the statistical filter.

If scan i_{scan}^{moon} is flagged for moon intrusion, then we take the first good scan i_{scan}^0 within m scans before i_{scan}^{moon} and the first good scan i_{scan}^1 m scans after i_{scan}^{moon} . If no good observations can be found within this window, we do not perform a correction, reset bit 11 of the scan flag (Table 22) and set bit 12 instead. If we find good observation for both i_{scan}^0 and i_{scan}^1 we calculate the value for the average cold counts at i_{scan}^{moon} by linear interpolation:

$$\bar{C}_c(i_{scan}^{moon}) = \bar{C}_c(i_{scan}^0) + \frac{\bar{C}_c(i_{scan}^1) - \bar{C}_c(i_{scan}^0)}{i_{scan}^1 - i_{scan}^0} \cdot (i_{scan}^{moon} - i_{scan}^0) \quad (140)$$

This is justified as long as the cold counts do not vary too much over the $2m+1$ scans in the window.

For SSMIS and TMI we have used $m = 200$ $\xi_{crit} = 5^\circ$ for the channels with frequencies 37 GHz and higher and $\xi_{crit} = 8^\circ$ for the channels with frequencies below 37 GHz. Figure 20 shows the cold count map for SSMIS 37V after the correction has been applied. We will use the same values for the GMI algorithm as first guess, but might update them post-launch.

The verification of the flagging and correction for lunar intrusion into the cold sky view is done post-launch by running the cold calibration module first without and then with doing the correction and plot maps similar than Figure 19 and Figure 20.

11.2 RFI Intrusion into the Cold Sky View

Radio frequency interference (RFI) into the cold mirror from geostationary telecommunication satellites that fly at high altitude was observed for the WindSat 10.7 GHz channels. With 300 MHz, the bandwidth of the WindSat 10.7 GHz channels is large compared with other instruments. The GMI 10.7 GHz bandwidth is only 100 MHz and we therefore expect that it is much less prone to RFI than WindSat. However, it is unknown how many geostationary satellite at what level and at which frequencies will be broadcasting when GMI is operating. Therefore RFI intrusion into the cold mirror needs to be analyzed and if necessary corrected.

Figure 21 shows a map of the cold swath of the WindSat 10.7 GHz v-pol for orbit # 10200. The x-axis specifies the along scan position of the cold sample. WindSat has a wide cold swath with 20 cold samples. The y-axis specifies the intra-orbit position or fractional rev # as explained in section 11.1. Moon and RFI intrusion are visible as hot spots.

We have developed and implemented a statistical filter method that detects RFI intrusions and flags the cold counts. The flagging is done for the single cold count observation and those flagged observations will not be used when computing the scan averaged cold counts (equation (1) of section 4.1). The statistical filter method can also be used for flagging and correcting lunar intrusion into the cold mirror as an alternative to the method described in section 11.1. It makes use of the following properties:

1. If there is no moon or RFI intrusion, cold counts are Gaussian distributed.
2. Moon and RFI intrusion lead to a positive bias.
3. If there is moon or RFI intrusion, there is still a sufficiently large part of the surrounding swath that is not contaminated.

4. The spatial pattern within the along-scan/orbit-position cold count map is always coherent for moon or RFI intrusions. In other words, if there is one pixel in the pattern flagged for intrusion, then also the surrounding pixels within a certain window should be bad as well.

Our method first calculates cold count average and standard deviation at each scan using all observations within +/-4 scans before and after. This is the blue curve on the left side of Figure 21. A cold observation is preliminarily flagged if the cold count exceeds a certain threshold, which we set to the lowest quartile plus 1 standard deviation. We then go through the cold swath map for the orbit -position map again and at each point we count the flagged events within a window of +/-2 scans and +/-2 cells. The final flag for that point is set if more than 60% out of these 25 surrounding events have the primary flag set, indicating a spatially coherent pattern that is typical for moon or RFI contamination. Events for which the final flag is set are excluded when computing the cold count average.

11.3 RFI and Sun Glint Flagging

11.3.1 RFI Glint Flagging

RFI from geostationary TV satellites can be reflected from the ocean surface into the main reflector. So far, it has been observed at 10.7 GHz for WindSat and to a smaller extent also for AMSR. If the location of the geostationary satellite that causes the RFI is known, one can develop a flag based on the location of the radiometer S/C and the location of the observed Earth cell.

The geostationary TV satellite orbit must parallel to the Earth equator. Its distance from the Earth center $\rho_{geostat} = 42164.17244 \text{ km}$ can be determined from the equation of motion, which is equals the gravity force to the centrifugal force:

$$\frac{GM_E \cdot m_{geostat}}{(\rho_{geostat})^2} = m_{geostat} \cdot \omega_E^2 \cdot \rho_{geostat}, \quad GM_E = 398600.4405 \text{ km}^3 \text{ s}^{-2} \quad (141)$$

$\omega_E = \frac{2\pi}{T_{sidereal}} = 0.7292115 \cdot 10^{-4} \frac{\text{rad}}{\text{s}}$ is the circular frequency of the Earth rotation [24]. In

order to be geostationary the orbital time of the satellite must equal the sidereal day $T_{sidereal} = 86164.10064 \text{ s}$.

If the geodetic longitude $\lambda_{geostat}$ is known, we can calculate the vector $\mathbf{R}_{geostat}$ pointing from the Earth center to the geostationary satellite in the ECI system from equation (159) of Appendix A . The geodetic coordinates of the Earth cell that is observed by the radiometer determine the vector \mathbf{R}_E from the Earth center to the earth cell according to equation (189) of Appendix B . $\mathbf{R}_{E-geostat} \equiv \mathbf{R}_{geostat} - \mathbf{R}_E$ is the vector from the Earth cell to the geostationary TV satellite and $\hat{\mathbf{R}}_{E-geostat}$ the corresponding unit vector in the ECI. The unit vector of an electromagnetic ray that was emitted from the radiometer to the Earth cell and is specularly reflected at the ocean surface is

$$\hat{\mathbf{r}}_{spec} = \mathbf{b}_0 - 2 \cdot \langle \mathbf{b}_0 \cdot \mathbf{U} \rangle \cdot \mathbf{U} \quad (142)$$

where \mathbf{U} is the surface normal vector pointing upward from the Earth (equation (194) of Appendix B) and \mathbf{b}_0 is the boresight unit vector (equation (195) of Appendix B). If the ocean surface was exactly specular than $\hat{\mathbf{R}}_{\text{E-geostat}} \equiv \hat{\mathbf{r}}_{\text{spec}}$ would be the condition for RFI intrusion. Because the ocean surface is rough, RFI can also intrude if it comes from non-specular directions. We compute the RFI glint angle φ_{RFI} as the angle between $\hat{\mathbf{R}}_{\text{E-geostat}}$ and $\hat{\mathbf{r}}_{\text{spec}}$:

$$\varphi_{RFI} = \arccos \left\langle \hat{\mathbf{R}}_{\text{E-geostat}} \cdot \hat{\mathbf{r}}_{\text{spec}} \right\rangle \quad (143)$$

The condition for RFI intrusion is that $|\varphi_{RFI}| < \varphi_{RFI}^{crit}$. Earth observations that are flagged for this condition should not be used for any geophysical applications. This type of geometrical flagging should of course only be applied if the Earth cell is located within the boundaries of the region into which the geostationary TV satellite is broadcasting. The easiest way to handle this is to draw a large enough rectangular box around the broadcast region and apply the RFI check only within this window. The value of the critical angle φ_{RFI}^{crit} depends on the frequency and strength of the RFI source in relation to the bandwidth of the 10.7 GHz channel. It can only be determined post-launch by trial and error from looking at brightness temperature maps of the regions into which the TV satellite is broadcasting.

At WindSat we have observed RFI at 10.7 GHz from 3 TV satellites (Table 23):

Table 23: Geostationary TV satellites causing RFI intrusion for the WindSat 10.7 GHz channels.

geostationary TV satellite	longitude $\lambda_{\text{geostat}}(^{\circ})$	window of broadcast region ($^{\circ}$)	affected parts of the swath
HOTBIRD	+13.0	longitude: [-25, +45] latitude: [+20, +80]	descending forward ascending backward
ASTRA	+19.0	longitude: [-25, +45] latitude: [+20, +80]	descending forward ascending backward
PAS-3R	-43.0	longitude: [-80, -30] latitude: [-45, -10]	ascending forward descending backward

Because the WindSat 10.7 GHz channels have a large bandwidth of 300 MHz we need to use a rather large value for the cutoff angle $\varphi_{RFI}^{crit} = 35^{\circ}$. For AMSR the bandwidth is only 100 MHz and a smaller value of $\varphi_{RFI}^{crit} = 25^{\circ}$ is sufficient. Moreover, at AMSR we have only found RFI glint that was caused by the first two satellites of Table 23.

Figure 23 and Figure 24 demonstrate how the RFI flint flagging works. The WindSat 6 H-pol and 10 H-pol observations had been resampled to a fixed Earth grid. Figure 23 shows the absolute value of the glint angle $|\varphi_{RFI}|$ for the case of the PAS-3R satellite at -43.0° longitude, which broadcasts over South America and leads to RFI glint for the WindSat ascending forward and descending backward looking swaths. All observations between rev# 2900 and rev# 7000 have been averaged together. Figure 24 shows the brightness temperature difference between 10H-pol and 6H-pol. The left panel was computed without RFI flagging. RFI is evident off the coast of Brazil. The right panel

was computed after including all RFI flagged observations. Because some map cells of the RFI flagged map contain only very few events, this map looks rather noisy.

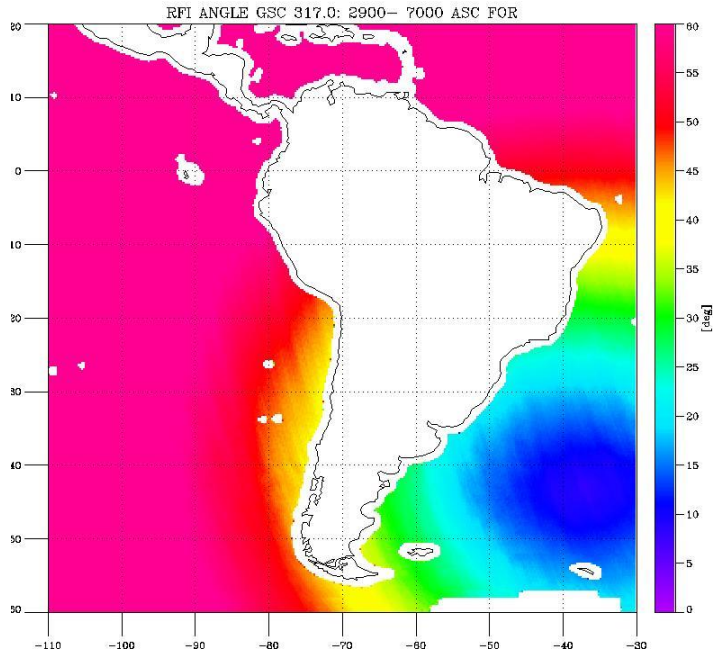


Figure 23: Absolute value of the RFI glint angle between the WindSat boresight and the geostationary TV satellite PAS-3R at 43.0° longitude.

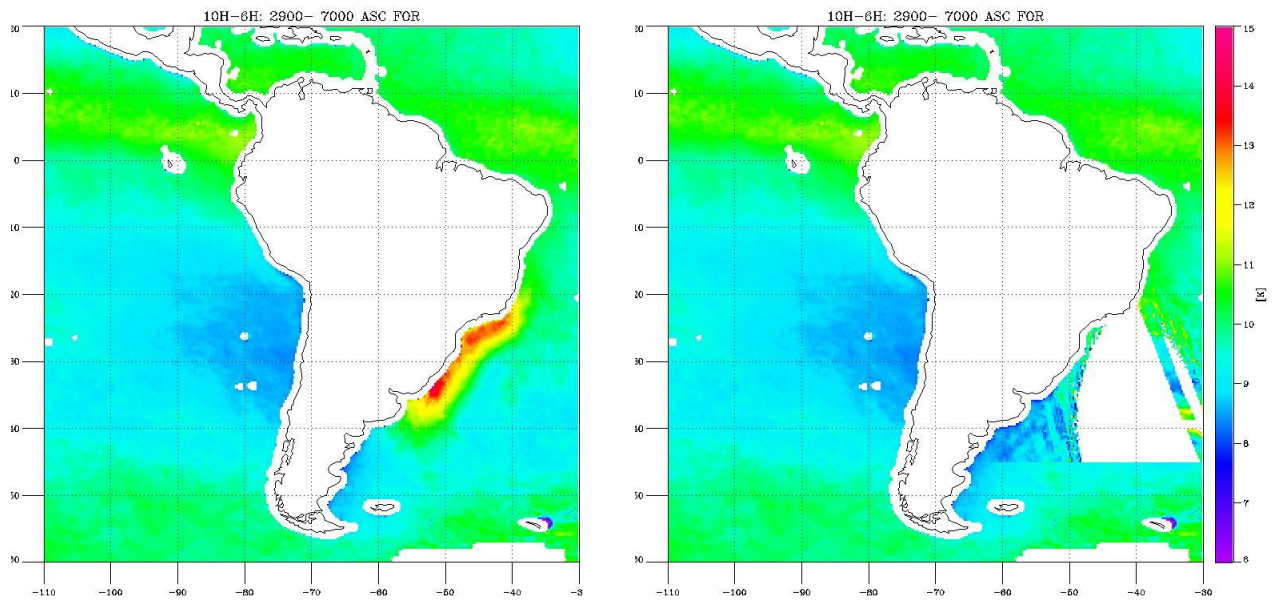


Figure 24: Brightness temperature difference between the WindSat 10 H-pol and 6 H-pol for the ascending forward looking swath. The maps show the averages of all orbits between rev# 2900 and rev# 7000. The left panel shows the result without applying the RFI glint flag. The right panel shows the result after events that were flagged for RFI were excluded from the data set.

11.3.2 Sun Glint Flagging

The same method can be applied to flag observations for sun light that is reflected from the ocean surface. The vector $\hat{\mathbf{r}}_{\text{sun}}$ from the Earth to the sun replaces the vector to the geostationary satellite $\hat{\mathbf{R}}_{\text{E-geostat}}$ in (143). Sun light is synchrotron radiation and therefore the sun brightness temperature decreases with increasing frequency ranging from about 22,000 K at 6.8 GHz to 7,000 K at 37.0 GHz. We can therefore decrease the critical angle $\varphi_{\text{sun}}^{\text{crit}}$ of the sun glint flag with increasing frequency. For SSM/I, TMI, AMSR and WindSat we use $\varphi_{\text{sun}}^{\text{crit}} = 25^\circ$ for C-band and X-band frequencies and for all higher frequency bands we use $\varphi_{\text{sun}}^{\text{crit}} = 10^\circ$. We expect that the values for GMI are the same.

11.4 Earth Intrusion into the Cold Sky View

Earth view contamination of the cold sky view can arise if the cold mirror does not cover the feed completely during the cold scan. That means that radiation from Earth can enter the cold mirror through its backlobes through the main reflector, which still sees the Earth during the cold sky view. This is most likely to occur for the low frequency feeds (10.7 GHz). The problem turned out to have a sizeable effect for both AMSR instruments (AMSR-E and Midori) but was also observed for the WindSat 6 GHz and 10 GHz channels, though its size is about 5 – 10 times smaller than it is for AMSR.

To determine its size quantitatively and derive a correction for it, we first produce a static map of antenna temperature measurements of the Earth. During flight, we calculate the Earth boresight location at each cold scan sample. We then average the cold counts into a map of the Earth. The upper panel of Figure 25 shows the result for 6H for 5,000 (about 1 year) WindSat orbits. A small intrusion of the Earth is visible in the cold count map leading to a contrast between the radiometrically hot land versus the radiometrically cold ocean.

The actual cold count temperature $T_c^{\text{eff}}(X)$ during the cold scan is then determined as:

$$T_c^{\text{eff}}(X_E) = (1 - \lambda)T_c + \lambda T_{B,E}(X_E) \quad (144)$$

where X_E is the Earth location, $T_c = 2.7K$, $T_{B,E}(X)$ is the brightness temperature due to the Earth radiation and $\lambda = f_E$ is the beam fraction from the Earth view. We have assumed here that there are no other intrusions into the cold sky view and that the cold sky reflector is not emissive. Let $C_c(X)$ be the observed cold counts before doing any scan averaging. They contain the Earth view intrusion. The corrected, uncontaminated cold counts are called C_c^{corr} . Assuming that the calibration is linear we can write:

$$\begin{aligned} C_c(X_E) &= a \cdot T_c^{\text{eff}}(X_E) + b \\ C_c^{\text{corr}} &= a \cdot T_c + b \end{aligned} \quad (145)$$

The coefficients a and b denote an average gain and offset that apply over the time period which was used to produce the map in Figure 25. Substituting (144) into (145) gives:

$$C_c^{\text{corr}} = C_c(X_E) - a \cdot \lambda \cdot [T_{B,E}(X_E) - T_c] \quad (146)$$

$T_{B,E}(X)$ is taken from the static TB map. The parameter λ is varied until the Earth contours in the lower plot of Figure 25 vanish. For the WindSat 6 GHz and 10 GHz channels we have found that λ is about 0.0005. For AMSR Midori it is about 5 times larger and for AMSR-E about 10 times larger. For WindSat ($\lambda \approx 0.0005$) the maximal size of the radiometric impact of this correction to the calibrated TA is 0.12 K. However, its actual size depends on the location, in other words the radiometric correction due to Earth contamination of the cold mirror is not a constant bias.

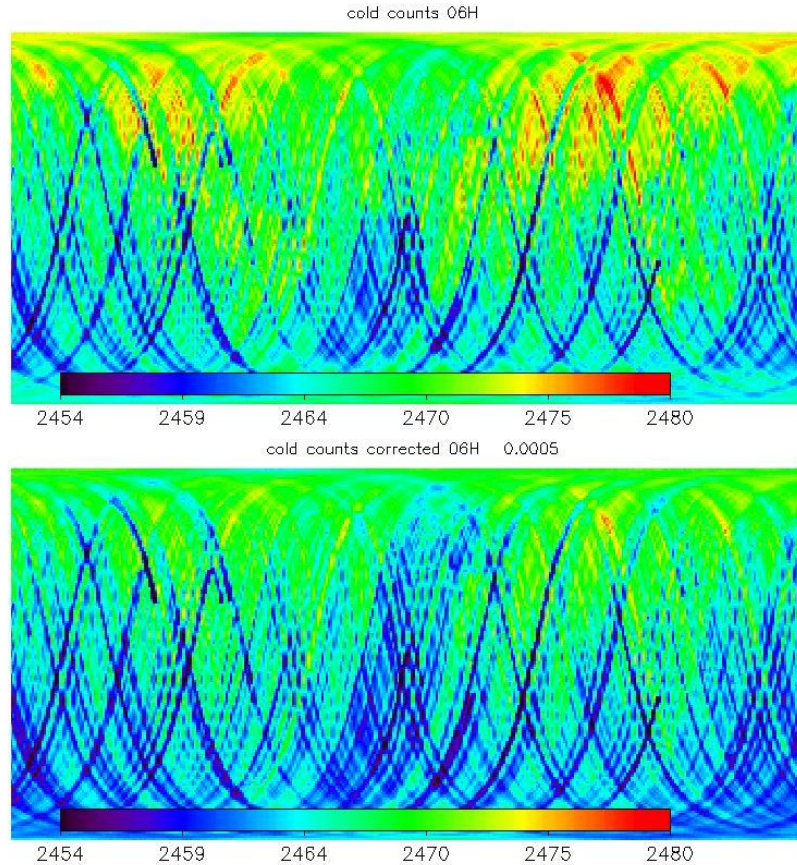


Figure 25: Earth map of cold counts for the 6H channel: Upper panel before, lower panel after doing the correction.

Once we have determined the value of λ we can use it in the calibration algorithm to derive an effective cold sky temperature for each cold sky according to (144) using the static Earth TA map. Finally we compute a scan average for $T_c^{eff}(X_E)$. It should be noted that the calibration algorithm does not correct the cold count themselves, but it corrects the cold sky brightness temperature. The values for the cold counts are the one that are measured, which contain the Earth view contamination.

11.5 Sun Intrusion into the Hot Load

Sun intrusion into the hot load can cause temperature gradients within the hot load and therefore lead to a deviation of the effective hot load temperature from the weighted average of the hot load PRT measurements (equation (4) of section 4.3). It has been observed for both AMSR instruments (AMSR-E and Midori), WindSat and SSMIS. For GMI we expect that the design of the hot load and the way it is mounted will shield it much better from sun intrusion than the hot loads of the other instruments. However, it might still turn out to be necessary a correction for it. Analysis and development of a

correction algorithm can only be done post-launch, as the error that is to be corrected depends on the design of the hot load, how it is shielded from the environment and the placing of the PRTs within the hot load. In the following we will briefly describe our analysis of the hot load anomaly for WindSat and how we developed a correction algorithm for it.

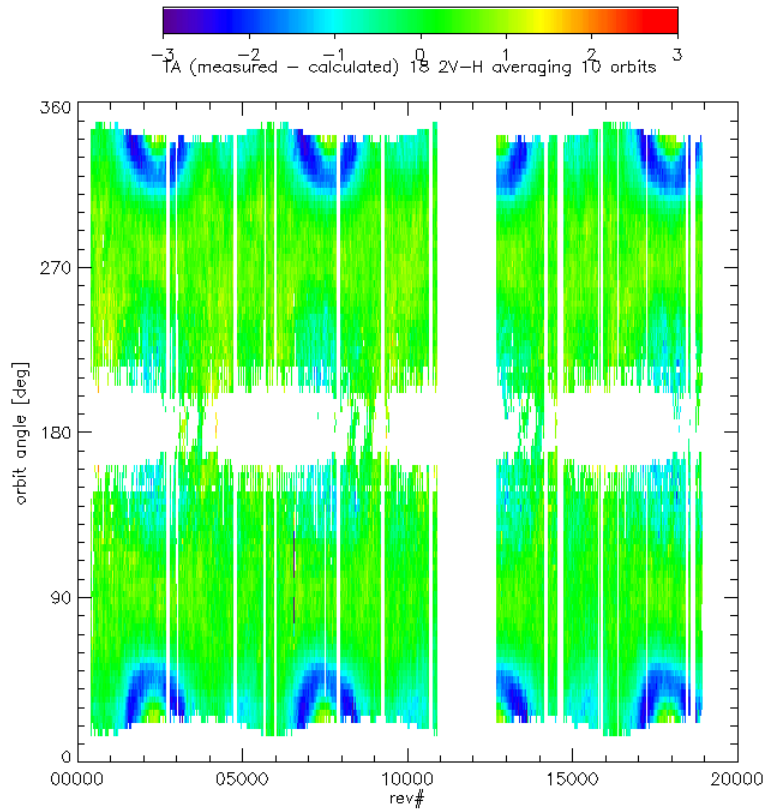


Figure 26: WindSat 18.7 GHz $2T_{A,v} - T_{A,h}$ measured – computed as a function of orbit number (rev #) and orbital angle.

The basic tool is to plot difference between measures and RTM computed antenna temperatures as function of time (orbit #) and intra-orbit position (fractional rev # or orbit angle). An orbit angle of 0 deg and 360 deg corresponds to highest southern latitude in the orbit, an orbit angle of 180 deg corresponds to the highest northern latitude in the orbit and orbit angles of 90 deg (270 deg) correspond to the equatorial crossings in the ascending (descending) swaths. Figure 26 shows the result for almost 20000 orbits of the WindSat 18.7 GHz channel combination of 2 v-pol – h-pol. Averages over 10 orbits were taken to reduce the noise. Section 12.1 explains in detail the procedure of the RTM calculation.

For computing the radiometer gain and offset we are using the hot load temperature T_h^{PRT} that is obtained from the weighted thermistor average temperatures. The weights for the thermistor averages depend on the frequency bands and were specified by the Naval Research Laboratory (NRL). These gain values are the ones to be used if there was no sun intrusion into the hot load.

The sun intrusion is clearly visible in Figure 26. The main intrusion occurs in the southern hemisphere and is due to reflection of the sun light from the tray into the hot load. A smaller intrusion is due to direct intrusion of sun light into the hot load and occurs in the northern hemisphere. At other frequencies, the problem is not evident (6.9, 10.7, 23.8 GHz) or it is much smaller (37 GHz). The reason for this is that the sun intrusion into the hot load affects mainly the thermistors that measure the hot load temperature for the arc of the 18 GHz horns. A detailed description of the WindSat hot load anomaly can be found in [25]. The anomaly is largest during times at which the sun either hits the hot load directly or if sun radiation gets reflected from the tray into the hot load.

We have developed an for correcting this problem for the 18 and 37 GHz channels. It takes the following steps:

1. From the difference between measured and computed antenna temperatures, we can calculate what the effective hot load temperature T_h^{eff} should be so that the WindSat antenna temperatures match the RTM antenna temperatures, making the assumption that the RTM TA is the correct value. The radiometric transfer equations (8)-(9) for the measured and calculated TAs are:

$$\begin{aligned} T_{A,2v-h}^{meas} &= xT_h^{PRT} + (1-x)T_c^{eff} - 4T_{nl} \cdot x \cdot (1-x) \\ T_{A,2v-h}^{RTM} &= xT_h^{eff} + (1-x)T_c^{eff} - 4T_{nl} \cdot x \cdot (1-x) \\ x &= \frac{C_E - \bar{C}_c}{\bar{C}_h - \bar{C}_c} \end{aligned} \quad (147)$$

Taking the difference between measured and RTM TA we obtain:

$$T_{A,2v-h}^{meas} - T_{A,2v-h}^{RTM} = x(T_h^{PRT} - T_h^{eff}) = -x\Delta T_{eff} \quad (148)$$

and because nonlinearity and cold space temperature are small compared with the hot load temperature, i.e. $T_A^{meas} \approx xT_h^{PRT}$:

$$\Delta T_{eff} \approx -\frac{T_h^{PRT}}{T_A^{meas}} \cdot [T_{A,2v-h}^{meas} - T_{A,2v-h}^{RTM}] \quad (149)$$

2. We find that the difference $\Delta T_{eff} = T_h^{eff} - T_h^{PRT}$ is correlated to the sun angle β , which we define as the angle between the sun vector and the S/C z-axis (spin axis). We derive a regression between ΔT_{eff} and β . This is done once using all available orbits.

3. For a given β we can then calculate the correction to the hot load temperature

$$T_h^{eff} = T_h^{PRT} + \Delta T_{eff}(\beta) \text{ and recompute the gain using this corrected hot load temperature.}$$

4. We apply a smoothing to this corrected gain value. In order to do this we use the fact that the gain a is correlated to the cold counts C_c through the basic radiometer equation $C_c = a(T_{rcv} + T_c) + C_0$, where T_{rcv} is the temperature of the receiver, $T_c = 2.7K$ is the cold space temperature and C_0 is some offset. Assuming that the cold counts vary harmonically with the orbit angle z , we fit the gain to a Fourier series in z :

$$a = b + d_0 C_c + d_1 \cos z + d_2 \sin z + d_3 \cos 2z + d_4 \sin 2z \quad (150)$$

This is done separately for each orbit. These are the final gain values that we use to compute antenna temperatures from earth view counts.

The correction $\Delta T_{eff}(\beta)$ and the resulting gain curves as function of the orbit angle z are shown in Figure 27 for one WindSat orbit.

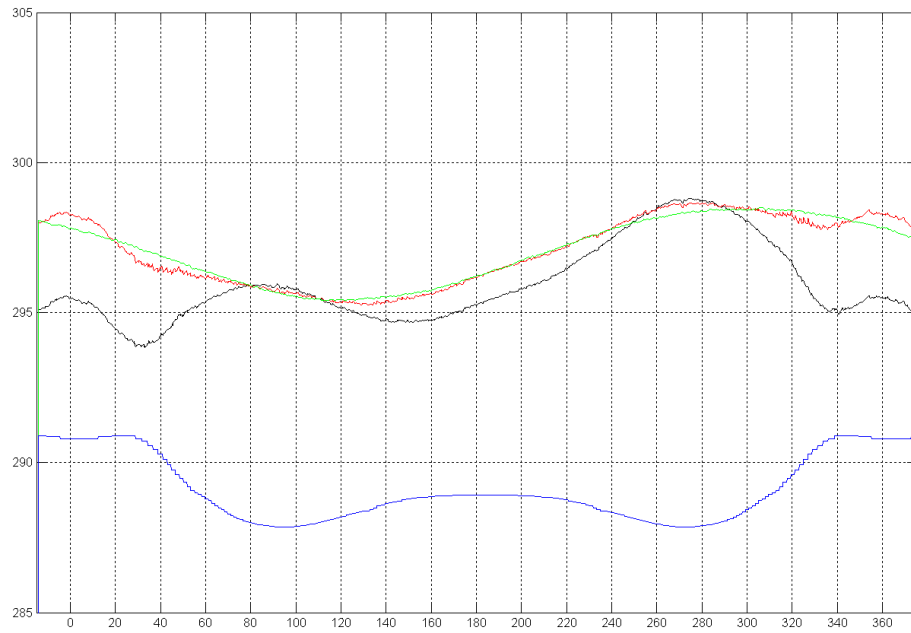


Figure 27: Gain as function of orbital angle for orbit # 1601. The black curve is the gain using the average thermistor temperatures (no hot load anomaly correction). The red curve is the gain after applying $\Delta T_{eff}(\beta)$. The green curve is the final gain after smoothing by fitting it to the cold counts + 2^{nd} order harmonics in z . The blue curve is $\Delta T_{eff}(\beta)$ shifted by 288K.

12 Post-Launch Calibration and Validation

This chapter outlines the main steps of the post-launch calibration and validation (cal/val) method. We give examples of how this method has been applied and worked for other radiometers. We expect that we will follow the same basic steps for the GMI pos-launch cal/val.

12.1 Basic Tool for Post-Launch Calibration

Measured Versus Computed Brightness Temperatures

The basic tool for our post-launch calibration method is to compare antenna temperatures (TA) or brightness temperatures (TB) that are measured from the radiometer with those that were computed from our RTM. The reason for analyzing the difference between measured and RTM computed antenna TA's or TB's rather than analyzing just the measured TAs or TBs themselves, is that we want to take out the variability of the environmental scene as much as possible. This is especially important for a cal/val shortly after launch where only a relatively small (1 -3 month) data set is available. Generally it is safer to work on the TA level rather than on the TB level. The reason for this is that an error in one polarization channel can contaminate the other polarization after the cross polarization correction gets applied. In order to calculate the TA from the TB of the RTM we use the simplified forms (112) and (113).

For computing the TB from the RTM we need to have environmental scenes. In principle it is desirable that these scenes are as accurate as possible. The general method for collocating environmental scenes with radiometer measurements is:

1. Atmospheric profiles of pressure, temperature, water vapor density and liquid cloud water density are taken from NCEP GDAS and linearly interpolated to the time and location of the radiometer measurement.
2. The NCEP cloud water density profiles contain both liquid water and ice. The radiometer measurement is at low frequencies (89 GHz and below) only sensitive to absorption by the liquid phase. In order to extract the liquid cloud density from the NCEP cloud water density profiles we assume that the cloud is water is completely in the liquid phase if the air temperature of the profile level is above $0^{\circ}C$ and completely in the ice phase if it is below $-20^{\circ}C$. For temperatures in between, we linearly interpolate the liquid density as a function of temperature.
3. SST is taken from the Reynolds OI products [21] and linearly interpolated to the time and location of the radiometer measurement.
4. For sea surface salinity we use we use the climatology from the World Ocean Atlas (WOA98, N.O.D.C, CD-ROM).
5. The surface wind speed and direction is taken from NCEP GDAS and linearly interpolated to the time and location of the radiometer measurement.
6. If Earth products from a second well calibrated radiometer are available that are close enough in time to the radiometer measurements that we want to calibrate, then we take the values for the columnar water and liquid cloud water of this second radiometer. We scale the NCEP GDAS profiles for water vapor density and liquid cloud water so that its columnar integral equals the radiometer measurement. For example for the WindSat cal/val we use SSM/I F13 measurements of columnar water vapor and cloud water. Both instrument collocate well within a 60 minute time window. The reason for doing this

scaling of the atmospheric density profiles is that the values for the columnar vapor and cloud water from NCEP tend to be relatively inaccurate whereas their profiles are more reliable.

7. Measurements are discarded that are over or close to land, ice or rain or are contaminated by RFI. In order to eliminate rain one can either require that the antenna temperature stays within the limit for rain free ocean scenes or that the columnar liquid cloud water is below 0.18 mm [14;26].

8. If available, we use the channel combination 2v-h for a given frequency, rather than v-pol and h-pol. Taking this combination reduces the error in the brightness temperatures that arises due to the errors in the atmospheric parameters [19].

9. It is not always necessary to perform a full integrations over the atmospheric profiles - (104) in the RTM calculation but one can take a simplified version of the RTM that uses only the columnar values for vapor and cloud together with sea surface temperature [14]. This method is computational much faster. Rather than using the NCEP values for columnar water vapor and cloud water one can also calculate the water vapor from SST based on the strong global correlation between vapor and temperature [14] and use a global climatology of liquid cloud water values that was derived from SSM/I measurements.

The purpose of the cal/val is to analyze biases between the radiometer measurements and the RTM computations. Errors in the environmental scenes tend to cancel out if large enough averages are taken. Generally, that means the more data are available, the less accurate the environmental scenes have to be. For a first cal/val that uses only 1-3 months of data we will try to use the more accurate method. For performing the cal/val with larger data sets, where computational time gets also an issue, we can use the simpler and faster methods.

12.2 Analysis and Correction of Sensor Pointing Errors

The first step in the post-launch cal/val plan is the analysis and correction of sensor pointing errors. Those errors include for example misspecification of nadir angle, azimuth angle, S/C attitude or time of the measurement. Different types of pointing error have been observed at other instruments, but each instrument had its own specific problem. TMI, AMSR-E and WindSat exhibited misspecifications of the S/C attitude, at WindSat there were in addition misspecifications of the azimuth offset and at SSMIS the value of the one of the nadir angles was incorrect. It seems obviously difficult to specify the pointing geometry pre-launch to the necessary degree of accuracy.

The basic method for both checking the pointing accuracy and correct potential errors is to calculate high resolution ($1/4^\circ$ or higher) global maps of average antenna temperature measurements for both the ascending and the descending swath and then plot the map of the difference of both. Pointing errors will cause coast lines and large rivers showing contours on the map. For most cases it is enough to use 1 – 3 months of data for the averaging. The misspecification is then found and corrected by trial and error. That means that the pointing parameter is adjusted until the showing of the coastlines and rivers in the map disappear. In some cases it is difficult or impossible to determine the cause of the pointing error. For example, a misspecification of the azimuthal offset will have the same effect as a misspecification of the yaw angle. As an example, Figure 28 and Figure 29 show the ascending minus maps for the SSMIS 18H channel before and after an ad-

justment of the nadir angle by -0.12° . This value corresponds to an error in geolocation of about 4 km.

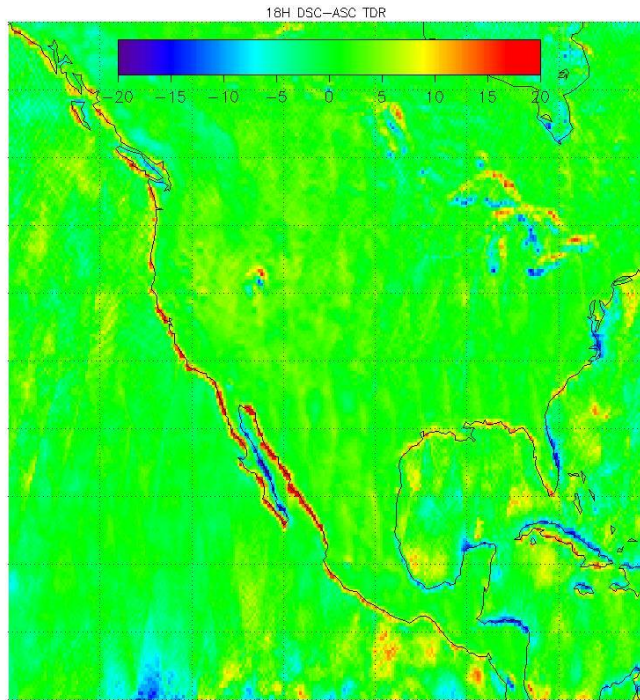


Figure 28: Descending minus ascending maps of SSMIS channel 18H for 500 (about 1 months) orbits with no nadir angle adjustment.

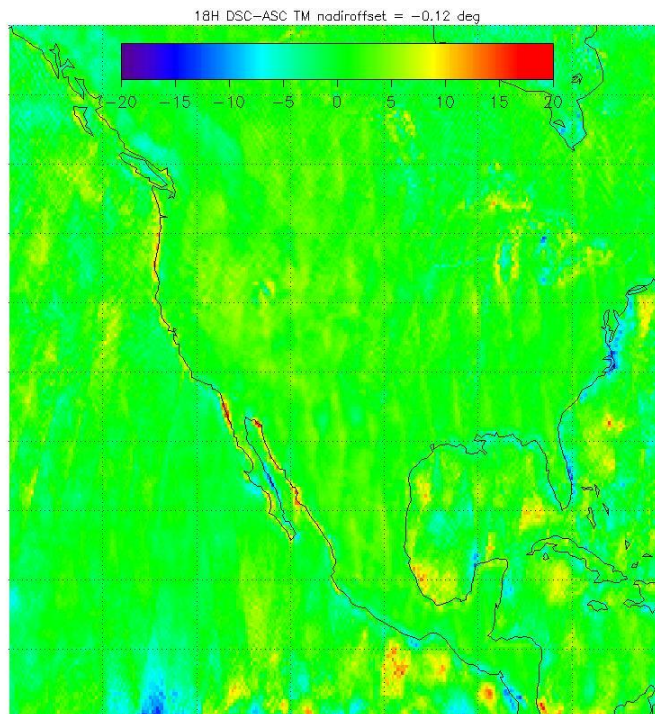


Figure 29: Descending minus ascending maps of SSMIS channel 18H for 500 (about 1 months) orbits after adjusting the nadir angle by -0.12° .

12.3 Analysis and Correction of Along-Scan Biases and Orbital-Position Dependent Biases in the Earth View Sector

The second step in the post-launch cal/val plan is the analysis of TA(measured) minus TA (RTM) (section 12.1) as a function of the along-scan position or Earth sample. We are looking for systematic deviation from a constant value and the variation of this deviation over the scan. We are also analyzing the standard deviation of TA(measured) minus TA (RTM) as a function of scan position. An overall bias that does not depend on the scan position is not yet of interest at this point. It will be dealt with when doing the absolute calibration (section 12.6). If TA(measured) minus TA (RTM) has a bias that depends on the along-scan position but on the same its standard deviation stays constant, there can be various causes:

1. Pointing errors that cause an variation of the Earth incidence angle across the scan. This has been observed at WindSat due to an misspecification of the S/C roll and pitch [27;28].
2. The calibration loads are intruding into the Earth view leading to a roll off near the edge of the Earth view sector. This has been observed at WindSat. After correcting for it, it was possible to widen the WindSat Earth view sector in the in the vicinity of the calibration loads.
3. The S/C or instrument is intruding into the Earth view.
4. Emission from an on-board RFI source. This has been observed at F15 SSM/I caused by the RADCAL beacon [29]. It has also been observed at some of the WindSat 18 GHz channels caused by an unknown source.

If the source of the error cannot be easily corrected, then we can derive a multiplicative static along scan bias correction in the following way, which is akin to the spillover correction (113):

$$T_{A,i}^{meas} = (1 - \lambda_i) T_{A,i}^{true} + \lambda_i T_{cont} = T_{A,i}^{true} + \lambda_i (T_{cont} - T_{A,i}^{true}) \quad (151)$$

$i = 1, \dots, n_{Earth}$ is the along scan position. λ_i denotes the contamination parameter. We identify the true antenna temperature $T_{A,i}^{true}$ with $T_{A,i}^{RTM}$. We also assume that $T_{cont} \square T_{A,i}^{true}$ or that $T_{cont} - T_{A,i}^{true}$ is proportional to $T_{A,i}^{true}$. That means that we treat the bias effectively like a spillover correction. The multiplicative along-scan bias correction λ_i can then be derived at each position i from the observations $T_{A,i}^{meas}$ and $T_{A,i}^{RTM}$ in the whole calibration set by a linear regression as:

$$T_{A,i}^{meas} = (1 - \lambda_i) T_{A,i}^{RTM} \quad (152)$$

where we have assumed that $|\lambda_i| \square 1$. Typical at least 1 – 3 months of data are necessary to determine λ_i from (152). Once λ_i has been determined we can then apply it to any measurement $T_{A,i}^{meas}$ in order to obtain a corrected value according to:

$$T_{A,i}^{corr} = \frac{T_{A,i}^{meas}}{(1 - \lambda_i)} \quad (153)$$

In a similar way we can also derive a static correction for biases that depend on the intra orbit position.

If we drop the assumption that $T_{cont} \square T_{A,i}^{true}$ or that $T_{cont} - T_{A,i}^{true}$ is proportional to $T_{A,i}^{true}$, then there could be also a scene independent additive bias $\beta_i \equiv \lambda_i T_{cont}$ between $T_{A,i}^{meas}$ and $T_{A,i}^{corr}$ in addition to the multiplicative bias $1 - \lambda_i$. From experience, it is difficult to distinguish multiplicative and additive biases from analyzing rainfree ocean scenes (section 12.1), because the dynamical range of brightness temperatures from rainfree ocean scenes is relatively small.

12.4 Correction of Calibration System Anomalies

The third step in the post-launch cal/val is the analysis and correction of calibration anomalies. This is discussed in chapter 11.

12.5 Analysis and Correction of Along-Scan Biases in the Calibration Counts

Along scan biases in the calibration counts can arise from contamination of the calibration scan by stray radiation from outside such as the S/C, instrument, struts, gap, shroud etc. The essential assumption is that the measurements in the center of the calibration scans are not contaminated, but the contamination occurs only at the edges. We can check this assumption by calculating averages of the calibration counts separately for each cell positions using many data of the calibration set. In order to be able to do that it is necessary that the calibration scan is large enough. A correction for the effective calibration load temperature (cold sky or hot load) can then be derived the following way:

Let T_{cal}^{eff} be the calibration load temperature without contamination and T_{cont} the radiometric temperature of the contamination source. The effective calibration load temperature $T_{cal,i}^{eff}$ at cell position i can be written as:

$$T_{cal,i}^{eff} = (1 - \lambda_i) \cdot T_{cal}^{eff} + \lambda_i \cdot T_{cont} = T_{cal}^{eff} + \lambda_i \cdot (T_{cont} - T_{cal}^{eff}) \quad (154)$$

We can derive $T_{eff,i}^{cal}$ from the calibration count C_i and the radiometric transfer equations (8) and (9):

$$T_{cal,i}^{eff} = x_i T_h^{eff} + (1 - x_i) T_c^{eff} - 4T_{nl} x_i (1 - x_i) \quad (155)$$

$$x_i = \frac{C_i - \bar{C}_c}{\bar{C}_h - \bar{C}_c}$$

When calculating x_i in (155), the averages \bar{C}_c and \bar{C}_h are taken only for the calibration observations at the center of the scans which are not contaminated by the outside source. Using many observations from the whole calibration data set we can then find the value of the multiplicative bias λ_i and/or the additive bias $\beta_i \equiv \lambda_i T_{cont}$ from (154) by linear regression. Even more than for the Earth counts, it will be difficult to disentangle multiplicative from additive biases, because the dynamical range of the calibration load temperatures is very narrow. For the cold calibration scan and a hot contamination source $T_{cal}^{eff} \square T_{cont}$ and therefore the bias would be additive. For the hot calibration scan and a cold contamination source $T_{cal}^{eff} \square T_{cont}$ and therefore the bias would be multiplicative. But because T_{cal}^{eff} is almost constant, it will be difficult to distinguish it from an additive bias.

We derive a static correction tables λ_i or β_i for each calibration scan position i . These tables will be input to the cold and hot calibration modules, respectively. When running the calibration algorithm the modules will produce a scan dependent effective temperature $T_{cal,i}^{eff}$ at each scan position according to (154) using the values for λ_i , β_i and the effective calibration temperature T_{cal}^{eff} , which has been computed by the modules at each scan before applying any along scan bias correction. Finally, a corrected effective temperature for each scan is computed by performing an average over all temperatures analogous to (1).

12.6 Absolute Calibration

The final step in the post-launch cal/val is the absolute calibration. It amounts simply to an on-orbit readjustment of the cross polarization and spillover parameters (112) and (113) using TBs that were calculated from the RTM and TAs that were measured by the radiometer. We need to make the assumption that:

$$\begin{aligned} a_{vh} &\approx a_{hv} \equiv a \\ \eta_v &\approx \eta_h \equiv \eta \end{aligned} \tag{156}$$

It is our experience that this assumption is fulfilled to high degree of accuracy. For example we have observed that antenna temperatures over land do not depend on polarization, from which we conclude that the spillover does not depend on polarization. The assumption is also consistent with the symmetry of the antenna patterns (78). For a frequency with dual polarization measurements this leaves us with two equations for the two unknowns a and η . The first step is to obtain the spillover factor η from the sum of v-pol and h-pol:

$$T_{A,v} + T_{A,h} \approx \eta \cdot (T_{B,v} + T_{B,h}) \tag{157}$$

The cross polarization contamination parameter a can then be calculated from:

$$T_{A,v} = \eta \cdot [T_{B,v} + a \cdot (T_{B,h} - T_{B,v})] \tag{158}$$

One necessity for doing the absolute calibration is the fact that accurate pre-launch measurements of the antenna patterns are very difficult, especially for the backlobes. This, in turn, makes it very difficult to accurately determine the spillover value pre-launch. Another purpose of the absolute calibration is to remove any residual biases within the calibration procedure.

It should be noted that the absolute calibration absorbs some other residual biases that have not been removed yet. In many cases the effect of those biases are indistinguishable and get therefore absorbed in the same way. For example, a residual bias in the effective hot load temperature effects the T_A in the same way as spillover does. Therefore any bias in the effective hot load temperature will get absorbed into the spillover readjustment (157).

For the absolute cal/val we use two separate data set. The first one is used for deriving the post-launch values of a and η . The second one is used for testing by calculating the difference between measured and calculated TAs or TBs using those derived values. Training and test sets should be from different time periods, each of those periods comprising at least 3 – 6 months of data. The total bias between measurement and calculation in the test set should be very small. This indicates that the absolute calibration is stable.

We show the results for the WindSat absolute calibration as example. Table 24 shows the values of the APC coefficients that were measured pre-launch by NRL and compares them with the ones from the RSS absolute calibration. With the only exception of the 6.8 GHz spillover factor we find excellent agreement between the pre-launch measurements and the post-launch ca/val. This indicates that the pre-launch NRL antenna pattern measurements had been very accurate. It also indicates that there are very only small residual biases in the calibration system or that they have been effectively removed.

The standard deviation of TB (measured) minus TB (computed) is approximately 0.4 K at all 5 WindSat frequencies for the channel combination $v - h/2$. One still needs to account for the fact that that the RTM calculation can contain a considerable error in the environmental scene and that there is a sampling mismatch between the WindSat measurement and the environmental scene (e.g. NCEP GDAS, Reynolds OI SST), that has been used in the RTM calculation. After removing this error we estimate the accuracy of both our RTM and the calibrated WindSat brightness temperatures to be about 0.2 K.

Table 24: Values for spillover and cross polarization contamination for WindSat from the NRL pre-launch antenna pattern measurements and the RSS post-launch absolute calibration.

	Band [GHz]	NRL (Pre-Launch)	Absolute Calibration (Post-Launch)
Spillover	6.8	0.9977	0.9811
	10.7	0.9973	0.9947
	18.7	0.9962	0.9934
	23.8	0.9963	0.9926
	37.0	0.9957	0.9938
Cross polarization contamination	6.8	0.9950	0.9944
	10.7	0.9967	0.9963
	18.7	0.9959	0.9898
	23.8	0.9879	0.9882
	37.0	0.9961	0.9958

Appendix A Coordinate Systems and Transformations

A.1 Earth Centered Inertial System (ECI)

The axes $\mathbf{E}_i, i=1,2,3$ of the inertial geocentric-equatorial coordinate system (ECI) [24] are as follows:

1. \mathbf{E}_3 points along the Earth rotation axis from S to N.
2. \mathbf{E}_1 lies in the equatorial plane pointing into the direction of the vernal equinox.
3. $\mathbf{E}_2 \equiv \mathbf{E}_3 \times \mathbf{E}_1$ completes the right hand system.

For the following, we assume that the Earth rotation axis is fixed and neglect precision and nutation.

The axes $\mathbf{E}'_i, i=1,2,3$ of the Earth fixed (rotating) geocentric-equatorial system are:

1. $\mathbf{E}'_3 \equiv \mathbf{E}_3$.
2. \mathbf{E}'_1 lies in the equatorial plane pointing into the direction of the Greenwich meridian.
3. $\mathbf{E}'_2 \equiv \mathbf{E}'_3 \times \mathbf{E}'_1$ completes the right hand system.

A.2 Geodetic System

The geodetic reference frame is the nominal nadir pointing flight system without yaw maneuver. Its axes $\mathbf{e}_i, i=1,2,3$ are defined as (GMI ICD-422-30-00-004):

1. \mathbf{e}_3 is pointing downward from S/C to the Earth nadir point.

2. $\mathbf{e}_2 \equiv \frac{\mathbf{e}_3 \times \mathbf{V}_{S/C}}{|\mathbf{e}_3 \times \mathbf{V}_{S/C}|}$ almost apposite to the orbit normal vector $\mathbf{L}_0 = \frac{\mathbf{R}_{S/C} \times \mathbf{V}_{S/C}}{|\mathbf{R}_{S/C} \times \mathbf{V}_{S/C}|}$.

$\mathbf{e}_1 \equiv \mathbf{e}_2 \times \mathbf{e}_3$ is close to the S/C velocity $\mathbf{V}_{S/C}$.

The S/C coordinate vector $\mathbf{R}_{S/C}$ in the ECI system $\mathbf{E}_i, i=1,2,3$ is:

$$\mathbf{R}_{S/C} = \begin{pmatrix} r_1 \\ r_2 \\ r_r \end{pmatrix} \cdot \hat{\mathbf{R}}_{S/C} = \begin{pmatrix} \left[\frac{\rho_e}{\sqrt{1-\varepsilon^2 \sin^2(\Theta_{S/C})}} + h_{S/C} \right] \cos(\Theta_{S/C}) \cos(\Phi_{S/C}) \\ \left[\frac{\rho_e}{\sqrt{1-\varepsilon^2 \sin^2(\Theta_{S/C})}} + h_{S/C} \right] \cos(\Theta_{S/C}) \sin(\Phi_{S/C}) \\ \left[\frac{\rho_e(1-\varepsilon^2)}{\sqrt{1-\varepsilon^2 \sin^2(\Theta_{S/C})}} + h_{S/C} \right] \sin(\Theta_{S/C}) \end{pmatrix} \quad (159)$$

$R_{S/C} = |\mathbf{R}_{S/C}| = \sqrt{(r_1^2 + r_2^2 + r_3^2)}$ is the distance from the S/C to the Earth center, $h_{S/C}$ is the S/C altitude and $\Theta_{S/C}$ is the geodetic S/C latitude. $\Phi_{S/C} = \lambda_{S/C} + \Theta(t)$ with $\lambda_{S/C}$ being the S/C longitude. $\rho_e = 6378.137$ km is the Earth equatorial radius, $\rho_p = 6356.824$ km is the Earth polar radius, $\varepsilon^2 = 1 - \frac{\rho_p^2}{\rho_e^2} = 0.006671977$ is the square of the numerical geoid eccentricity.

Given the Cartesian components of $\mathbf{R}_{S/C}$, the geodetic coordinates $\Theta_{S/C}$, $\Phi_{S/C}$ and $h_{S/C}$ in (159) can be obtained using the iterative method in [24], chapter 5.5.

A.3 Gauss System

$\mathbf{N}_1 \equiv \frac{\mathbf{E}_3 \times \mathbf{L}_0}{|\mathbf{E}_3 \times \mathbf{L}_0|}$ points from the Earth center into the direction of the ascending equatorial crossing. The 3 vectors: \mathbf{N}_1 , $\mathbf{N}_2 \equiv \mathbf{L}_0 \times \mathbf{N}_1$ and $\mathbf{N}_3 \equiv \mathbf{L}_0$ constitute a right hand system. The x and y axes of this system are in the orbital plane.

The S/C location vector $\mathbf{R}_{S/C}(t)$ at observation time t (measured since 12Z on 01 JAN 2000) in the Gauss frame is:

$$\mathbf{R}_{S/C}(t) = R_{S/C} \begin{pmatrix} \cos(\omega_{S/C}(t-t_0)) \\ \sin(\omega_{S/C}(t-t_0)) \\ 0 \end{pmatrix} \quad (160)$$

The S/C velocity $\mathbf{V}_{S/C}(t)$ in the Gauss frame is:

$$\mathbf{V}_{S/C}(t) = \frac{d}{dt} \mathbf{R}_{S/C}(t) = R_{S/C} \omega_{S/C} \begin{pmatrix} -\sin(\omega_{S/C}(t-t_0)) \\ \cos(\omega_{S/C}(t-t_0)) \\ 0 \end{pmatrix} \quad (161)$$

A.4 Transformation Between Gauss and ECI Systems

In general, the components of an arbitrary vector \mathbf{A} are:

$$\mathbf{A} = \sum_{k=1}^3 a_k \mathbf{N}_k = \sum_{l=1}^3 b_l \mathbf{E}_l \quad (162)$$

Furthermore:

$$\mathbf{N}_k = \sum_{m=1}^3 \langle \mathbf{N}_k \cdot \mathbf{E}_m \rangle \mathbf{E}_m \quad (163)$$

$\langle \cdot \rangle$ denotes the scalar product of 2 vectors. Therefore:

$$\begin{aligned} \mathbf{A} &= \sum_{k=1}^3 a_k \mathbf{N}_k = \sum_{k=1}^3 a_k \sum_{m=1}^3 \langle \mathbf{N}_k \cdot \mathbf{E}_m \rangle \mathbf{E}_m = \\ & \sum_{m=1}^3 \left[\sum_{k=1}^3 a_k \langle \mathbf{N}_k \cdot \mathbf{E}_m \rangle \right] \mathbf{E}_m \equiv \sum_{m=1}^3 b_m \mathbf{E}_m \end{aligned} \quad (164)$$

The coordinate transformation can be read off from equation (164) as:

$$b_m = \left[\sum_{k=1}^3 a_k \langle \mathbf{N}_k \cdot \mathbf{E}_m \rangle \right] \quad (165)$$

The vectors $\mathbf{N}_i = i = 1, \dots, 3$ can be obtained from the vectors $\mathbf{E}_i = i = 1, \dots, 3$ through the elementary Euler rotations:

1. Rotation around the z-axis by $+\alpha$.
2. Rotation around the (new) x-axis by $+i$.

α is right ascension of the ascending node, which is the angle between the vernal equinox and the ascending equatorial crossing. i is the orbital inclination angle.

The components of $\mathbf{N}_i = i = 1, \dots, 3$ in the $\mathbf{E}_i = i = 1, \dots, 3$ system are then given by the column vectors of the composite rotation matrix: $R_z(-\alpha) \cdot R_x(-i)$.

The elementary rotation matrixes are [24]:

$$\begin{aligned} R_x(\theta) &= \begin{pmatrix} 1 & 0 & 0 \\ 0 & \cos(\theta) & \sin(\theta) \\ 0 & -\sin(\theta) & \cos(\theta) \end{pmatrix} \\ R_y(\theta) &= \begin{pmatrix} \cos(\theta) & 0 & -\sin(\theta) \\ 0 & 1 & 0 \\ \sin(\theta) & 0 & \cos(\theta) \end{pmatrix} \\ R_z(\theta) &= \begin{pmatrix} \cos(\theta) & \sin(\theta) & 0 \\ -\sin(\theta) & \cos(\theta) & 0 \\ 0 & 0 & 1 \end{pmatrix} \end{aligned} \quad (166)$$

We have:

$$\begin{aligned} R_z(-\alpha) \cdot R_x(-i) &= \\ & \begin{pmatrix} \cos(\alpha) & -\sin(\alpha) & 0 \\ \sin(\alpha) & \cos(\alpha) & 0 \\ 0 & 0 & 1 \end{pmatrix} \cdot \begin{pmatrix} 1 & 0 & 0 \\ 0 & \cos(i) & -\sin(i) \\ 0 & \sin(i) & \cos(i) \end{pmatrix} = \\ & \begin{pmatrix} \cos(\alpha) & -\sin(\alpha)\cos(i) & \sin(\alpha)\sin(i) \\ \sin(\alpha) & \cos(\alpha)\cos(i) & -\cos(\alpha)\sin(i) \\ 0 & \sin(i) & \cos(i) \end{pmatrix} \end{aligned} \quad (167)$$

Writing out the scalar products in (165):

$$\begin{aligned}
\langle \mathbf{N}_1 \cdot \mathbf{E}_1 \rangle &= \cos(\alpha) & \langle \mathbf{N}_1 \cdot \mathbf{E}_2 \rangle &= \sin(\alpha) & \langle \mathbf{N}_1 \cdot \mathbf{E}_3 \rangle &= 0 \\
\langle \mathbf{N}_2 \cdot \mathbf{E}_1 \rangle &= -\cos(i)\sin(\alpha) & \langle \mathbf{N}_2 \cdot \mathbf{E}_2 \rangle &= \cos(i)\cos(\alpha) & \langle \mathbf{N}_2 \cdot \mathbf{E}_3 \rangle &= \sin(i) \\
\langle \mathbf{N}_3 \cdot \mathbf{E}_1 \rangle &= +\sin(i)\sin(\alpha) & \langle \mathbf{N}_3 \cdot \mathbf{E}_2 \rangle &= -\sin(i)\cos(\alpha) & \langle \mathbf{N}_3 \cdot \mathbf{E}_3 \rangle &= \cos(i)
\end{aligned} \tag{168}$$

The transformation from the Gauss system (vector components $a_i, i=1, \dots, 3$) into the *ECI* system (vector components $b_i, i=1, \dots, 3$) is:

$$\begin{aligned}
\begin{pmatrix} b_1 \\ b_2 \\ b_3 \end{pmatrix} &= \begin{pmatrix} \langle \mathbf{E}_1 \cdot \mathbf{N}_1 \rangle & \langle \mathbf{E}_1 \cdot \mathbf{N}_2 \rangle & \langle \mathbf{E}_1 \cdot \mathbf{N}_3 \rangle \\ \langle \mathbf{E}_2 \cdot \mathbf{N}_1 \rangle & \langle \mathbf{E}_2 \cdot \mathbf{N}_2 \rangle & \langle \mathbf{E}_2 \cdot \mathbf{N}_3 \rangle \\ \langle \mathbf{E}_3 \cdot \mathbf{N}_1 \rangle & \langle \mathbf{E}_3 \cdot \mathbf{N}_2 \rangle & \langle \mathbf{E}_3 \cdot \mathbf{N}_3 \rangle \end{pmatrix} \cdot \begin{pmatrix} a_1 \\ a_2 \\ a_3 \end{pmatrix} \\
&= \begin{pmatrix} \cos(\alpha) & -\cos(i)\sin(\alpha) & +\sin(i)\sin(\alpha) \\ \sin(\alpha) & \cos(i)\cos(\alpha) & -\sin(i)\cos(\alpha) \\ 0 & \sin(i) & \cos(i) \end{pmatrix} \cdot \begin{pmatrix} a_1 \\ a_2 \\ a_3 \end{pmatrix}
\end{aligned} \tag{169}$$

The S/C longitude at the time of the ascending equatorial crossing is:

$$\lambda_0 \equiv \lambda(t_0) = \alpha - \Theta(t_0) \tag{170}$$

where $\Theta(t_0)$ is the angle between the Greenwich meridian and the vernal equinox ([24], chapter 5.1.4).

A.5 In-Flight S/C System (F) and GMI System

Geodetic attitude (roll, pitch and yaw) specify the orientation of the actual in-flight S/C axes with respect to the nadir pointing nominal flight axes.

The attitude matrices for the 3 Euler angles roll r , pitch p and yaw y are defined as:

$$\begin{aligned}
R_x(r) &= \begin{pmatrix} 1 & 0 & 0 \\ 0 & \cos(r) & \sin(r) \\ 0 & -\sin(r) & \cos(r) \end{pmatrix} && \text{roll matrix} \\
R_y(p) &= \begin{pmatrix} \cos(p) & 0 & -\sin(p) \\ 0 & 1 & 0 \\ \sin(p) & 0 & \cos(p) \end{pmatrix} && \text{pitch matrix} \\
R_z(y) &= \begin{pmatrix} \cos(y) & \sin(y) & 0 \\ -\sin(y) & \cos(y) & 0 \\ 0 & 0 & 1 \end{pmatrix} && \text{yaw matrix}
\end{aligned} \tag{171}$$

The total attitude matrix is the product:

$$R(r, p, y) = R_x(r) \cdot R_y(p) \cdot R_z(y) \tag{172}$$

We denote the nominal (nadir pointing) S/C axes as $\mathbf{e}_i, i=1, 2, 3$ and the axes of the actual in flight S/C system (F) including roll, pitch and yaw as $\mathbf{e}'_i, i=1, 2, 3$. The coordinate transform is:

$$\langle \mathbf{e}'_j \cdot \mathbf{e}_i \rangle = R_{ji}(r, p, y) \quad i, j = 1, 2, 3 \quad (173)$$

The GMI coordinate system is defined as:

$$\mathbf{e}_1^{\text{GMI}} \equiv \mathbf{e}'_1 \quad \mathbf{e}_2^{\text{GMI}} \equiv -\mathbf{e}'_2 \quad \mathbf{e}_3^{\text{GMI}} \equiv -\mathbf{e}'_3 \quad (174)$$

In this document we will use the flight coordinate system (F) rather than the GMI system as reference frame when doing boresight geolocation.

A.6 Main Reflector Coordinate System ($MRC S$)

We first characterize the nominal definition of the $MRC S$ and we also assume that the antenna is not scanning but looking into the center of the forward swath:

The origin of the $MRC S$ is in the focal point of the antenna. The x-z plane of the $MRC S$ is the same as the x-z plane of the nominal (nadir pointing) flight coordinate system (F). The x-z axes of the $MRC S$ are obtained from the x-z axes of F by rotating counter-clockwise around the y-axis by the nominal off-nadir angle $\theta_N = 48.5^\circ$.

Let $\mathbf{e}_i, i = 1, \dots, 3$ denote the 3 Cartesian coordinate (x,y,z) unit vectors of the F system and $\mathbf{f}'_i, i = 1, \dots, 3$ denote the 3 Cartesian coordinate unit vectors of the $MRC S$. Then:

$$\begin{aligned} \mathbf{e}_1 &= \cos(\theta_N) \mathbf{f}'_1 + \sin(\theta_N) \mathbf{f}'_3 \\ \mathbf{e}_2 &= \mathbf{f}'_2 \\ \mathbf{e}_3 &= -\sin(\theta_N) \mathbf{f}'_1 + \cos(\theta_N) \mathbf{f}'_3 \end{aligned} \quad (175)$$

From this it follows that the Cartesian components $b_i, i = 1, \dots, 3$ of an arbitrary 3-vector \mathbf{b} in F system and $MRC S$ are related by:

$$b_{MRC S, i} = \langle \mathbf{f}'_i \cdot \mathbf{e}_j \rangle b_{F, j} = [r_2]_{ij} b_{F, j} \quad (176)$$

or

$$\begin{aligned} \mathbf{b}_{MRC S} &= \mathbf{r}_2(\theta_N) \cdot \mathbf{b}_F \\ \mathbf{b}_F &= \mathbf{r}_2(-\theta_N) \cdot \mathbf{b}_{MRC S} \end{aligned} \quad (177)$$

where \mathbf{r}_2 is the rotation matrix

$$\mathbf{r}_2(\theta_N) = \begin{pmatrix} \cos(\theta_N) & 0 & -\sin(\theta_N) \\ 0 & 1 & 0 \\ +\sin(\theta_N) & 0 & \cos(\theta_N) \end{pmatrix} \quad (178)$$

If the feedhorn was located at the focal point, the plane of incidence, defined as the plane between boresight vector and nadir, is the x-z plane of F . In that case the boresight direction would be aligned with the z-axis of the $MRC S$. In general, the location of the feedhorns are offset from the focal point by the off-track angles given in Table 25. That means that the planes of incidence for the feedhorns are rotated around the nadir (z-axis of F) by the corresponding values of those off-track angles.

The transformation (177)/(178) constitutes is the nominal relation between $MRC S$ and F for a non-scanning antenna. Due to various misalignments the real transformation matrix

\mathbf{r}_{F-MRCS} between *MRCS* and *F* differs slightly from its ideal value $\mathbf{r}_2(-\theta_N)$ in (178) and needs to be substituted by (BATC, GMI SER # 2351340, 1/11/ 2011):

$$\mathbf{r}_{F-MRCS} = \begin{pmatrix} +0.662996346939964 & +0.000333258340532 & -0.748622557022657 \\ -0.000736534865224 & 0.999999707306875 & -0.000207129321169 \\ +0.748622268878408 & +0.000688712597420 & +0.662996398341879 \end{pmatrix} \\ \approx \mathbf{r}_2(-\theta_N)$$

Note that this transformation matrix is universal and does not depend on the channel. It is used for both low and high frequency channels.

If the reflector is scanning then the transformation between *MRCS* and *F* involves an additional counter-clockwise rotation around the z-axis by the scan angle α_{scan} :

$$\mathbf{r}_3(\alpha_{scan}) = \begin{pmatrix} \cos(\alpha_{scan}) & +\sin(\alpha_{scan}) & 0 \\ -\sin(\alpha_{scan}) & \cos(\alpha_{scan}) & 0 \\ 0 & 0 & 1 \end{pmatrix} \quad (180)$$

bringing the full transformation between *MRCS* and *F* to:

$$\mathbf{b}_F = \mathbf{r}_3(\alpha_{scan}) \cdot \mathbf{r}_{MRCS-F} \cdot \mathbf{b}_{MRCS} \quad (181)$$

A.7 Main Beam System (*MBS*)

The z-axis of the *MBS* is pointing into the boresight direction and the x-z plane of the *MBS* contains the S/C nadir vector \mathbf{e}_3 . We denote the 3 Cartesian coordinate (x,y,z) unit vectors of the *MBS* with $\mathbf{f}_i, i = 1, \dots, 3$. The *MBS* axes are obtained from the *F* axes by 2 consecutive rotations:

1. Counter-clockwise rotation around the z-axis of *F* by the off-track angle ϕ_0 . The coordinate transformation is done by the rotation matrix:

$$\mathbf{r}_3(\phi_0) = \begin{pmatrix} \cos(\phi_0) & +\sin(\phi_0) & 0 \\ -\sin(\phi_0) & \cos(\phi_0) & 0 \\ 0 & 0 & 1 \end{pmatrix} \quad (182)$$

2. Counter-clockwise rotation around the new y-axis by the off-nadir angle θ_N . The coordinate transformation is done by the rotation matrix:

$$\mathbf{r}_2(\theta_N) = \begin{pmatrix} \cos(\theta_N) & 0 & -\sin(\theta_N) \\ 0 & 1 & 0 \\ +\sin(\theta_N) & 0 & \cos(\theta_N) \end{pmatrix} \quad (183)$$

As a consequence, the S/C nadir vector \mathbf{e}_3 has the *MBS* decomposition:

$$\mathbf{e}_3 = -\sin(\theta_N)\mathbf{f}_1 + \cos(\theta_N)\mathbf{f}_3 \quad (184)$$

The Cartesian components $b_i, i = 1, \dots, 3$ of an arbitrary 3-vector \mathbf{b} in the non-scanning *MRCS* and the *MBS* system are related by the 3 consecutive rotations:

$$\mathbf{b}_{MBS} = \mathbf{r}_2(\theta_N) \cdot \mathbf{r}_3(\phi_0) \cdot \mathbf{r}_{MRCF} \cdot \mathbf{b}_{MRCF} \quad (185)$$

If the reflector is scanning the full transformation reads:

$$\mathbf{b}_{MBS} = \mathbf{r}_2(\theta_N) \cdot \mathbf{r}_3(\phi_0) \cdot \mathbf{r}_3(\alpha_{scan}) \cdot \mathbf{r}_{MRCF} \cdot \mathbf{b}_{MRCF} \quad (186)$$

Table 25: Off-nadir angles θ_N and off-track angles ϕ_0 for the GMI channels. Taken from BATC, GMI SER # 2349971, 3/30, 2011.

Band [GHz]	10.65	18.7	23.8	36.6	89	166	183
θ_N [deg]	48.428	48.441	48.447	48.473	48.463	45.282	45.277
ϕ_0 [deg]	+9.717	+4.091	+4.116	-2.315	+0.736	+2.330	+0.036

Table 25 shows the values for the off-nadir angles θ_N and the off-track angles ϕ_0 for the various GMI channels.

Appendix B Geolocation

The boresight unit vector $\mathbf{b}_0 \equiv b_1\mathbf{E}_1 + b_2\mathbf{E}_2 + b_3\mathbf{E}_3$ pointing from S/C to the Earth cell has the following components in the F system:

$$\mathbf{b}_0 = \sin(\theta_N) \cdot \cos(\omega) \cdot \mathbf{e}_1 - \sin(\theta_N) \cdot \sin(\omega) \cdot \mathbf{e}_2 + \cos(\theta_N) \cdot \mathbf{e}_3 \quad (187)$$

where θ_N , is the boresight nadir angle of the feedhorn and ω is the boresight looking azimuth (scan angle). As defined, $\omega = 0$ means that the instrument looks forward, $\omega > 0$ means that the instrument looks left of forward and $\omega < 0$ means that the instrument looks right of forward. The value of ω can be calculated from the basic input parameters that were specified in section 5.1. If, for a given channel, ω_0 is the azimuth offset at the beginning of the Earth view, n_{Earth} the number of earth view samples, τ_{int} the integration time and Δt_{scan} the duration of the scan, then the looking azimuth $\omega(i)$ for Earth view sample $i = 1, \dots, n_{Earth}$ is:

$$\omega(i) = \omega_0 + (i-1) \cdot \frac{\tau_{int}}{\Delta t_{scan}} \cdot \frac{360^\circ}{n_{Earth}} \quad (188)$$

Using the coordinate transformation procedure from Appendix A we can transform \mathbf{b}_0 into the ECI system.

The coordinate vector \mathbf{R}_E of the boresight-Earth intersection point in the ECI system is:

$$\mathbf{R}_E = \begin{pmatrix} \left[\frac{\rho_e}{\sqrt{1 - \varepsilon^2 \sin^2(\Theta_E)}} \right] \cos(\Theta_E) \cos(\Phi_E) \\ \left[\frac{\rho_e}{\sqrt{1 - \varepsilon^2 \sin^2(\Theta_E)}} \right] \cos(\Theta_E) \sin(\Phi_E) \\ \left[\frac{\rho_e (1 - \varepsilon^2)}{\sqrt{1 - \varepsilon^2 \sin^2(\Theta_E)}} \right] \sin(\Theta_E) \end{pmatrix} \quad (189)$$

Θ_E and λ_E are geodetic latitude and longitude of the Earth observation cell, respectively, and $\Phi_E = \lambda_E + \Theta(t)$. The Cartesian components $R_{Ei} = \langle \mathbf{R}_E \cdot \mathbf{E}_i \rangle$, $i = 1, 2, 3$ fulfill the geoid equation:

$$\frac{R_{E1}^2 + R_{E2}^2}{\rho_e^2} + \frac{R_{E3}^2}{\rho_p^2} = 1 \quad (190)$$

They can be computed from:

$$\mathbf{R}_E = \mathbf{R}_{S/C} + \eta \cdot \mathbf{b}_0 \quad (191)$$

where:

$$\eta = R_{S/C} \cdot \left[B - \sqrt{B^2 - C} \right] \quad (192)$$

is the range distance from the S/C to the Earth cell and in order to have an intersection with the Earth, it must be $\eta > 0$. Furthermore:

$$B = -\frac{r_1 b_1 + r_2 b_2 + \left(\frac{\rho_e}{\rho_p}\right)^2 r_3 b_3}{1 + \left[\left(\frac{\rho_e}{\rho_p}\right)^2 - 1\right] b_3^2} \quad C = \frac{1 - \left(\frac{\rho_e}{r}\right)^2 + \left[\left(\frac{\rho_e}{\rho_p}\right)^2 - 1\right] b_3^2}{1 + \left[\left(\frac{\rho_e}{\rho_p}\right)^2 - 1\right] b_3^2} \quad (193)$$

where the $r_i, i = 1, \dots, 3$ were defined in (159).

At the boresight-Earth intersection point, we can form a local coordinate system $\{\mathbf{S}, \mathbf{E}, \mathbf{U}\}$ consisting of:

1. The surface normal \mathbf{U} pointing upward from the Earth.
2. The vector \mathbf{S} pointing N to S along the local meridian.
3. The vector \mathbf{E} pointing locally E parallel to the equator.

The components of $\{\mathbf{S}, \mathbf{E}, \mathbf{U}\}$ in the $\{\mathbf{E}_1, \mathbf{E}_2, \mathbf{E}_3\}$ system are:

$$\begin{aligned} \mathbf{U} &= \cos(\Theta_E) \cos(\Phi_E) \mathbf{E}_1 + \cos(\Theta_E) \sin(\Phi_E) \mathbf{E}_2 + \sin(\Theta_E) \mathbf{E}_3 \\ \hat{\mathbf{E}} &= -\sin(\Phi_E) \mathbf{E}_1 + \cos(\Phi_E) \mathbf{E}_2 \\ \mathbf{S} &= \mathbf{E} \times \mathbf{U} \end{aligned} \quad (194)$$

The components of \mathbf{b}_0 in the $\{\mathbf{S}, \mathbf{E}, \mathbf{U}\}$ system are:

$$\mathbf{b}_0 = -\sin(\theta) \cdot \cos(\alpha) \cdot \mathbf{S} + \sin(\theta) \cdot \sin(\alpha) \cdot \mathbf{E} - \cos(\theta) \cdot \mathbf{U} \quad (195)$$

where θ is the Earth incidence angle (EIA) and α is the looking azimuth relative to N.

Appendix C Optimum Interpolation and Near-Sidelobe Corrections

C.1 Optimum Interpolation

The Optimum Interpolation (OI) technique for imaging microwave radiometer data is an application of the Backus-Gilbert method of image reconstruction and was developed by [30] based on earlier studies by [31].

The general problem is the following:

We consider an antenna that is taking spatial samples at a rate that is at least twice the spatial frequency response (*Nyquist* rate). If the spatial frequency response is characterized by the 3-dB footprint size L [in km], then the samples need to be taken every $L/2$ km or more.

The antenna temperature T_A for a specific channel that is received by a microwave radiometer coming from an individual field of view (IFOV) observation cell at Earth location \mathbf{r} can be written as the area integral over the brightness temperatures T_B weighted by an antenna gain pattern kernel function G within the whole IFOV:

$$T_A(\mathbf{r}) = \int dx' dy' G(\mathbf{r}, \mathbf{r}') \cdot T_B(\mathbf{r}') \quad (196)$$

$$\mathbf{r} = \begin{pmatrix} x \\ y \end{pmatrix} \quad \mathbf{r}' = \begin{pmatrix} x' \\ y' \end{pmatrix}$$

For simplicity we have assumed that there is no contribution from cross polarization. The removal of cross polarization contamination is effectively handled during the antenna pattern correction (chapter 9). The gain pattern $G(\mathbf{r}, \mathbf{r}')$ is normalized:

$$\int dx' dy' G(\mathbf{r}, \mathbf{r}') = 1 \quad (197)$$

Assume that we have a set of N antenna temperature measurements at cell positions \mathbf{r}_i : $T_A(\mathbf{r}_i)$, $i = 1, \dots, N$ that are all given by gain integrals of the form (196). The goal of the OI is to reconstruct the antenna temperature of a target cell at location \mathbf{r}_t :

$$T_A(\mathbf{r}_t) = \int dx' dy' G(\mathbf{r}_t, \mathbf{r}') \cdot T_B(\mathbf{r}') \quad (198)$$

with

$$\int dx' dy' G(\mathbf{r}_t, \mathbf{r}') = 1 \quad (199)$$

as weighted average over the measurements $T_A(\mathbf{r}_i)$, $i = 1, \dots, N$:

$$\tilde{T}_A(\mathbf{r}_t) = \sum_{i=1}^N a_i \cdot T_A(\mathbf{r}_i) \quad (200)$$

Using (196) one can write (200) in the form:

$$\tilde{T}_A(\mathbf{r}_t) = \int dx' dy' \bar{G}_t(\mathbf{r}_t, \mathbf{r}') \cdot T_B(\mathbf{r}') \quad (201)$$

with:

$$\bar{G}_t(\mathbf{r}_t, \mathbf{r}') = \sum_{i=1}^N a_i \cdot G(\mathbf{r}_i, \mathbf{r}') \quad (202)$$

$\tilde{T}_A(\mathbf{r}_t)$ is an estimate for the true value $T_A(\mathbf{r}_t)$. The normalization condition (199) implies that also

$$\int dx' dy' \bar{G}_t(\mathbf{r}_t, \mathbf{r}') = 1 \quad (203)$$

which demands that all the weights a_i must sum up to 1:

$$\sum_{i=1}^N a_i = 1 \quad (204)$$

The error of estimating $T_A(\mathbf{r}_t)$ by $\tilde{T}_A(\mathbf{r}_t)$ is:

$$\Delta = \int dx' dy' [G(\mathbf{r}_t, \mathbf{r}') - \bar{G}_t(\mathbf{r}_t, \mathbf{r}')] \cdot T_B(\mathbf{r}') \quad (205)$$

For the special case that one of the grid cells is equal to the target cell $i = t$, the error Δ vanishes if $a_{i=t} = 1$ and $a_i = 0$ otherwise.

In the following we treat the microwave emission as homogenous random process with uniform spectral power density[32]. That means:

$$T_B(\mathbf{r}) = \langle T_B \rangle + \delta T_B(\mathbf{r}) \quad (206)$$

The spectral decomposition of the random fluctuation $\delta T_B(\mathbf{r})$ is:

$$\delta T_B(\mathbf{r}) = \int dk_x dk_y e^{i(k_x x + k_y y)} f(k_x, k_y) = \int d^2 \mathbf{k} e^{i\mathbf{k} \cdot \mathbf{r}} f(\mathbf{k}) = \int d^2 \mathbf{k} e^{-i\mathbf{k} \cdot \mathbf{r}} f^*(\mathbf{k}) \quad (207)$$

where f^* denotes the complex conjugate and $f^*(\mathbf{k}) = f(-\mathbf{k})$. In (207) we have used the fact that $\delta T_B(\mathbf{r})$ is real. The ensemble average $\langle \dots \rangle$ over the fluctuation vanishes, i.e.:

$$\langle \delta T_B(\mathbf{r}) \rangle = 0 \quad (208)$$

and therefore also

$$\langle f(\mathbf{k}) \rangle = 0 \quad (209)$$

The correlator of the fluctuations does not vanish. The homogeneity condition means:

$$\begin{aligned} \langle f(\mathbf{k}) \cdot f^*(\mathbf{k}') \rangle &= \delta^{(2)}(\mathbf{k} - \mathbf{k}') \cdot F^2 \\ \langle \delta T_B(\mathbf{r}) \cdot \delta T_B(\mathbf{r}') \rangle &= \int d^2 \mathbf{k} d^2 \mathbf{k}' e^{i(\mathbf{k} \cdot \mathbf{r} - \mathbf{k}' \cdot \mathbf{r}')} \langle f(\mathbf{k}) \cdot f^*(\mathbf{k}') \rangle = (2\pi)^2 \delta^{(2)}(\mathbf{r} - \mathbf{r}') \cdot F^2 \end{aligned} \quad (210)$$

where F is constant. Taking the expectation value of Δ^2 in (205) gives:

$$\begin{aligned}
\langle \Delta^2 \rangle &= \left\langle \left[\int dx' dy' [G(\mathbf{r}_i, \mathbf{r}') - \bar{G}_i(\mathbf{r}_i, \mathbf{r}')] \cdot T_B(\mathbf{r}') \right]^2 \right\rangle = \\
& \left\langle \left[\int dx' dy' [G(\mathbf{r}_i, \mathbf{r}') - \bar{G}_i(\mathbf{r}_i, \mathbf{r}')] \cdot [\langle T_B \rangle + \delta T_B(\mathbf{r}')] \right]^2 \right\rangle = \\
& \langle T_B \rangle^2 \cdot \int dx' dy' [G(\mathbf{r}_i, \mathbf{r}') - \bar{G}_i(\mathbf{r}_i, \mathbf{r}')] \cdot \int dx' dy' [G(\mathbf{r}_i, \mathbf{r}') - \bar{G}_i(\mathbf{r}_i, \mathbf{r}')] + \\
& 2 \cdot \langle T_B \rangle \cdot \left[\int dx' dy' [G(\mathbf{r}_i, \mathbf{r}') - \bar{G}_i(\mathbf{r}_i, \mathbf{r}')] \right] \cdot \left[\int dx' dy' [G(\mathbf{r}_i, \mathbf{r}') - \bar{G}_i(\mathbf{r}_i, \mathbf{r}')] \cdot \langle \delta T_B(\mathbf{r}') \rangle \right] + \\
& \int dx' dy' dx'' dy'' [G(\mathbf{r}_i, \mathbf{r}') - \bar{G}_i(\mathbf{r}_i, \mathbf{r}')] [G(\mathbf{r}_i, \mathbf{r}'') - \bar{G}_i(\mathbf{r}_i, \mathbf{r}'')] \cdot \langle \delta T_B(\mathbf{r}') \cdot \delta T_B(\mathbf{r}'') \rangle
\end{aligned} \tag{211}$$

The first term in the sum of (211) vanishes because of the normalization conditions (199) and (203). The second term vanishes because of the same reason and also because of (208). Using (210), the remaining third term can be written as:

$$\langle \Delta^2 \rangle = (2\pi)^2 \cdot F^2 \cdot \int dx' dy' [G(\mathbf{r}_i, \mathbf{r}') - \bar{G}_i(\mathbf{r}_i, \mathbf{r}')]^2 \tag{212}$$

The OI can be regarded as maximum likelihood estimator (MLE) for Δ^2 , that means it tries to find weights $a_i, i = 1, \dots, N$ which minimize the expression

$$Q[a_i] = \int dx' dy' [G(\mathbf{r}_i, \mathbf{r}') - \bar{G}_i(\mathbf{r}_i, \mathbf{r}')]^2 \tag{213}$$

while satisfying the constraint (204).

Substituting (202) into (213) gives:

$$\begin{aligned}
Q[a_i] &= \\
& \int dx' dy' [G(\mathbf{r}_i, \mathbf{r}')]^2 \\
& - 2 \cdot \sum_{i=1}^N a_i \cdot \int dx' dy' [G(\mathbf{r}_i, \mathbf{r}') \cdot G(\mathbf{r}_i, \mathbf{r}')] + \sum_{i,j=1}^N a_i \cdot a_j \cdot \int dx' dy' [G(\mathbf{r}_i, \mathbf{r}') \cdot G(\mathbf{r}_j, \mathbf{r}')]
\end{aligned} \tag{214}$$

The first term in (214) does not depend on the a_i and does therefore not influence the OI solution. As abbreviations we introduce the gain overlap matrix \mathbf{g}_{ij} between the interpolating cells and the overlap \mathbf{v}_i between the interpolating cells and the target cell:

$$\begin{aligned}
\mathbf{g}_{ij} &\equiv \int dx' dy' [G(\mathbf{r}_i, \mathbf{r}') \cdot G(\mathbf{r}_j, \mathbf{r}')] \\
\mathbf{v}_i &\equiv \int dx' dy' [G(\mathbf{r}_i, \mathbf{r}') \cdot G(\mathbf{r}_i, \mathbf{r}')]
\end{aligned} \tag{215}$$

We also order the parameters $a_i, i = 1, \dots, N$ in form of a column vector $\mathbf{a} \equiv \begin{pmatrix} a_1 \\ \vdots \\ a_n \end{pmatrix}$ or its

transposed $\mathbf{a}^T = (a_1, \dots, a_n)$ and introduce the abbreviation:

$$\mathbf{u}_i \equiv \int dx' dy' G(\mathbf{r}_i, \mathbf{r}') = 1 \tag{216}$$

The OI can then compactly be written as minimizing the expression:

$$h[\mathbf{a}] \equiv \mathbf{a}^T \cdot \mathbf{g} \cdot \mathbf{a} - 2 \cdot \mathbf{v}^T \cdot \mathbf{a} = \mathbf{a}^T \cdot \mathbf{g} \cdot \mathbf{a} - 2 \cdot \mathbf{a}^T \cdot \mathbf{v} \tag{217}$$

under the constraint

$$f[\mathbf{a}] \equiv \mathbf{u}^T \cdot \mathbf{a} - 1 = \mathbf{a}^T \cdot \mathbf{u} - 1 = 0 \quad (218)$$

The optimization problem can be solved by using the Euler-Lagrange technique. Introducing the Lagrange multiplier λ the condition for minimizing (217) under the constraint (218) is:

$$\frac{dh[\mathbf{a}]}{da_k} = \lambda \cdot \frac{df[a]}{da_k}, \quad k = 1, \dots, N \quad (219)$$

Writing out (219) leads to:

$$2 \cdot (\mathbf{g} \cdot \mathbf{a} - \mathbf{v}) = \lambda \mathbf{u} \quad (220)$$

The condition for the Lagrange multiplier λ can be derived from (220) by multiplying the whole equation with \mathbf{a}^T from the left and using (218):

$$\lambda = 2 \cdot (\mathbf{a}^T \cdot \mathbf{g} \cdot \mathbf{a} - \mathbf{v}^T \cdot \mathbf{a}) \quad (221)$$

Substituting (221) into (220) gives:

$$(\mathbf{g} \cdot \mathbf{a} - \mathbf{v}) = [\mathbf{a}^T \cdot \mathbf{g} \cdot \mathbf{a} - \mathbf{a}^T \cdot \mathbf{v}] \mathbf{u} = [\mathbf{a}^T \cdot (\mathbf{g} \cdot \mathbf{a} - \mathbf{v})] \mathbf{u} = [(\mathbf{g} \cdot \mathbf{a} - \mathbf{v})^T \cdot \mathbf{a}] \mathbf{u} \quad (222)$$

and

$$\mathbf{a} = [\mathbf{a}^T \cdot (\mathbf{g} \cdot \mathbf{a} - \mathbf{v})] \cdot [\mathbf{g}^{-1} \cdot \mathbf{u}] + \mathbf{g}^{-1} \cdot \mathbf{v} \quad (223)$$

Where \mathbf{g}^{-1} is the inverse matrix to \mathbf{g} . We abbreviate:

$$\mathbf{b} \equiv (\mathbf{g} \cdot \mathbf{a} - \mathbf{v}) \quad (224)$$

Then (222) becomes

$$\mathbf{b} = [\mathbf{b}^T \cdot \mathbf{a}] \mathbf{u} \quad (225)$$

and (223) becomes:

$$\mathbf{a} = \mathbf{g}^{-1} \cdot \mathbf{v} + [\mathbf{a}^T \cdot \mathbf{b}] \cdot [\mathbf{g}^{-1} \cdot \mathbf{u}] = \mathbf{g}^{-1} \cdot \mathbf{v} + [\mathbf{b}^T \cdot \mathbf{a}] \cdot [\mathbf{g}^{-1} \cdot \mathbf{u}] \quad (226)$$

Multiplying equation (226) with \mathbf{b}^T from the left and using (225) gives:

$$\begin{aligned} [\mathbf{b}^T \cdot \mathbf{a}] &= \mathbf{b}^T \cdot \mathbf{g}^{-1} \cdot \mathbf{v} + [\mathbf{b}^T \cdot \mathbf{a}] \cdot [\mathbf{b}^T \cdot \mathbf{g}^{-1} \cdot \mathbf{u}] \\ [\mathbf{b}^T \cdot \mathbf{a}] &= \frac{\mathbf{b}^T \cdot \mathbf{g}^{-1} \cdot \mathbf{v}}{1 - [\mathbf{b}^T \cdot \mathbf{g}^{-1} \cdot \mathbf{u}]} = \frac{[\mathbf{b}^T \cdot \mathbf{a}] \cdot [\mathbf{u}^T \cdot \mathbf{g}^{-1} \cdot \mathbf{v}]}{1 - [\mathbf{b}^T \cdot \mathbf{a}] \cdot [\mathbf{u}^T \cdot \mathbf{g}^{-1} \cdot \mathbf{u}]} \\ 1 - [\mathbf{b}^T \cdot \mathbf{a}] \cdot [\mathbf{u}^T \cdot \mathbf{g}^{-1} \cdot \mathbf{u}] &= [\mathbf{u}^T \cdot \mathbf{g}^{-1} \cdot \mathbf{v}] \\ [\mathbf{b}^T \cdot \mathbf{a}] &= \frac{1 - [\mathbf{u}^T \cdot \mathbf{g}^{-1} \cdot \mathbf{v}]}{[\mathbf{u}^T \cdot \mathbf{g}^{-1} \cdot \mathbf{u}]} \end{aligned} \quad (227)$$

Substituting (227) back into (226) leads to the final solution for the OI weights

$\mathbf{a}_i, i = 1 \dots N$:

$$\mathbf{a} = \mathbf{g}^{-1} \cdot \left[\mathbf{v} + \frac{1 - [\mathbf{u}^T \cdot \mathbf{g}^{-1} \cdot \mathbf{v}]}{[\mathbf{u}^T \cdot \mathbf{g}^{-1} \cdot \mathbf{u}]} \mathbf{u} \right]$$

with the components:

$$\mathbf{u}_i \equiv \int dx' dy' G(\mathbf{r}_i, \mathbf{r}') = 1 \quad (228)$$

$$\mathbf{v}_i \equiv \int dx' dy' [G(\mathbf{r}_i, \mathbf{r}') \cdot G(\mathbf{r}_i, \mathbf{r}')]]$$

$$\mathbf{g}_{ij} \equiv \int dx' dy' [G(\mathbf{r}_i, \mathbf{r}') \cdot G(\mathbf{r}_j, \mathbf{r}')]]$$

$$i = 1, \dots, N$$

C.2 Resampling and Composite Field of View

The OI method is used during Level-2 processing for resampling the individual radiometer observations onto composite field of views (CFOV) cells. The resampling saves two purposes:

1. Averaging multiple finely sampled high resolution IFOV observations to lower resolution CFOV footprints with less noise. Assuming that the noise of each IFOV is σ_{IFOV} , then it follows from equation that the noise of the CFOV σ_{CFOV} is:

$$\sigma_{CFOV}^2 = \left(\sum_{i=1}^N a_i^2 \right) \cdot \sigma_{IFOV}^2 \quad (229)$$

Therefore the resampling noise reduction factor (NRF) is $\sqrt{\sum_{i=1}^N a_i^2}$. Generally, there is a tradeoff between noise reduction and resolution. The best noise reduction or smallest NRF in (229) that satisfies the normalization condition (204) is obtained if all weights $a_i = \frac{1}{N}$. This solution applies to the special case that all $i = 1, \dots, N$ interpolation are identical to the target cell t . In that case, we recover the standard noise reduction for N independent measurements $\sigma_{CFOV} = \frac{\sigma_{IFOV}}{\sqrt{N}}$. For the general case the OI is designed to find the best configuration for the weights a_i that simultaneously minimizes the NRF and maximizes resolution. The weights found by the OI are in general different than the simple $a_i = \frac{1}{N}$ weights, as the equal weighting does not result in the optimal resolution. As a general rule, the finer the sampling of the IFOV, the more effective the OI method can be in finding a solution with low NRF. Frequently, the numerical result of the OI method results in values for the a_i that are relatively large and negative and therefore the NRF is also relatively large. However, a combination for the a_i with smaller NRF but only slightly worse resolution might exist. One way, to force the OI method to find this solution is to apply a smoothing to the gain overlap matrix \mathbf{g}_{ij} and substitute the \mathbf{g}_{ij} in equation (228) by $\mathbf{g}_{ij} \rightarrow \mathbf{g}_{ij} + \beta \cdot \delta_{ij}$, where δ_{ij} denotes the $N \times N$ unit matrix and β is a smoothing factor.

2. The CFOV of all channels are shifted to a common location. This is necessary, because geophysical retrieval algorithms generally require input brightness temperatures from several channels at the same location on the Earth. For SSM/I, SSMI, TMI and AMSR the higher resolutions are resampled to the lower resolution and the cells are shifted to the location of the higher resolution. As an example AMSR Level-2 products are produced on 4 different resolutions:

a. Very low resolution: The 7, 10, 18, 23 and 37 GHz IFOV are resampled to the resolution of the 7 GHz 3-dB footprint and the CFOV are shifted to the locations of the 37 GHz observations.

b. Low resolution: The 10, 18, 23 and 37 GHz IFOV are resampled to the resolution of the 10 GHz 3-dB footprint and the CFOV are shifted to the locations of the 37 GHz observations.

c. Medium resolution: The 18, 23 and 37 GHz IFOV are resampled to the resolution of the 18 GHz 3-dB footprint and the CFOV are shifted to the locations of the 37 GHz observations.

d. High resolution: The 37 GHz IFOV are kept at their original resolution and locations.

For WindSat the Level 2 products are also produced at these 4 resolutions. However, all observations are resampled onto a fixed $1/8^\circ$ by $1/8^\circ$ latitudinal – longitudinal Earth grid, because of the complicated geometry of the WindSat swath, which involves different scan arcs for the 5 frequencies and observations from both forward and backward looks. An example is shown in Figure 30.

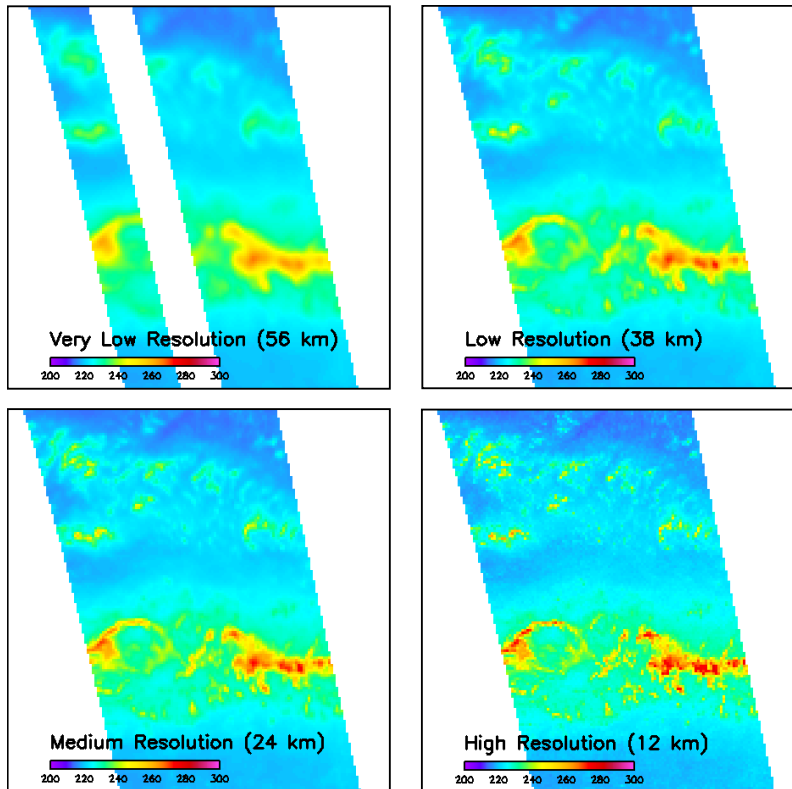


Figure 30: WindSat Level 2 brightness temperatures for the 37V channel at 4 different resolutions. The figure shows a rain band in the ITCZ just north of the equator in the central Pacific in December. The missing part on the swath of the 56 km is due to the fact that there are no 6.8 GHz observations and for producing the figures all channels at a given resolution were required.

C.3 Near-Sidelobe Corrections

The OI method could also be applied to remove contributions from near sidelobes from the IFOV. At each IFOV cell observations from the surrounding cells are resampled onto the area of the main beam, which is defined as the area between the first minima in the antenna pattern gain functions. As a result, one can correct for contaminations of the near-sidelobes into the main beam, which occur if the cell is near a geographical interface (e.g. ocean – land, rain – rain free, cloud – cloud free). This is done for each individual channel and each IFOV cell. We expect that some of the resampling weights a_i will be negative resulting in a larger NRF in favor of a resolution enhancement when compared with the method of the last section. Actually the resampling could even result in a NRF that is larger than 1.

For GMI only channels 1-7 (10.7 – 37.0 GHz) are at least Nyquist sampled and therefore the method cannot be used for the higher frequency channels 8 -13 (89 – 183 GHz). On the other hand, the 10.7 GHz observations are strongly oversampled and in that case we expect that the method would work most effectively. That is of course also the case where those corrections would be most important, as the 10.7 GHz horn has the smallest beam efficiency.

Appendix D Planck Function, Rayleigh–Jeans Approximation and Effective Cold Space Temperatures

The basic quantity which is intended to be measured by a microwave radiometer is power of electromagnetic radiation at the top of the atmosphere. For historic reasons, it is common in microwave physics to work in terms of brightness temperatures (TB) instead of the power, though in principle it would be as easy to work in terms of power rather than TB. The relationship between power and temperature is given by Planck's law and the use of TB instead of power is justified by using the Rayleigh-Jeans (RJ) approximation to the correct Planck law. The RJ approximation is justified in the microwave region for most cases. However, when dealing with radiation from cold space, it breaks down. This problem can be fixed, by using an effective cold space brightness temperature $T_c(\nu)$, which is higher than the physical cold space temperature $T_{c_0} = 2.73K$ and depends on the frequency ν of the radiation.

In this appendix we exhibit the relation between power and TB using the RJ approximation to Planck's law and derive the values of $T_c(\nu)$ from the GMI frequencies.

The power of electromagnetic radiation with polarization $p=1,2$ in the frequency interval $d\nu$ that is emitted by the surface area dA of a body at physical temperature T into the direction of the solid angle $d\Omega = \sin(\theta) d\theta d\phi$ is given by Planck's law [32]:

$$\begin{aligned} dP_p(\nu, T) &= \frac{1}{2} \varepsilon_p(\nu, T, \dots) \cdot B(\nu, T) \cos(\theta) d\Omega dA d\nu \\ &= \frac{1}{2} \varepsilon_p(\nu, T, \dots) \cdot \frac{2h}{c^2} \frac{\nu^3}{e^{h\nu/kT} - 1} \cos(\theta) d\Omega dA d\nu \end{aligned} \quad (230)$$

$\varepsilon_p(\nu, T, \dots)$ is the emissivity of the body at polarization p , which is $\varepsilon_p \equiv 1$ for a black body. $h = 6.626176 \cdot 10^{-34}$ Joule \cdot s is Planck's constant and $k = 1.38066 \frac{\text{Joule}}{\text{Kelvin}}$ is Boltz-

mann's constant. The quantity $B(\nu, T) = \frac{2h}{c^2} \frac{\nu^3}{e^{h\nu/kT} - 1}$ is often called spectral brightness

and has dimensions $\frac{\text{Watt}}{\text{m}^2 \cdot \text{steradian} \cdot \text{Hz}}$. For the following it will be convenient to work

instead with the scaled quantity:

$$\Theta(\nu, T) \equiv \frac{c^2}{2k\nu^2} B(\nu, T) = \frac{1}{k} \frac{h\nu}{e^{h\nu/kT} - 1} \quad (231)$$

which we will call the *Planck brightness temperature (TB)*, as it has the dimension of temperature.

The expansion of $\Theta(\nu, T)$ of (231) as function of the dimensionless parameter $\frac{h\nu}{kT}$ up to second order reads:

$$\Theta(\nu, T) = \frac{1}{k} \frac{h\nu}{e^{h\nu/kT} - 1} = T - \frac{1}{2} \frac{h\nu}{k} + \frac{1}{12} \left(\frac{h\nu}{k} \right) \frac{h\nu}{kT} \pm \dots \quad (232)$$

The Rayleigh-Jeans (RJ) approximation to the Planck law is the truncation (232) at 0th order is $\Theta(\nu, T) = T$, which means that the Planck TB is equal to the physical temperature of the black body.

Figure 31 shows the difference $\delta = \Theta - T$ between the full Planck brightness temperature Θ and the RJ approximation, which is the physical temperature T .

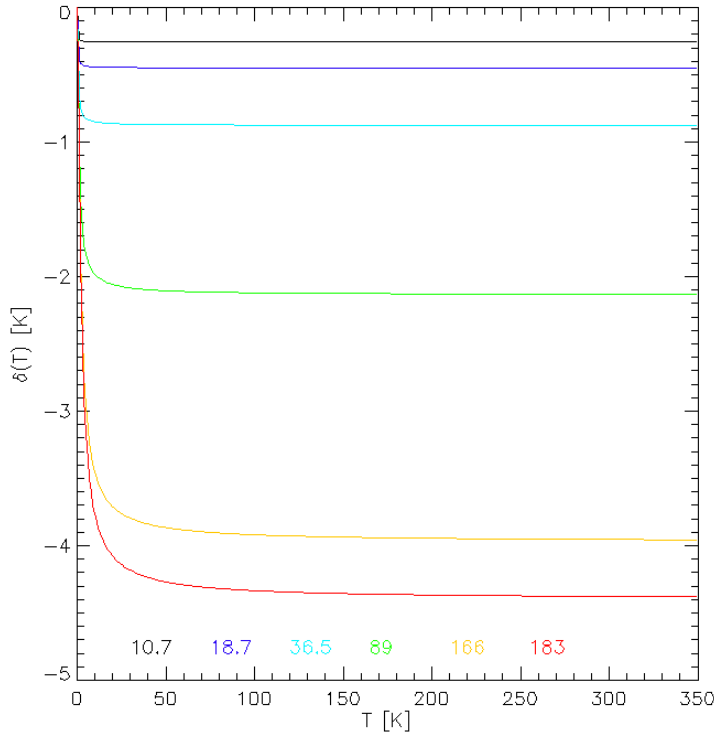


Figure 31: Deviation $\delta = \Theta - T$ of the Planck Brightness Temperature Θ (231) from the physical temperature T (RJ approximation) for the GMI frequencies.

If the physical temperature T becomes large, the deviation δ between the correct Planck law and the RJ approximation goes asymptotical to $\delta_\infty \equiv -\frac{1}{2} \frac{h\nu}{k}$, which is the next to

leading order (NLO) term in the expansion (232) and which is independent of temperature. In some sense this term acts like a constant (temperature independent) background power. As it is evident from Figure 31 this NLO to the RJ approximation is actually significant even at the lower frequency channels. In any radiative and radiometric transfer calculation, even at microwave frequencies, one should actually use the Planck TB Θ rather than the physical temperature or RJ TB T , which could be easily done. It is mainly for historic reasons that the RJ approximation is widely used. For most temperatures (atmospheric, surface, radiometric) that occur in practice, the deviation from the RJ law has reached its asymptotic limit $\delta(T) \approx \delta_\infty$ and does therefore not depend on T any more.

As we will explain in the following, this leads to cancellations in the radiative transfer equations under consideration, which simplifies those equations considerably and therefore the RJ approximation becomes useful. At 10.7 GHz the low end of the radiometric temperature range is about 80 K for which the value of δ differs from δ_∞ by less than $3 \cdot 10^{-4}$ K. At 183 GHz the series (232) converges slower for a given value of T , however the low end of the radiometric temperature range is also much larger, about 220 K, for

which δ and δ_∞ deviate still by less than 0.03 K. The only exception occurs if the radiation comes from cold space ($T_{c0} = 2.73$ K), for which even the NLO to the RJ approximation breaks down, as it becomes obvious from Figure 31.

In the following we will now discuss the most important cases including the handling of the cold space radiation within the RJ approximation:

1. Radiometric Transfer Function (Equation (8)):

In terms of the Planck TB this equation should be written as:

$$\begin{aligned}\Theta_{A,scene} &= x \Theta(T_h) + (1-x) \Theta(T_{c0}) - 4\Theta_{nl}x(1-x) \\ &= \Theta(T_{c0}) + x \cdot (\Theta(T_h) - \Theta(T_{c0})) - 4\Theta_{nl}x(1-x)\end{aligned}\quad (233)$$

We set $\Theta_{nl} = T_{nl}$, which becomes simply a definition of the non-linearity T_{nl} . Substituting the definition $\Theta = T + \delta$ in (233) leads to:

$$\begin{aligned}T_{A,scene} &= [T_{c0} + x \cdot (T_h - T_{c0}) - 4T_{nl}x(1-x)] + [\delta(T_{c0}) - \delta(T_{A,scene}) + x \cdot (\delta(T_h) - \delta(T_{c0}))] \\ &= [T_{c0} + \delta(T_{c0}) - \delta(T_{A,scene})] + x \cdot (T_h - [T_{c0} + \delta(T_{c0}) - \delta(T_h)]) - 4T_{nl}x(1-x)\end{aligned}\quad (234)$$

We now assume that for both $T_{A,scene}$ and T_h the deviation from the RJ approximation has reached the asymptotic limit δ_∞ which is independent on T , that means:

$$\delta(T_{A,scene}) \approx \delta(T_h) \approx \delta_\infty = -\frac{hv}{2k}\quad (235)$$

Then (234) can be rewritten as:

$$T_{A,scene} = T_c + x \cdot (T_h - T_c) - 4T_{nl}x(1-x)\quad (236)$$

where T_c is an effective cold space temperature accounting for the deviation of the RJ approximation from the Planck law and is given by:

$$T_c \equiv T_{c0} + \delta(T_{c0}) - \delta_\infty = \Theta(T_{c0}) - \delta_\infty = \frac{1}{k} \frac{hv}{e^{hv/kT_{c0}} - 1} + \frac{hv}{2k} = \frac{hv}{2k} \cdot \left(\frac{e^{hv/kT_{c0}} + 1}{e^{hv/kT_{c0}} - 1} \right)\quad (237)$$

The values of T_c for the GMI frequencies from (237) are listed in Table 26.

Table 26: Values for the effective temperature of cold space accounting for the deviation of the RJ approximation from the Planck law for the GMI frequencies.

Frequency [GHz]	10.65	18.7	23.8	36.64	89.0	166.5	183.31
T_c [Kelvin]	2.74	2.75	2.77	2.82	3.27	4.43	4.76

2. Spillover Correction (Cold Space Intrusion into the Earth View)

The expression for the antenna temperature (113), correctly written in terms of Planck temperatures, reads:

$$\Theta(T_A) = (1-\eta) \cdot \Theta(\tilde{T}_A) + \eta \cdot \Theta(T_{c0}) \quad (238)$$

Substituting again the decomposition $\Theta(T) = T + \delta(T)$, (238) becomes:

$$\begin{aligned} [T_A + \delta(T_A)] &= (1-\eta) \cdot [\tilde{T}_A + \delta(\tilde{T}_A)] + \eta \cdot [T_{c0} + \delta(T_{c0})] \\ T_A &= (1-\eta) \cdot \tilde{T}_A + \eta \cdot [T_{c0} + \delta(T_{c0}) - \delta(\tilde{T}_A)] + [\delta(\tilde{T}_A) - \delta(T_A)] \end{aligned} \quad (239)$$

Assuming the asymptotic limits:

$$\delta(\tilde{T}_A) \approx \delta(T_A) \approx \delta_\infty \quad (240)$$

equation (239) simplifies to the form (113) with the an effective cold space temperature T_c , that is given by (237).

3. Earth Intrusion into the Cold Mirror

Equation (144), correctly written in terms of Planck temperatures, reads:

$$\Theta(T_c(X_E)) = (1-\lambda) \cdot \Theta(T_{c0}) + \lambda \cdot \Theta(T_{B,E}(X_E)) \quad (241)$$

We again substitute the corresponding decomposition $\Theta(T) = T + \delta(T)$ and the asymptotic form $\delta(T_{B,E}(X_E)) \approx \delta_\infty$:

$$\begin{aligned} T_c(X_E) + \delta(T_c(X_E)) &= (1-\lambda) \cdot [T_{c0} + \delta(T_{c0})] + \lambda \cdot [T_{B,E}(X_E) + \delta(T_{B,E}(X_E))] \\ T_c(X_E) + \delta(T_c(X_E)) &= (1-\lambda) \cdot [T_{c0} + \delta(T_{c0})] + \lambda \cdot [T_{B,E}(X_E) + \delta_\infty] \\ [T_c(X_E) + \delta(T_c(X_E)) - \delta_\infty] &= (1-\lambda) \cdot [T_{c0} + \delta(T_{c0}) - \delta_\infty] + \lambda \cdot T_{B,E}(X_E) \end{aligned} \quad (242)$$

Comparing with (237) we see that $T_c = [T_{c0} + \delta(T_{c0}) - \delta_\infty]$ is the effective cold space temperature without Earth intrusion whereas $[T_c(X_E) + \delta(T_c(X_E)) - \delta_\infty]$ is the effective cold space temperature with Earth intrusion and (144) is recovered.

4. Radiative Transfer Equation

The argument for the radiative transfer equation (103) is very similar. We list the basic steps:

$$\Theta(T_B) = \Theta_U + \tau \cdot E \cdot \Theta(T_S) + \tau \cdot R \cdot (1+\Omega) (\Theta_D + \tau \cdot \Theta(T_{c0})) - \tau \cdot R \cdot \Omega \cdot \Theta(T_{c0}) \quad (243)$$

$$\Theta(T_B) = T_B + \delta(T_B) \approx T_B + \delta_\infty$$

$$\Theta(T_S) = T_S + \delta(T_S) \approx T_S + \delta_\infty \quad (244)$$

$$\Theta(T_{c0}) = T_{c0} + \delta(T_{c0})$$

Using the relation:

$$\int_0^S dz \alpha(z) \tau(z, S) = \int_0^S dz \alpha(z) e^{-\int_z^S dz' \alpha(z')} = \int_0^S dz \frac{\partial}{\partial z} e^{-\int_z^S dz' \alpha(z')} = \left[e^{-\int_z^S dz' \alpha(z')} \right]_0^S = 1 - \tau \quad (245)$$

we find:

$$\begin{aligned} \Theta_U &= \int_0^S dz \alpha(z) \Theta[T(z)] \tau(z, S) = \int_0^S dz \alpha(z) [T(z) + \delta(T(z))] \\ &\approx \int_0^S dz \alpha(z) T(z) + \delta_\infty \cdot \int_0^S dz \alpha(z) \tau(z, S) = T_{BU} + \delta_\infty \cdot (1 - \tau) \end{aligned} \quad (246)$$

$$\Theta_D = T_{BD} + \delta_\infty \cdot (1 - \tau)$$

Substituting (244) and (244) into (243) gives:

$$\begin{aligned} T_B &= [T_{BU} + \tau \cdot E \cdot T_S + \tau \cdot R \cdot (1 + \Omega) \cdot T_{BD}] + \\ &[-\delta_\infty + \delta_\infty \cdot (1 - \tau) + \tau \cdot (1 - R) \cdot \delta_\infty + \tau \cdot R \cdot \delta_\infty \cdot (1 - \tau)] + \\ &\tau \cdot R \cdot \Omega \delta_\infty \cdot (1 - \tau) + \tau^2 \cdot R \cdot (1 + \Omega) \cdot [T_{c0} + \delta(T_{c0})] - \tau \cdot R \cdot \Omega \cdot [T_{c0} + \delta(T_{c0})] \end{aligned}$$

$$\begin{aligned} T_B &= [T_{BU} + \tau \cdot E \cdot T_S + \tau \cdot R \cdot (1 + \Omega) \cdot T_{BD}] - \\ &\tau^2 \cdot R \cdot \delta_\infty + \tau \cdot R \cdot \Omega \delta_\infty \cdot (1 - \tau) + \tau^2 \cdot R \cdot (1 + \Omega) \cdot [T_{c0} + \delta(T_{c0})] - \\ &\tau \cdot R \cdot \Omega \cdot [T_{c0} + \delta(T_{c0})] \end{aligned}$$

$$\begin{aligned} T_B &= [T_{BU} + \tau \cdot E \cdot T_S + \tau \cdot R \cdot (1 + \Omega) \cdot T_{BD}] - \\ &\tau^2 \cdot R \cdot (1 + \Omega) \cdot \delta_\infty + \tau^2 \cdot R \cdot (1 + \Omega) \cdot [T_{c0} + \delta(T_{c0})] + \\ &\tau \cdot R \cdot \Omega \delta_\infty - \tau \cdot R \cdot \Omega \cdot [T_{c0} + \delta(T_{c0})] \end{aligned}$$

$$\begin{aligned} T_B &= [T_{BU} + \tau \cdot E \cdot T_S + \tau \cdot R \cdot (1 + \Omega) \cdot T_{BD}] + \\ &\tau^2 \cdot R \cdot (1 + \Omega) \cdot [T_{c0} + \delta(T_{c0}) - \delta_\infty] - \tau \cdot R \cdot \Omega \cdot [T_{c0} + \delta(T_{c0}) - \delta_\infty] \end{aligned} \quad (247)$$

$$T_B = [T_{BU} + \tau \cdot E \cdot T_S + \tau \cdot R \cdot (1 + \Omega) \cdot T_{BD}] + \tau^2 \cdot R \cdot (1 + \Omega) \cdot T_c - \tau \cdot R \cdot \Omega \cdot T_c$$

That means after a few manipulations we recover the form (103) with the effective cold space temperature (237).

To summarize: For all practical applications that involve cold space radiation at GMI frequencies we can use the RJ approximation to the Planck law as long as we use the effective cold space temperature from (237) with the values given in Table 26.

Bibliography

- [1] T. Mo, M. D. Goldberg, D. S. Crosby, and Z. Cheng, "Recalibration of the NOAA microwave sounding unit," *Journal of Geophysical Research*, vol. 106, no. D10, pp. 10145-10150, 2001.
- [2] J. Claassen and A. K. Fung, "The Recovery of Polarized Apparent Temperature Distributions of Flat Scenes from Antenna Temperature Measurements," *IEEE Transactions on Antennas and Propagation*, vol. 22, no. 3, pp. 433-442, May. 1974.
- [3] H. C. Ko, "On the Reception of Quasi-Monochromatic, Partially Polarized Radio Waves," *Proceedings of the IRE*, vol. 50, pp. 1950-1957, Sep. 1962.
- [4] J. R. Piepmeier, D. G. Long, and E. G. Njoku, "Stokes Antenna Temperatures," *IEEE Transactions on Geoscience and Remote Sensing*, vol. 46, no. 2, pp. 516-527, Feb. 2008.
- [5] G. Sinclair, "The Transmission and Reception of Elliptically Polarized Waves," *Proceedings of the IRE*, vol. 38, pp. 148-151, Feb. 1950.
- [6] A. C. Ludwig, "The definition of cross polarization," *IEEE Transactions on Antennas and Propagation*, vol. 21, pp. 197-200, Jan. 1973.
- [7] T. Meissner and F. J. Wentz, "Polarization rotation and the third Stokes parameter: The effects of spacecraft attitude and Faraday rotation," *IEEE Transactions on Geoscience and Remote Sensing*, vol. 44, no. 3, pp. 506-515, 2006.
- [8] G. B. Rybicki and A. Lightman, *Radiative Processes in Astrophysics*. New York: John Wiley & Sons, Inc., 1979, p. 382.
- [9] H. J. Liebe, P. W. Rosenkranz, and G. A. Hufford, "Atmospheric 60-GHz oxygen spectrum: New laboratory measurements and line parameters," *Journal of Quantitative Spectroscopy & Radiative Transfer*, vol. 48, pp. 629-643, 1992.
- [10] M. J. Schwartz, "Observation and Modeling of Atmospheric Oxygen Millimeter-wave Transmittance." Ph.D., M.I.T., 1997.
- [11] P. Rosenkranz, "Water vapor microwave continuum absorption: A comparison of measurements and models," *Radio Science*, vol. 33, no. 4, pp. 919-928, 1998.
- [12] V. H. Payne, E. J. Mlawer, K. E. Cady-Pereira, and J. L. Moncet, "Water vapor continuum absorption in the microwave," *IEEE Transactions on Geoscience and Remote Sensing*, vol. in print, 2011.
- [13] T. Meissner and F. J. Wentz, "The complex dielectric constant of pure and sea water from microwave satellite observations," *IEEE Transactions on Geoscience and Remote Sensing*, vol. 42, no. 9, pp. 1836-1849, 2004.
- [14] F. J. Wentz and T. Meissner, "AMSR Ocean Algorithm, Version 2," Remote Sensing Systems, Santa Rosa, CA, 121599A-1, 2000. [Online]. Available: http://www.remss.com/papers/amr/AMSR_Ocean_Algorithm_Version_2.pdf.

- [15] A. Stogryn, "The apparent temperature of the sea at microwave frequencies," *IEEE Transactions on Antennas and Propagation*, vol. AP-15, pp. 278-286, 1967.
- [16] Meissner, Thomas and Wentz, Frank J., "Ocean retrievals for WindSat: Radiative transfer model, algorithm, validation," presented at the 9th Specialist Meeting on Microwave Radiometry and Remote Sensing Applications, Puerto Rico, USA, 2006, Paper Catalog # 06EX1174C. [Online]. Available: [http://www.remss.com/papers/meissner_and_wentz\(2006\).pdf](http://www.remss.com/papers/meissner_and_wentz(2006).pdf).
- [17] T. Meissner and F. J. Wentz, "The Emissivity of the ocean surface between 6 - 90 GHz over a large range of wind speeds and Earth incidence angles," *IEEE Transactions on Geoscience and Remote Sensing*, vol. submitted, 2011.
- [18] S. Yueh, W. Wilson, S. J. Dinardo, and F. Li, "Polarimetric microwave brightness signatures of ocean wind directions," *IEEE Transactions on Geoscience and Remote Sensing*, vol. 37, no. 2, pp. 949-959, 1999.
- [19] T. Meissner and F. J. Wentz, "An updated analysis of the ocean surface wind direction signal in passive microwave brightness temperatures," *IEEE Transactions on Geoscience and Remote Sensing*, vol. 40, no. 6, pp. 1230-1240, 2002.
- [20] C. S. Cox and W. H. Munk, "Measurement of the roughness of the sea surface from photographs of the sun's glitter," *Journal of the Optical Society of America*, vol. 44, no. 11, pp. 838-850, 1954.
- [21] R. W. Reynolds and T. M. Smith, "Improved global sea surface temperature analyses using optimum interpolation," *Journal of Climate*, vol. 7, pp. 929-948, 1994.
- [22] J. Hollinger, R. Lo, G. Poe, R. Savage, and J. Pierce, "Special Sensor Microwave/Imager User's Guide. NRL Tech. Rpt," Naval Research Laboratory, Washington, DC, Technical Report 1987.
- [23] W. H. Press, S. A. Teukolsky, W. T. Vetterling, and B. P. Flannery, *Numerical Recipes in Fortran 77*, 2nd ed. Cambridge: Cambridge University Press, 1992.
- [24] O. Montenbruck and E. Gill, *Satellite Orbits: Models, Methods, and Applications*. Berlin: Springer, 2000.
- [25] E. Twarog, W. E. Purdy, P. W. Gaiser, K. H. Cheung, and B. E. Kelm, "WindSat On-Orbit Warm Load Calibration," *IEEE Transactions on Geoscience and Remote Sensing*, vol. 44, no. 3, pp. 516-529, Mar. 2006.
- [26] F. J. Wentz, "A well calibrated ocean algorithm for special sensor microwave / imager," *Journal of Geophysical Research*, vol. 102, no. C4, pp. 8703-8718, 1997.
- [27] T. Meissner and F. J. Wentz, "Polarization rotation and the third stokes parameter: The effects of spacecraft attitude and faraday rotation," *IEEE Transactions on Geoscience and Remote Sensing*, vol. 44, no. 3, pp. 506-515, 2006.

- [28] W. E. Purdy, P. W. Gaiser, G. A. Poe, E. A. Uliana, T. Meissner, and F. J. Wentz, "Geolocation and pointing accuracy analysis for the WindSat sensor," *IEEE Transactions on Geoscience and Remote Sensing*, vol. 44, no. 3, pp. 496-505, 2006.
- [29] K. A. Hilburn and F. J. Wentz, "Mitigating the impact of RADCAL beacon contamination on F15 SSM/I ocean retrievals.," *Geophysical Research Letters*, vol. 35, Sep. 2008.
- [30] G. A. Poe, "Optimum Interpolation of Imaging Microwave Radiometer Data," *IEEE Transactions on Geoscience and Remote Sensing*, vol. 28, no. 5, pp. 800-810, 1990.
- [31] A. Stogryn, "Estimates of Brightness Temperatures from Scanning Radiometer Data," *IEEE Transactions on Antennas and Propagation*, vol. AP-26, no. 5, pp. 720-726, 1978.
- [32] F. Reif, *Fundamentals of Statistical and Thermal Physics*. San Francisco: McGraw-Hill, inc., 1965.